LRP 524/95 August 1995

Invited and Contributed Papers
presented at the
22nd EPS CONFERENCE ON CONTROLLED FUSION AND PLASMA PHYSICS

Bornemouth, UK.
3 - 7 July, 1995

LIST OF CONTENTS

Ohmic H-mode and confinement in TCV

J.-M. Moret, M. Anton, S. Barry, R. Behn, G. Besson, F. Bühlmann, A. Burri, R. Chavan, M. Corboz, C. Deschenaux, M.J. Dutch, B.P. Duval, D. Fasel, A. Favre, S. Franke, A. Hirt, F. Hofmann, C. Hollenstein, P.-F. Isoz, B. Joye, J.B. Lister, X. Llobet, J.-C. Magnin, P. Mandrin, B. Marletaz, P. Marmillod, Y. Martin, J.-M. Mayor, J. Moravec*, C. Nieswand, P.J. Paris, A. Perez, Z.A. Pietrzyk, V. Piffl*, R.A. Pitts, A. Pochelon, O. Sauter, W. van Toledo, G. Tonetti, M.Q. Tran, F. Troyon, D.J. Ward, H. Weisen

Centre de Recherches en Physique des Plasmas
École Polytechnique Fédérale de Lausanne
Association Euratom - Confédération Suisse
CH-1015, Lausanne, Switzerland

* Institute of Plasma Physics
Czech Academy of Science
Za Slovankou 3, 18200 Praha 8, Czech Republic

Abstract: The unique flexibility of TCV for the creation of a wide variety of plasma shapes has been exploited to address some aspects of tokamak physics for which the shape may play an important role. The electron energy confinement time in limited ohmic L-mode plasmas whose elongation and triangularity have been varied ($\kappa = 1.3 - 1.9$, $\delta = 0.1 - 0.7$) has been observed to improve with elongation as $\kappa^{0.5}$ but to degrade with triangularity as $(1 - 0.8\ \delta)$, for fixed safety factor. Ohmic H-modes have been obtained in several diverted and limited configurations, with some of the diverted discharges featuring large ELMs whose effects on the global confinement have been quantified. These effects depend on the configuration: in double null (DN) equilibria, a single ELM expels on average 2%, 6% and 2.5% of the particle, impurity and thermal energy content respectively, whilst in single null (SN) configurations, the corresponding numbers are 3.5%, 7% and 9%, indicative of larger ELM effects. The presence or absence of large ELMs in DN discharges has been actively controlled in a single discharge by alternately forcing one or other of the two X-points to lie on the separatrix, permitting stationary density and impurity content ($Z_{eff} \approx 1.6$) in long H-modes (1.5 s).

1. Introduction

The principal goal of TCV (Tokamak à Configuration Variable) is to investigate effects of the plasma shape, in particular high elongation, on tokamak physics and performance. The shape variability of TCV can cover high elongations, $\kappa \leq 3$, and high positive or negative triangularity (with independent control of the top and bottom triangularity). A wide variety of open diverted configurations are possible, including single null (SN) or double null (DN) equilibria with a large variation in X-point position, divertor leg geometry and strike zone location and extension. In order that these different shapes may be created without any hardware modification, the TCV design incorporates a number of unusual features. The vacuum vessel has a nearly rectangular cross-section with a height-to-width ratio of 3 and is continuously welded. Its low toroidal resistance (55 $\mu\Omega$) allows passive stabilisation of vertical plasma movement at high elongation. Plasma shaping is accomplished by a set of 16 independently controlled poloidal coils, arranged in two vertical stacks of 8 on each side of the vessel. Other constructional parameters are major radius, $R = 0.89$ m, minor radius, $a \leq 0.25$ m, toroidal magnetic field, $B_T \leq 1.43$ T and maximum plasma current at full elongation, $I_p > 1$ MA.

From the beginning of physics operation in June 1993, a large effort has been devoted to the establishment and optimisation of the extremely versatile shape control system required to exploit the potential of TCV. The combination of the outer coil power supply bandwidth and the shielding effect of the vacuum vessel limits the maximum vertical instability growth rate, γ, and hence the maximum plasma elongation that can be stabilised. To date, the highest elongation achieved is $\kappa = 2.05$ at $I_p = 800$ kA and, in a separate discharge, a maximum value of $\gamma = 1000\ s^{-1}$ has been obtained. To permit stabilisation of the highest elongations and hence allow TCV to reach its full design specification, internal coils have been installed inside the vessel and a dedicated fast power supply is now being commissioned for operation later in 1995. Installation of a 4.5 MW ECRH system is also underway to permit further improvement in plasma performance.

This paper addresses a number of physics issues for which the study of the influence of plasma shape is important. First results will be presented in each case. The first subject, discussed in Section 2, treats the influence of shape on global energy confinement, for which the present database is rather sparse, comprising mainly extrapolations of results from different machines. As a second topic, the ohmic H-mode, which has been achieved in virtually all configurations in TCV will be presented in Sections 3 and 4. Section 3 gives a phenomenological description of the H-mode, whilst Section 4 describes the impact of ELMs on the global confinement in many configurations. The discussion of Section 5 will show how fine shape adjustments can control the ELM occurrence. The last, Section 6, explores the present TCV operational domain, describing results of measurements and modelling of the vertical instability growth rate in several configurations.

2. Influence of plasma shape on confinement

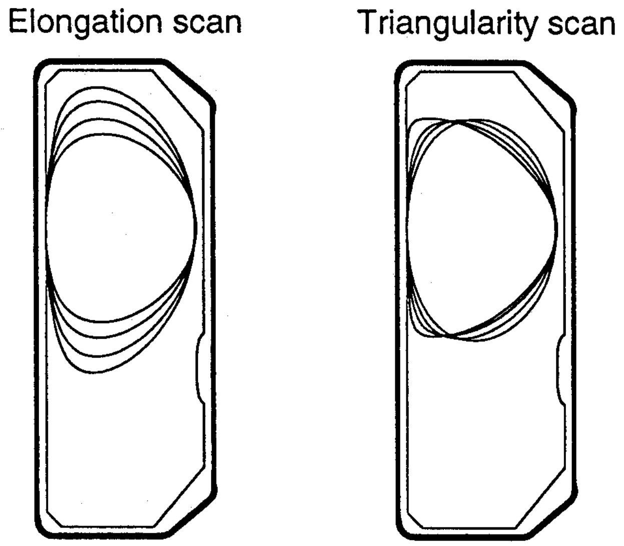

Fig. 1 The elongation and triangularity scan used for the confinement study.

Given the wide variety of possible TCV equilibria, a first step in the approach to quantifying the influence of plasma shape on confinement properties has been to concentrate on the study of a few specific shapes. Since elongation and triangularity are two of the most important shape parameters, both an elongation scan at fixed triangularity and a scan in triangularity, δ, at fixed elongation have been performed. Configurations with values of $\kappa = 1.3, 1.5, 1.7$ and 1.9 at a fixed $\delta = 0.3$ and $\delta = 0.1, 0.3, 0.5$ and 0.7 at a fixed $\kappa = 1.5$ have been generated. Analytic shape contour coordinates were used: $R = R_0 + a \cos(\theta + \delta \sin\theta)$ and $Z = Z_0 + a\,\kappa \sin\theta$ where (R_0,Z_0) refers to the plasma centre, a is the minor radius and θ the poloidal angle [1]. Figure 1 illustrates these 7 shapes. It is impossible to maintain constant plasma current with such large shape modifications, due both to important variations in the edge safety factor and because the smallest configurations cannot accommodate large currents and the largest cannot be produced at low currents. A current scan has thus been performed in each configuration in order to encompass a variation of the edge safety factor q_a from 3 to 5, except at the highest elongation, for which the low currents corresponding to values of $q_a > 4$ lead to a high degree of vertical instability which cannot at present be controlled in TCV. These current scans are necessary to separate any influence of the shape on the confinement from an intrinsic dependence on the plasma current. Each discharge was performed at the same line averaged density, 8×10^{19} m^{-3}, so that any density dependence of the confinement need not to be accounted for. For each configuration, the plasma remained in L-mode and was limited by the graphite inner wall protection tiles. All data points were taken during stationary conditions, so that time derivatives of magnetic and thermal energy can be ignored during the analysis.

Since a measurement of the total radiated power, P_{rad}, is not yet available, the confinement properties of these plasmas are quantified simply by the electron energy confinement time, $\tau_{Ee} = W_e/P_{oh}$, where P_{oh} is the ohmic input power. The total electron energy, W_e, is obtained by volume integration of Thomson scattering measurements at up to 10 spatial positions. The electron energy confinement time is plotted in figure 2 as a function of the inverse safety factor, $1/q_a$, for all configurations. In all cases a decrease of τ_{Ee} is observed when I_p is increased, compatible with a $q_a^{0.3}$ scaling and somewhat weaker than in the neo-Alcator law. As shown by the decreased value of the ratio of the central value of the density to its volume average, the density profile broadens at high I_p. Thus, although the line average density remains constant, some residual dependency on the central density may also explain part or all of this variation of τ_{Ee}.

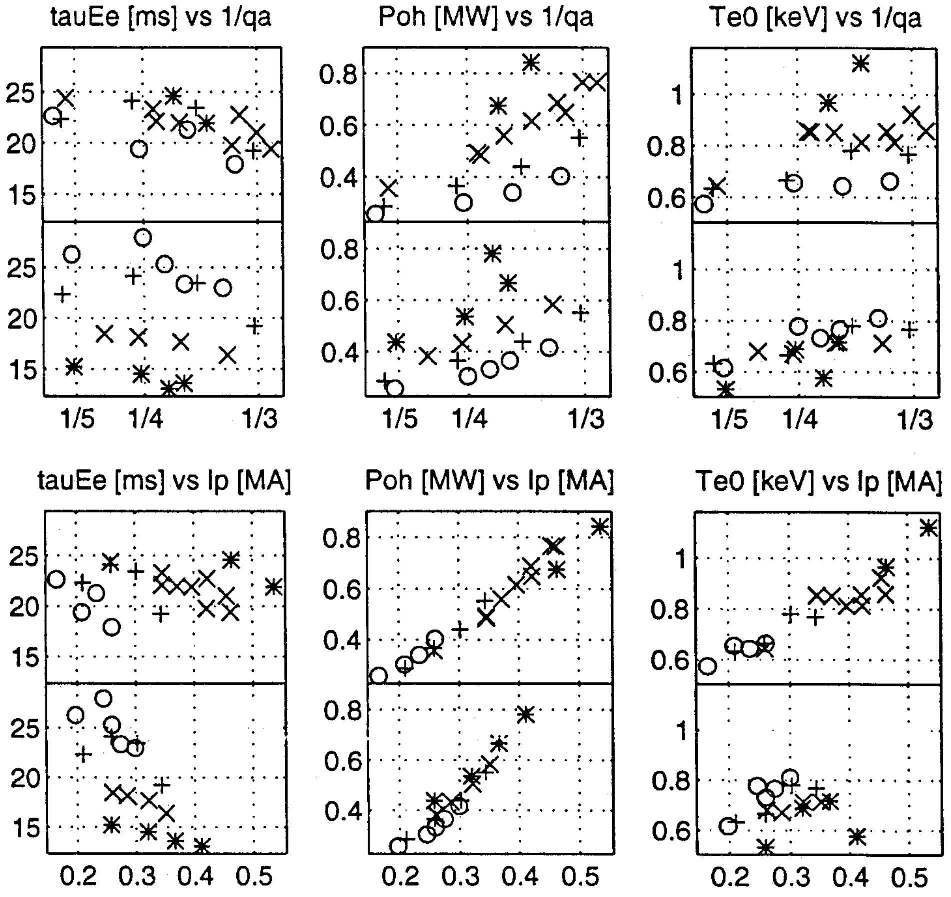

Fig. 2 Electron energy confinement time, ohmic power and central electron temperature plotted as a function of the inverse safety factor and of the plasma current. The following symbols are used:

		o	+	×	*
top half of each figure: elongation scan	κ =	1.3	1.5	1.7	1.9
bottom half of each figure: triangularity scan	δ =	0.1	0.3	0.5	0.7

Turning specifically to the elongation scan, the first observation shown in figure 2 is a large increase in the central electron temperature, $T_e(0)$, rising from 0.6 keV at the lowest current and elongation to 1.2 keV for the highest current and elongation. This leads to a relative increase in W_e larger than that of the plasma volume. In addition, the increase in the electric field necessary to drive the current (roughly proportional to $(\kappa^2 + 1) / 2$) is compensated by a decrease in the plasma resistivity, resulting in a loop voltage, V_{loop}, that, at a given value of q_a, is the same for all elongations. Combining these effects gives a τ_{Ee} which improves with elongation at a fixed value of q_a; this dependence may be described by a power law, $\kappa^{0.5 \pm 0.1}$. The ratio of the total energy confinement time predicted by the ITER89-P scaling law and the measured electron energy confinement time ranges from 0.6 to 1.2, which may indicate that the parametric dependence of ITER scaling is not incorrect. Extracting the varying parameters relevant to this elongation scan from the ITER89-P law yields a factor 2.5 $I_p^{0.85}\,\kappa^{0.5}\,P_{oh}^{-0.5}$, where the numerical coefficient (for I_p in MA and P_{oh} in MW) is specific to the TCV conditions and is chosen such that this factor is unity when extrapolating to $\kappa = 1$. The result is a predicted improvement of the confinement time that can be summarised by $\kappa^{1.2}$ and, as illustrated in figure 3, is substantially larger than that observed in TCV. The ITER89-P law essentially applies to confinement in presence of additional heating; in ohmic plasmas the intrinsic link between I_p and P_{oh} may render the comparison impossible. At high elongation, the increase in both P_{oh} and $T_e(0)$ results in an increased impurity concentration, observed on the soft X-ray emissivity [2] and on the intensity of a C-VI line measured by an ultra-soft X-ray spectrometer [3]. The concentration of carbon, the main impurity in TCV, deduced from these measurements is roughly proportional to the ohmic power leading to a ratio P_{rad}/P_{oh} that should be almost constant. Thus, a more refined estimate of τ_{Ee} accounting for the radiated power would give a correction factor that is essentially identical for all elongations and would not fundamentally modify the observed κ dependence.

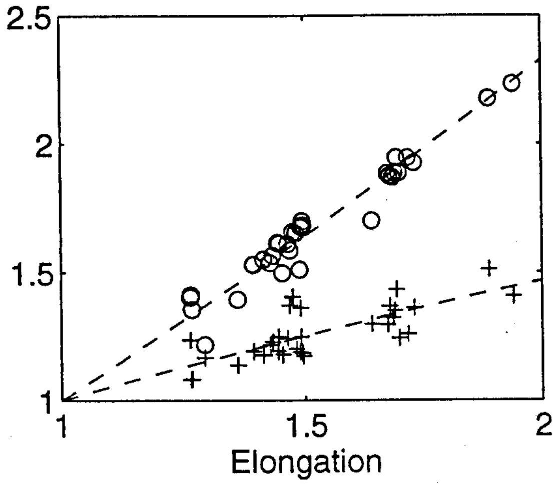

Fig. 3 Improvement factor of the electron energy confinement time when elongation is increased. Circles are the ITER89-P predictions, crosses the TCV measurements.

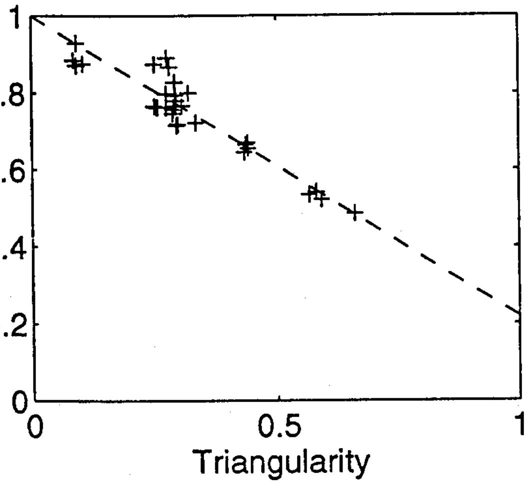

Fig. 4 Degradation factor of the electron energy confinement time when triangularity is increased.

In the triangularity scan, the current must be increased as δ varies in order to maintain constant q_a, with a corresponding increase in V_{loop}; modification of the resistance (via Z_{eff} or T_e) is, in contrast to the elongation scan, only marginal. The relative reduction of the electrical conductivity due to a larger fraction of trapped electrons at high triangularity is computed to be less than 5% for the highest triangularity and has also only a small influence on V_{loop}. The combination of these effects leads to a substantial reduction in τ_{Ee} of roughly 40% when passing from an elliptical shape to a triangularity of 0.7. This reduction cannot be explained by an intrinsic dependence on the plasma current alone; this clearly appears in a plot (figure 2) of τ_{Ee} versus I_p in which each triangularity forms a decreasing curve shifted with respect to the others. A small reduction in the impurity concentration is observed at fixed plasma current when increasing the triangularity. Thus the ratio P_{rad}/P_{oh} is decreasing and a confinement time corrected for the radiation loss would display an even larger degradation when the shape is more triangular. Whilst a power law cannot be used, figure 4 shows that for the δ variation explored in this study, a reduction factor of the form (1 - 0.8 δ) approximately describes the present data.

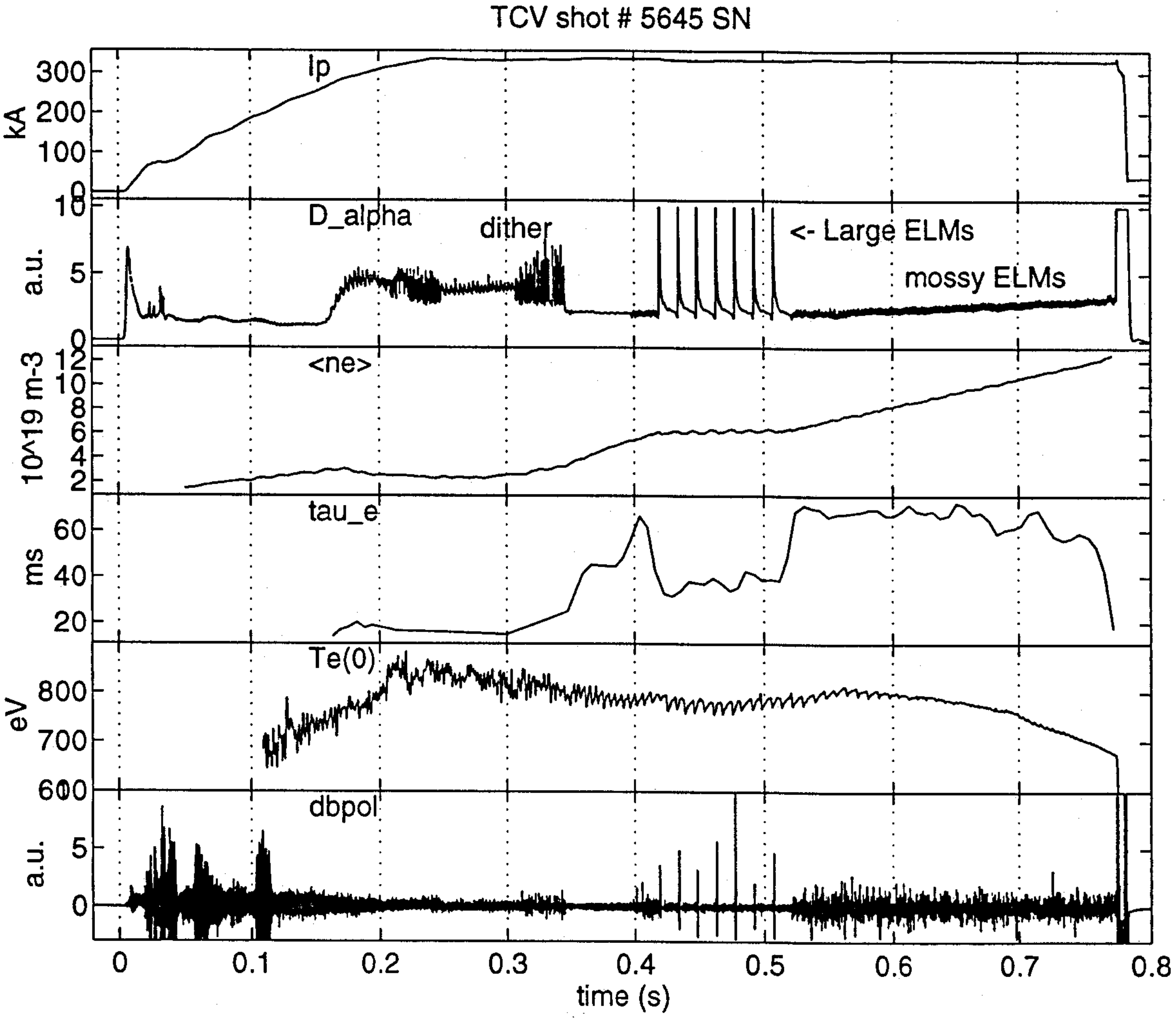

Fig. 5 Typical H-mode time traces. From top to bottom: plasma current, D_α signal, average electron density, energy confinement time, electron temperature from soft X-ray emission, MHD magnetic activity on the high field side midplane.

3. Ohmic H-mode phenomenology

Following the first boronisation in TCV, ohmic H-modes were obtained in discharges with a variety of shapes, including SN equilibria with the ion ∇B drift directed towards the X-point and DN configurations [4]. Limiter H-modes have also been achieved for κ between 1.7 and 1.9 at I_p ranging from 360 to 600 kA, although H transitions are only possible at 360 kA for values of $\delta \geq 0.25$. The discharge shown in figure 5 illustrates most of the features observed in TCV H-modes. Transitions can be "dithering", with the D_α intensity switching between L- and H-mode levels and can also feature ELMs with pulses of D_α emission well above the L-mode level. In general, an initial ELM-free period of 20 ms or more follows the L-H transition. In the example presented in figure 5, a short period of irregular "mossy" ELMs causing low amplitude fluctuations on the D_α signal precedes several large ELMs. The latter significantly reduce the energy confinement time and interrupt the density rise with, in this particular case, the H-phase terminating after a final period of mossy ELMs characterised by MHD activity and D_α modulation localised in the divertor region and do not appear to influence the global confinement. The fact that the first large ELM is observed only after an initial ELM-free period during which an edge pressure gradient can build up, suggests that these large ELMs may be related to type I ELMs observed in other devices with additional heating. There is no physics reason why this type of ELM should exist only in the presence of additional heating, provided that the edge confinement is effective enough to bring the pressure gradient there to the ELM instability limit.

Fig 6 SN and DN equilibria used for quantification of the ELM effects.

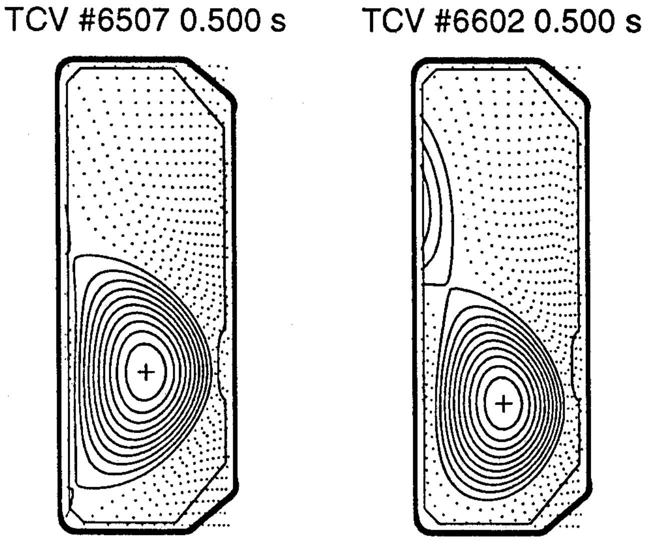
TCV #6507 0.500 s

TCV #6602 0.500 s

4. Effect of ELMs on the global confinement

The potential for using ELMs as a means of controlling the impurity and α-particle content of an H-mode based reactor plasma requires knowledge both of how to control their occurrence and of their effect on global confinement. One method by which the latter may be investigated is to take the time average of particle and energy balance over many ELMs [5]. This approach allows an estimation of the average effect of a single ELM without requiring detailed measurements of relevant parameters for each ELM. In the case of electron particle balance this reads:

$$\langle dN/dt\rangle/N = S/N - 1/\tau_{up} - f_{ELM} \langle \Delta N_{ELM}\rangle/N, \qquad (1)$$

where the LHS is the rate of change of the total electron content averaged over many ELMs, S is a particle source, τ_{up} stands for the underlying particle confinement time (that which would prevail in the absence of ELMs), f_{ELM} symbolises the ELM repetition rate or frequency and $<\Delta N_{ELM}>$ is the average number of particles expelled by a single ELM. Analogous expressions hold for the impurity content, N_Z, and the thermal energy W. Only the quantities $<dN/dt>/N$ and f_{ELM} can be directly measured, but the relative number of electrons expelled by each ELM, $<\Delta N_{ELM}>/N$, may be evaluated from the slope of $<dN/dt>/N$ as a function of f_{ELM}.

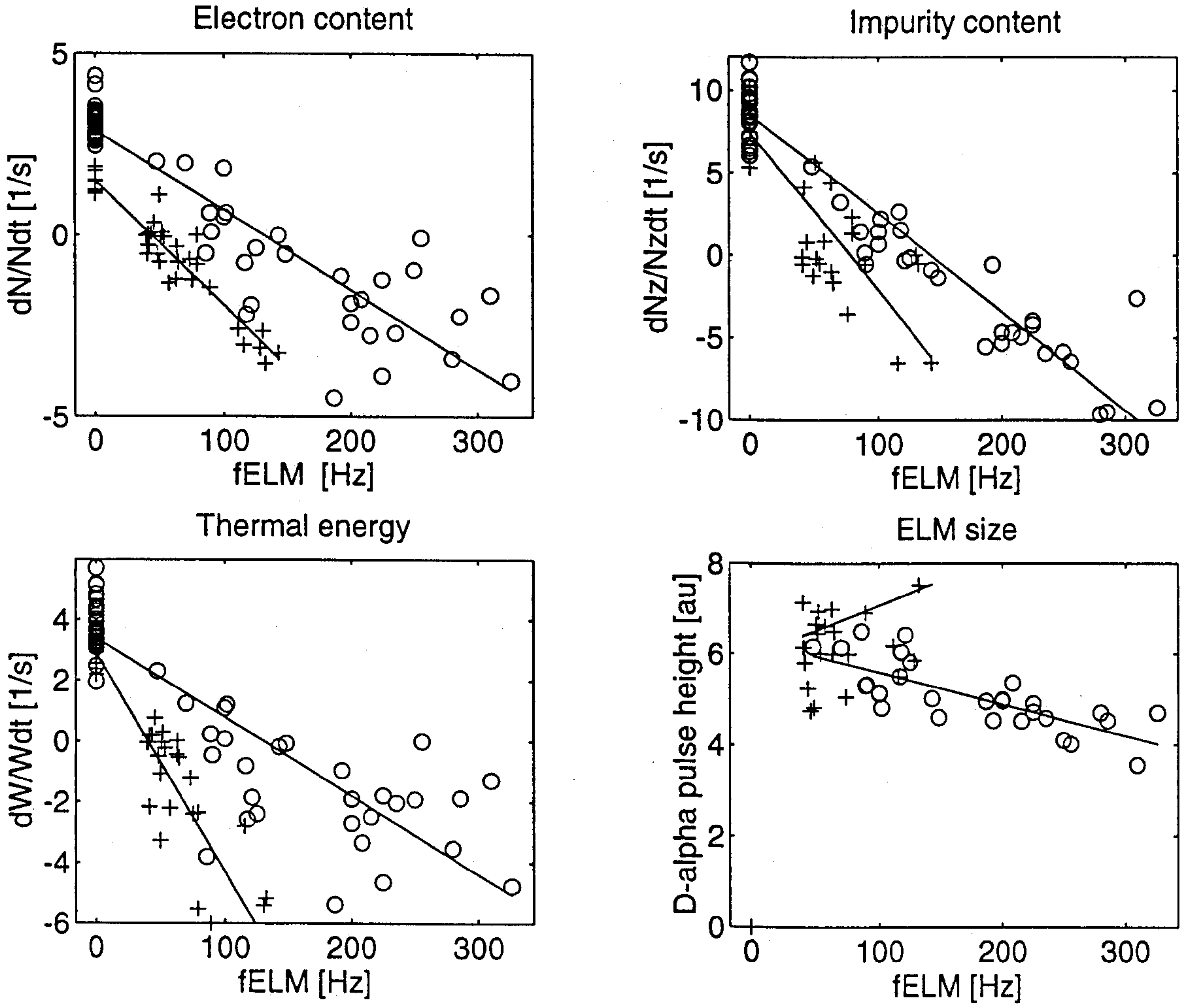

Fig. 7 Relative rate of change of the electron particle, the impurity and the thermal energy content as a function of the ELM frequency for the SN (+) and DN (o) configuration.

Two configurations have been studied in detail, a DN D-shaped configuration with $\kappa = 1.7$, $\delta = 0.7$ and $I_p = 390$ kA and a SN configuration with the ion drift directed toward the X-point and with $\kappa = 1.6$, $\delta = 0.3$ and $I_p = 330$ kA, both shown in figure 6. In these experiments the total electron content was measured by a 4-channel interferometer, the impurity content estimated from the soft X-ray emissivity [2] and the total thermal energy derived from the equilibrium reconstruction based only on magnetic measurements. Each experimental trace is divided into time windows of roughly constant ELM frequency in which the relevant quantities and their time derivatives are estimated. The corresponding rates of change are plotted in figures 7 as a function of f_{ELM} for both configurations, together with the D_α spike amplitude. The latter varies only slightly over the observable frequency range. The rates of change are nearly linear with f_{ELM} up to frequencies of about 300 Hz and 120 Hz for the DN and the SN configurations respectively. Above these frequencies small, irregular ELMs and H-L transitions render this type of analysis impracticable. The slopes of the fitted lines indicate that in DN each ELM expels on average 2% of the electron content, 2.5% of the thermal energy and 6% of the impurity content. In SN, the corresponding numbers are 3.5%, 7% and 9% and are indicative of larger ELM effects in this configuration. Note that this is an estimate of the net loss fraction of particles, since the gross outward flux due to the ELMs may be partly offset by an influx due to ELM-enhanced recycling. In addition, the estimate of the impurity content is based only on a single chord measurement and cannot account for a spatial distribution or a profile change due to the ELMs. The fraction of thermal energy released by the ELMs is observed to be larger than that of the particle content in both configurations. This shows that the expelled energy is larger than the initial thermal energy of the expelled particles and suggests a transient enhancement in transport larger for the heat than for the particles. In DN, stationary conditions are obtained for an ELM frequency of 120 Hz, where the fitted line crosses zero. At this point, the volume average electron density is $<n_e> \approx 8 \times 10^{19}$ m^{-3}, the effective charge $Z_{eff} \approx 1.6$ and the energy confinement time is reduced by ≈ 30% compared with the underlying value in the absence of ELMs. In SN, due to the larger effect of individual ELMs, stationary conditions are obtained at a lower ELM frequency of 50 Hz.

5. ELM control experiments

During H-mode DN experiments, the presence of large ELMs has been observed to be correlated with a slight poloidal flux imbalance between the two X-points. The ELMs appear only if the ion ∇B drift is directed away from the active X-point, defined as that lying on the separatrix. This phenomena has been used to actively control the ELM occurrence [6]. Switching between active upper and lower X-points (figure 8) is achieved simply by modulating the vertical position reference by a few millimetres. The most striking feature in figure 8 is the synchronisation of the ELM-free and ELMy phases with the imposed modulation, in this case ±12 mm. In this way, H-modes of long duration, up to 1.5 s, have been obtained in which a quasi-stationary density, $<n_e> \approx 8 \times 10^{19}$ m^{-3}, is achieved despite the ELM-free periods. Although higher than its L-mode level, the average impurity concentration also remains stationary at $Z_{eff} \approx 1.6$. This technique has also been used to feedback control the density during H–mode, by appropriately coupling the density error signal to the vertical position demand signal. Under these conditions, the plasma was again observed to toggle between the ELM-free and ELMy states. This is indicative of an hysteresis in the establishment of the conditions required for the ELMs to appear. This observation and the fact that large ELMs have never been seen during the first 20 ms of an H-mode, suggest that not only the configuration, but also other parameters and their time evolution, such as the build up of an edge pressure gradient, are important in determining the stability domain of occurrence of large ELMs.

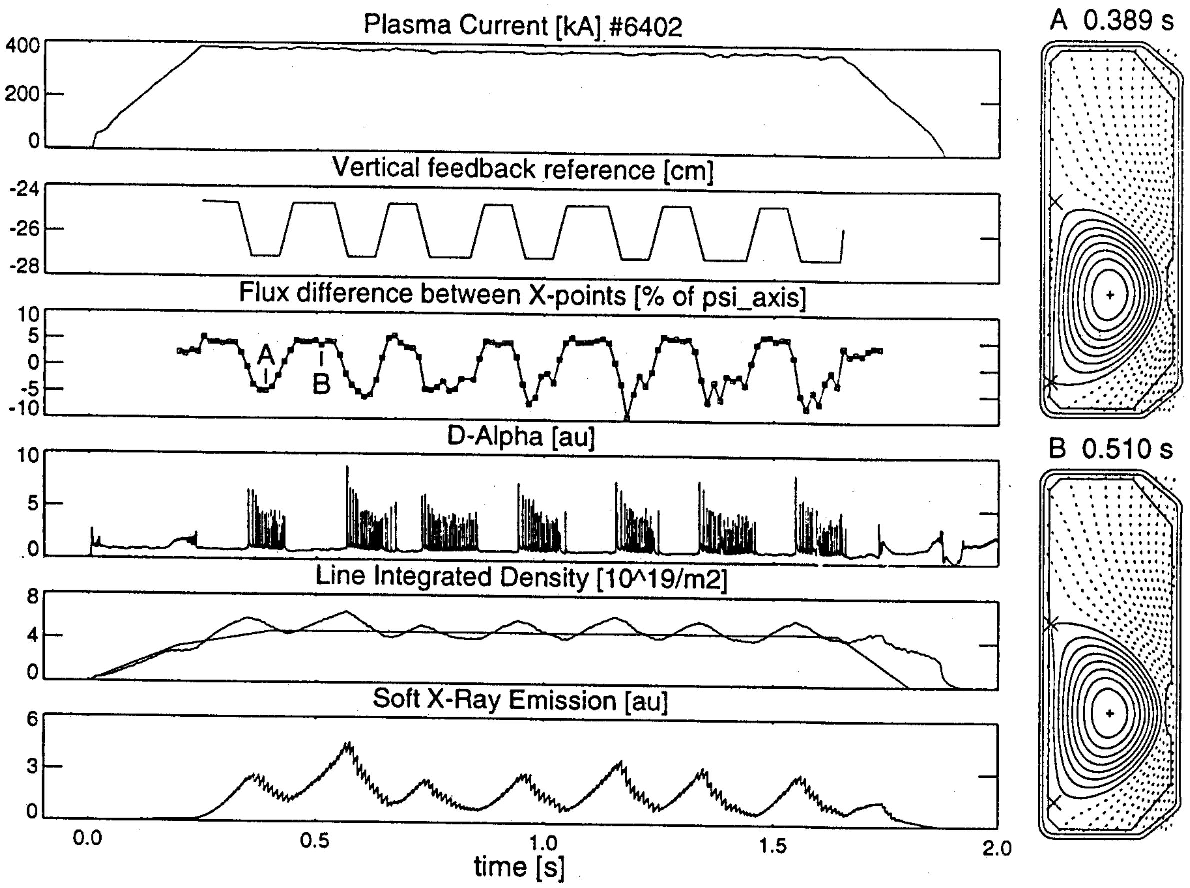

Fig. 8 Active ELM control.

6. Measurement and modelling of the vertical growth rate

The very elongated shapes possible in TCV offer an ideal opportunity to experimentally determine vertical instability growth rates for a variety of plasma shapes and to compare the results with modelled values [7]. A series of discharges has been performed in which both the vertical and radial position feedback loops acting on the outer shaping coils were opened following establishment of the final configuration. The plasma motion during the subsequent vertical displacement disruption was monitored both by the real time observer of the centre of gravity of the current distribution (as described in [1]) and by the equilibrium reconstruction. In each case, a vertical growth rate was extracted from the exponential temporal evolution. Three shape parameters were varied at a fixed plasma current of 250 kA: an elongation scan from $\kappa = 1.4$ to 1.75, a triangularity scan from $\delta = 0.1$ to 0.65 and a vertical position scan from the vessel mid-plane, $Z_0 = 0$ m, to 0.3 m. The measured growth rates are plotted in figure 9 and show that the vertical instability increases rapidly with elongation. The maximum observed value of $\gamma = 1000\ \mathrm{s}^{-1}$ is the highest yet measured on TCV. Combined with the time constants of the vessel eigenmode current decay (2.7 to 8.2 ms), this value of γ corresponds to a stability margin of only 1.26 but is close to the maximum frequency response of the thyristor power supplies. The results demonstrate the beneficial effect of imposing strong triangularity when increasing the elongation, due to a reduction of the field curvature at fixed κ when δ is increased. The scan in vertical position indicates the importance in TCV of the proximity of the wall in making the vertical motion less unstable, due to better coupling of the plasma current distribution to the top or bottom vacuum vessel plates. These experimental values have been compared both with the predictions of a rigid displacement model of the current distribution in the presence of the vessel [8] and with calculations of the NOWA-W code [9] which also includes plasma deformability. Both models give good agreement with the experimental observations.

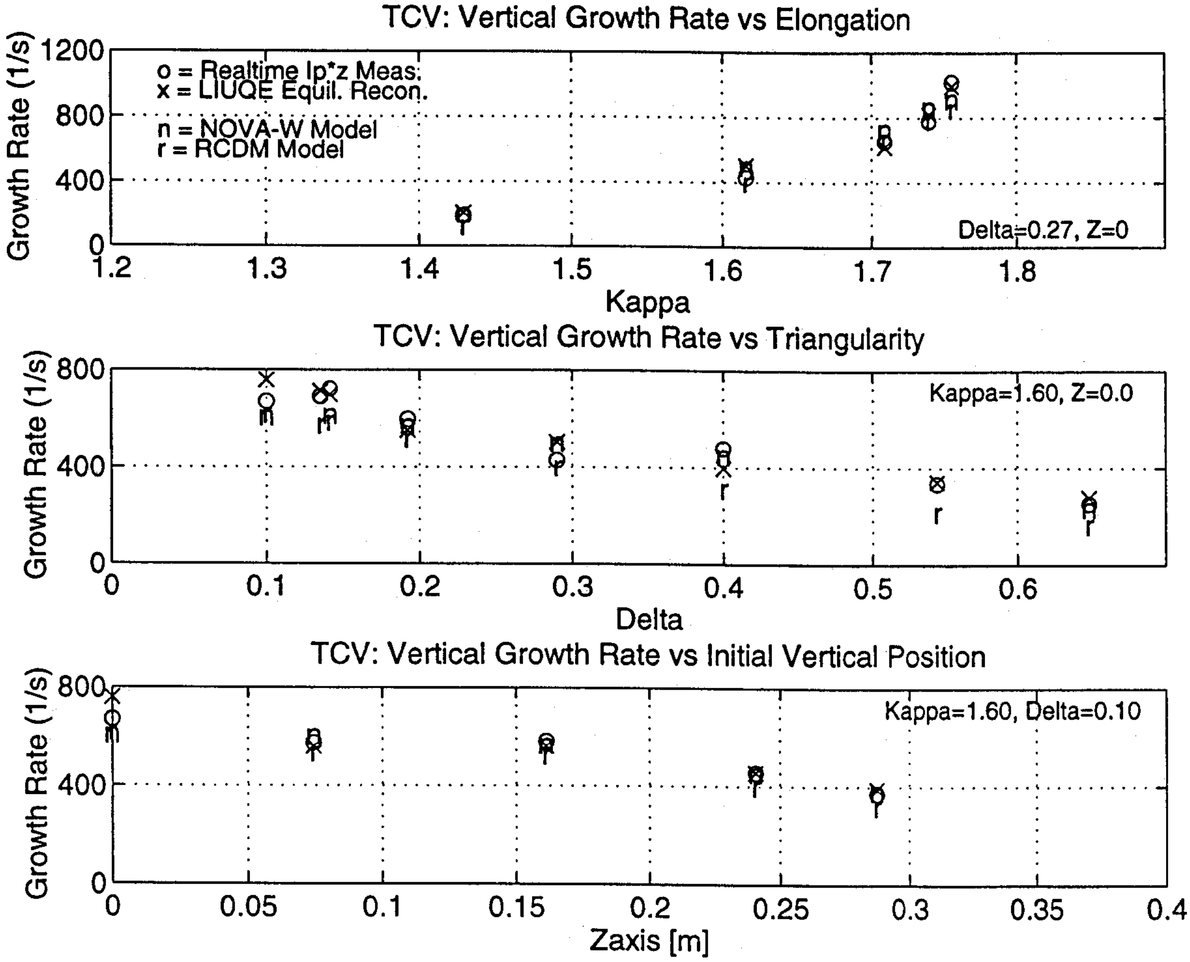

Fig. 9 Measurements and modelling of the vertical instability growth rate for an elongation, triangularity and vertical position scan.

7. Conclusions

After two years of operation, TCV has explored a large variety of plasma shapes, demonstrating the unique flexibility of the device and its control systems. Experiments have been performed that address specific aspects of tokamak physics for which the plasma shape plays an important role. The influence of elongation and triangularity on the confinement properties have begun to be explored in L-mode limited configurations. Preliminary results indicate that at a fixed value of the safety factor, the electron energy confinement time improves with the elongation as $\kappa^{0.5}$, but deteriorates at high triangularity by a factor (1 - 0.8 δ) for the equilibria studied. These important results need to be confirmed and the database enlarged to encompass a wider experimental parameter range, including additional heating. Together with improved diagnostic capability, this will hopefully permit a deeper insight into the underlying mechanisms governing these observations.

Ohmic H-modes in TCV are possible in all diverted configurations in which the ion ∇B drift is directed toward the active X-point and even in limited discharges. Large ELMs, probably related to type I ELMs seen in other machines with additional heating have been obtained. Their occurrence and the magnitude of their effect on the global confinement can be modified by varying the plasma configuration, especially near the X–points: SN equilibria display larger ELMs than DN equilibria and a slight imbalance of the X-points of DN in favour of the ion ∇B drift allows ELM suppression. This opens up the possibility of controlling the evolution of H-mode plasma parameters by appropriate tuning of discharge confinement properties through shape modifications.

Acknowledgements. It is a pleasure to acknowledge the entire TCV technical team for their continuous effort during the construction and the operation of the machine. This work was partially supported by the Fonds National Suisse de la Recherche Scientifique.

References

[1] Hofmann F, Dutch M J, Moret J-M, 1995, *Plasma shape control in TCV using MGAMS,* this conference.

[2] Weisen H, Pasini D, Weller A et al., 1991, *Rev. Sci. Instrum.* **62** 1531.

[3] Weisen H, Piffl V, Krejci A, Moravec J, Raus J, Dutch M J, Paris P J, 1995, *Ultra-soft X-ray spectroscopy using multilayer mirrors on TCV,*this conference.

[4] Hofmann F, Lister J B, Anton M, Barry S, Behn R, Bernel S, Besson G et al, 1994, *Plasma Phys. Control. Fusion* **36** B277.

[5] Weisen H, Dutch M J, Pochelon A, Hirt A, Pitts R A, Hofmann F, Anton M et al., 1995, *Edge localised modes in the TCV Tokamak,* this conference.

[6] Dutch MJ, Hofmann F, Duval BP, Hirt A, Joye B, Lister JB, Martin Yet al., 1995, *Nucl. Fusion* **35** 650.

[7] Dutch M J, Hofmann F, Sauter O, Ward D J, Anton M, Moret J-M, 1995, *Comparison of experimental and theoretical growth rates of the vertical instability in TCV,* this conference.

[8] Lister J B, 1995, *A rigid displacement model for vertical motion in TCV,* Lausanne report LRP 526/95.

[9] Ward D J, Jardin S C, Cheng C Z, 1993, *J. Comput. Phys.***104** 221.

MHD Operational Limits and Disruption Statistics in TCV Ohmic Plasmas

A. Pochelon, J.B. Lister, Ch. Deschenaux, X. Llobet, Y. Martin,
M. Anton, M.J. Dutch, B.P. Duval, F. Hofmann, B. Joye, Ch. Nieswand,
J.M. Moret, R.A. Pitts, G. Tonetti and H. Weisen.

Centre de Recherches en Physique des Plasmas
Association Euratom - Confédération Suisse
Ecole Polytechnique Fédérale de Lausanne
CH - 1015 Lausanne

Introduction:

We describe the operational limits of ohmic plasmas in the elongated TCV tokamak ($\kappa<3$, $I_p=1MA$, $R=0.88m$, $a=0.25m$, $B\varphi<1.5T$). The latter is a flexible machine in which a wide variety of plasma configurations may be produced and in which plasmas with $\kappa<2.1$, $-0.7<\delta<0.9$, $I_p < 0.81MA$ have already been achieved. The vessel interior has 64% coverage of carbon protection tiles and is regularly boronised. The data include plasmas produced both before and after boronisation in limiter and diverted configurations and in both L- and H-mode confinement regimes. A database dedicated to the study of the plasma operational range and disruption probability statistics has been created, covering one and half years of operation. The experimental campaigns in TCV are exploratory by design, leading inevitably to a large variety of disruptions. This paper presents a first attempt to describe disruptions and the operational range in TCV. The essential diagnostics presently available and used for this study are: the equilibrium reconstruction code LIUQE [1] based on magnetic measurements, a 5 channel interferometer, mhd probes, soft-X rays, and some spectroscopic lines. The quality of plasma performance so far achieved in these ohmic discharges is $\beta_N<2.0$, $H_{ITER\text{-}89P}<2.4$.

Disruption Description and Categorisation:

Initial attempts to classify the *"causes"* of disruptions in the five usual categories - density limit, q-limit, locked modes, vertical disruption events, impurity injection - have shown that this is a gross oversimplification. We have found it necessary to add additional *"environmental"*, non-numerical information such as: stationary plasma, change in the configuration, H- or L-mode, presence of ELMs, H to L-transition just before disruption, vertically unstable position or shape control experiment (type of experiment), or deliberate VDE, locked mode (or mode frequency decreasing to zero), technical problems, beginning or end of pulse, etc... In addition, it is necessary to provide information on the disruption *"evolution"*: for example, motion towards/away from the X-point and rapidity of the current quench.

These environmental variables appear particularly necessary since disruptions do not always originate from a single cause, but often reflect the simultaneous occurrence of (coupled) events. They may also reflect the difficulty of characterising certain disruptions.

Fig. 1 illustrates an example of an upper SN ELMy H-mode leading to disruption. At first glance, the ELMs may appear to be the cause. In fact, the ELMs seem to be triggered by repetitive upward motion resulting from non-optimal vertical position control, pressing the X-point onto the central column. Experiments in TCV have shown that these slight equilibrium modifications can influence ELM activity [2]. In this example ELMs, the vertical motion and ultimately also the sawteeth are coupled. Whilst some discharges continue with an H-L transition, revealed by the instantaneous increase of D_α and n=1 MHD activity, this example demonstrates a disruption which, in addition to q_{95} close to 2, is preceded by the simultaneous presence of non-optimal vertical control, ELMs and sawteeth.

Disruption Statistics:

A period of 1701 machine cycles has been selected for statistical study. Of this number, 1195 were full plasma attempts of which 342 failed to achieve the minimal condition of $I_p^{max}=50kA$, or $\overline{n}_e^{max}=3\times10^{18}m^{-3}$ and are therefore not retained. Data with $\kappa<1.2$ are included, but the reconstruction of internal parameters such as l_i is not attempted. This leaves 853 successful, elongated shots retained, of which 456 disrupted (53%). Among these disruptions, 130 were deliberately produced in vertical control experiments, leaving 38% "unforeseen" disruptions. For each shot, the variables of interest are stored in the database at regular intervals (50ms) together with 3 time slices just before the disruption event at 5ms intervals. In order to be able to compute a "disruptivity" (disruption rate normalised to the population density in a given range of the operational space), both disrupted and non-disrupted shots are included, especially since this study includes all TCV experimental campaigns, without dedicated shots to explore different disruption ranges.

Various Operational Diagrams:

The highest **densities** have been obtained at the highest currents possible with the higher elongations, generally in H-mode, with line-average densities reaching 2.2×10^{20} m^{-3} and corresponding to the Greenwald limit $\overline{n}_{e20}=0.27\times I_p[MA]/a^2[m^2]$ m^{-3} at constant current [3], **Fig. 2**. This limit can be largely exceeded (×1.6) in the current decrease phase. At constant current, the density limit corresponds to a Murakami value of $M_{19} = \overline{n}_e\times R/B\varphi = 13\times10^{19}Wb^{-1}$ following the first boronisation, compared with $5.5\times10^{19}Wb^{-1}$ before. The first boronisation more than doubled the maximum density and permitted access to the ohmic H-mode, in which the density limit rose from $M_{19}\,q_{95} = 15$ to 32 (constant current).

The low density range limit - due to **locked modes** - is subject to important variations, depending on wall conditioning, in particular on the ageing of the boronised layer. Fresh boronisation helps to improve operation below $\overline{n}_e=4\times10^{19}m^{-3}$. Locked-mode disruptions may be separated into two groups. A low density group peaking at $M_{19}=2$ found at any q<5, with a distinct grouping at q=3 and a high density group between q=2 and 3, **Fig. 3a**. Studying the effect of shaping on the presence of low density locked modes shows a very clear beneficial effect, with low density locked modes being strongly reduced for typically $\delta>0.3$ and $\kappa>1.6$, **Fig 3b**: shaping reduces the low density locked modes region to a small zone around $q=3$.

These two populations of high and low density **locked-mode** disruptions may also be clearly distinguished in the l_i-q diagram. The low density cases, essentially associated with ramp-up and establishment of the magnetic configuration, are typically spread over the l_i-q space below $q=5$ with again an accumulation at $q=3$. The high density locked modes concentrate in the region $2<q<3$ at low $l_i(1)<0.8$, our normal ohmic H-mode operating range.

In l_i-κ space, the different disruption "environments" can appear in very different locations, see **Fig. 4**. Whilst control experiments and plasma configuration changes tend to produce disruptions in the upper half of the operational l_i values, H-modes disrupt in the lower third portion of the operational l_i values, with ELM-free disruptions located at the very lower boundary limit. The low H-mode l_i values suggest an advantage of using H-mode confinement for high elongation experiments, making use of the associated naturally broader current profiles.

The normalised **beta**, $\beta_N = \beta(\%)\ (a\ B/I_p)$, computed from equilibrium code reconstructions in stationary ohmic conditions, is typically <2 in stationary ohmic conditions. The highest β_N values so far obtained have been produced at high density and with $\delta>0.45$, where ohmic H-mode is attained, suggesting a globally positive effect of triangularity on performance limits. In transient conditions, higher values are obtained: values of $\beta=3\%$ can be obtained by ramping down the toroidal field at constant plasma current in an ELM-free H mode discharge, yielding $\beta_N\leq2.2$. Such high values of β_N can also be obtained in the current ramp-down.

This first attempt to construct an operational and disruption statistics database for TCV has therefore shown the merit of plasma shaping for the achievement of high densities and high β_N in ohmic plasmas. Shaping also appears to have a very beneficial effect in strongly reducing the occurrence of low density locked-mode disruptions. This is of interest both for the improvement of the TCV operating range and for the set up of an adequate ECCD target plasma. This work was partly supported by the Fonds National Suisse de la Recherche Scientifique.

References:

[1] F. Hofmann, G. Tonetti, Nucl. Fus. **28**, 1871 (1988).
[2] M. Dutch, F. Hofmann, B.P. Duval et al., Nucl. Fus. (1995), to appear.
[3] M. Greenwald, J.L. Terry, S.M. Wolfe, S. Ejima et al., Nucl. Fus. **28**, 2199 (1988)

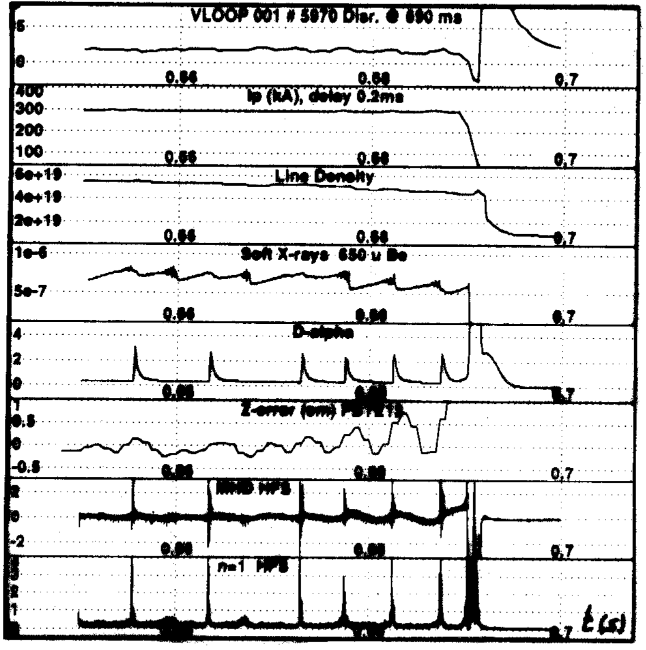

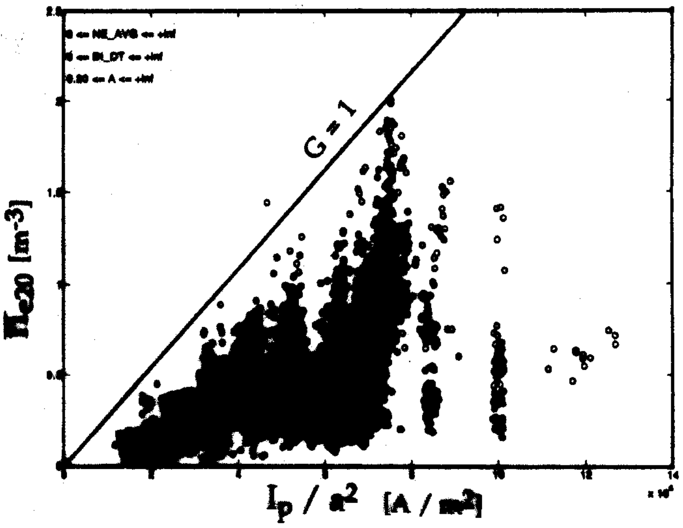

Fig. 2 Greenwald diagram.

Fig. 1 Example of multi-faceted disruption.

Fig. 3a

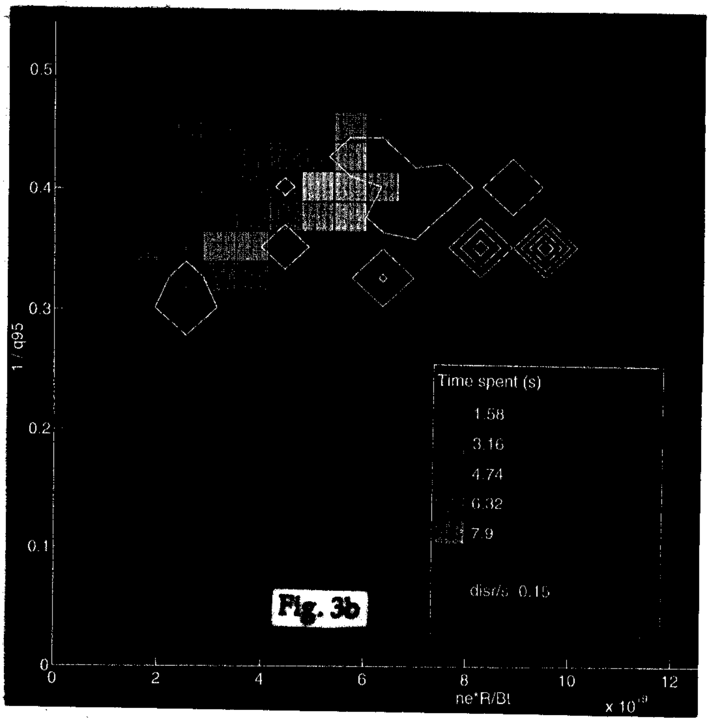

Fig. 3b

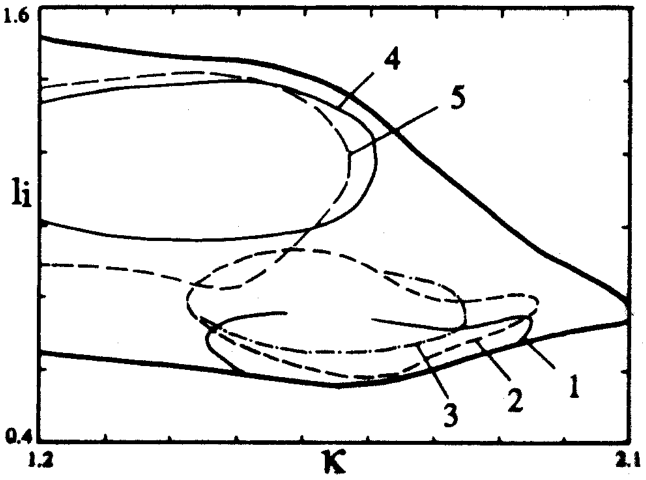

Fig. 3a Hugill diagram with the locked-modes contour line of 0.15 disr./s. The underlying gray tones express the time spent in the corresponding portion of operational space. Fig. 3b idem, but only for $\kappa > 1.6$, $\delta > 0.3$.

Fig. 4 l_i-κ diagram with the location of different disruption "environments":

1) H-mode, ELM-free, 2) H-L transition shortly before disr., 3) ELMy, 4) magnetic configuration change, 5) control experiments.

Plasma Shape Control in TCV using MGAMS

F. Hofmann, M.J. Dutch, J.-M. Moret
Centre de Recherches en Physique des Plasmas, EPFL
Association EURATOM - Confédération Suisse,
21 Avenue des Bains, CH-1007 Lausanne, Switzerland

1. Introduction

TCV is a rather unusual tokamak since it allows the creation of an extreme variety of plasma shapes and magnetic configurations. The MGAMS shape and position control algorithm [1] has been developed specifically for TCV with the aims of versatility, accuracy and ease of operation. The basic idea is that the operator only specifies the plasma shape and plasma current evolution and everything else is done automatically by the MGAMS software. This concept has proven very efficient in TCV since it allows us to create completely new plasma shapes in a single discharge, without using any information from previous discharges.

Plasma shape control in tokamaks involves basically four steps: (a) Identification of the plasma shape in real time, (b) Comparison of the real plasma shape with a preprogrammed shape, (c) Evaluation of coil current corrections such as to bring the real shape as close as possible to the preprogrammed shape, (d) Evaluation of coil voltages to produce the desired coil current corrections. In the following sections, we will show how each of these four steps is implemented in the MGAMS algorithm.

2. Shape Identification

In MGAMS, the plasma current distribution is reconstructed, in real time, in the form of a finite element matrix [2]. The current elements are fixed in space, and their amplitudes are determined such as to produce the best fit to the magnetic measurements (magnetic field probes, flux loops, coil currents and vessel currents). It should be noted that in TCV, it is essential to include the effects of vessel currents in the shape identification procedure, since the vacuum vessel has very low toroidal resistance (55 μΩ). Once the plasma current distribution is known, shape parameters can be derived in various ways. The standard method in MGAMS consists of defining a number of moments of the plasma current distribution,

$\Sigma I_i (Z_i - Z_o)$	vertical position
$\Sigma I_i (R_i - R_o)$	radial position
$\Sigma I_i (Z_i - Z_o)^2$	elongation
$\Sigma I_i (Z_i - Z_o) (R_i - R_o)$	tilt
$\Sigma I_i (Z_i - Z_o)^2 (R_o - R_i)$	triangularity

where I_i is the total current in the i-th element, (R_i, Z_i) are the coordinates of the current centroid of the i-th element and (R_o, Z_o) are the coordinates of an arbitrary reference position, usually taken as the expected initial position of the magnetic axis.

Alternatively, the plasma shape can be defined in terms of flux errors at the plasma boundary [1] or, equivalently, in terms of gaps between plasma surface and vessel wall.

3. Reference Shape

The time evolution of the reference plasma shape must be specified by the operator, either in analytic form, $R(t) = R_o + a \cos(\theta + \delta \sin\theta + \lambda \sin 2\theta)$ and $Z(t) = Z_o + a\,\kappa \sin\theta$, where θ is the poloidal angle and the parameters R_o, Z_o, a, κ, δ, λ are functions of time, or in the form of discrete boundary points, $R_i(t)$, $Z_i(t)$. The number of boundary points specified at each time slice is typically between 4 and 20. In addition, coordinates of X-points and separatrix strike points can be prescribed as functions of time. Using this information, MGAMS starts the shot preparation by computing a number of free-boundary equilibria [3]. This gives us a first estimate of the coil currents as functions of time. From these equilibria we also compute the various moments of the plasma current distribution, as defined in section 2. They serve as reference waveforms for those shape parameters which are feedback controlled. The final step in the shot preparation is the calculation of feed-forward coil voltages. This is achieved by solving the circuit equations for the complete tokamak discharge, including plasma and vessel currents.

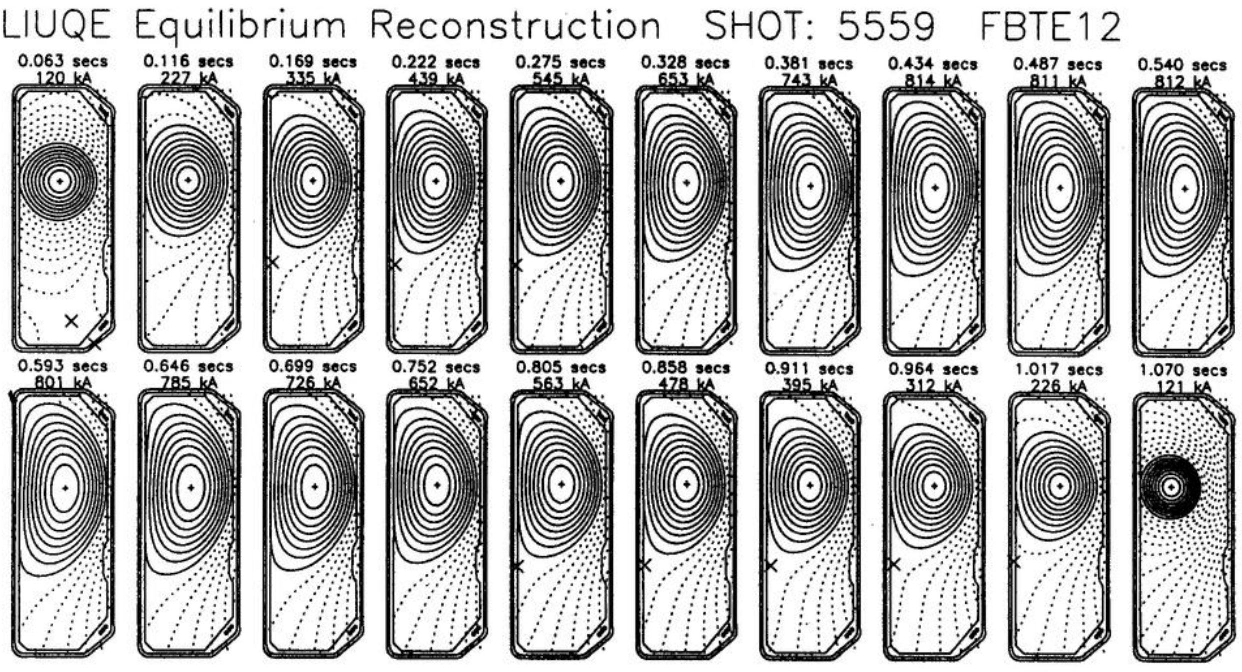

Fig. 1. Typical plasma evolution in TCV discharge ($I_{p,\,max} = 810$ kA, $\kappa_{max} = 2.0$)

4. Coil Current Corrections and Coil Voltages

Coil current corrections are computed in real time by the TCV hybrid matrix multiplier [4]. In MGAMS, these corrections are usually applied in the form of moments (vertical field, radial field, quadrupole field, hexapole field, etc.). Each moment is defined by a particular coil current distribution and, ideally, controls only one shape parameter. The moments are constructed as an orthogonal set. The amplitude of each moment, in real time, depends on the deviation of the measured shape parameter from its preprogrammed value. If the plasma shape is expressed in terms of flux errrors at the plasma boundary, the coil current corrections are evaluated in such a way as to minimize the flux errors [1]. The computation of instantaneous coil voltages which are required to produce the desired coil current corrections is basically straightforward, but it is complicated by the perturbing effect of the vessel currents.

5. User Interface

A graphical user interface has been developed for MGAMS, based on MATLAB software. The operator first specifies all input parameters: The plasma current must be given as a function of time (rampup phase, flattop and rampdown phase). The shape evolution must be specified, as explained in section 3, above. The rampdown phase is usually assumed to be the exact inverse of the rampup phase. However, in many cases, it is advantageous to program the rampdown phase slightly differently in order to avoid disruptions during rampdown. Finally the proportional, differential and integral gains have to be specified for the various feedback loops (plasma current, vertical position, radial position, plasma density, shape parameters, etc.). Once the operator has set the various parameters described above, the MGAMS shot preparation is launched. Coil currents and voltages are computed as functions of time, and the control matrices and reference waveforms are generated. Matrices and waveforms are then loaded into the TCV hybrid computer and the machine is ready for triggering a discharge.

6. Results

The MGAMS algorithm has allowed the creation of many different plasma shapes in TCV. A typical plasma evolution is shown in Fig.1. The equilibrium reconstructions shown here were performed after the discharge, using the LIUQE code [5]. The plasma current is ramped up to 810kA in 0.43 sec and the maximum elongation is 2.0. The accuracy of the shape control algorithm can be verified by comparing the preprogrammed shape with the shape obtained from full equilibrium reconstructions. It can also be tested by making use of other diagnostics, such as soft X-ray and visible imaging cameras. It is found that, for vertically elongated plasmas, the radial accuracy is generally better than 5 mm and the vertical accuracy is of the order of 1 cm. Fig.2. shows a number of plasma shapes that were produced in TCV, using MGAMS. Each image is taken from a different shot, and in each case, the shape is shown at the time when the plasma current has reached its maximum value. Some of the shapes shown here were generated for testing the algorithm, but in most cases, the particular shape was a necessary condition for reaching a certain physics goal.

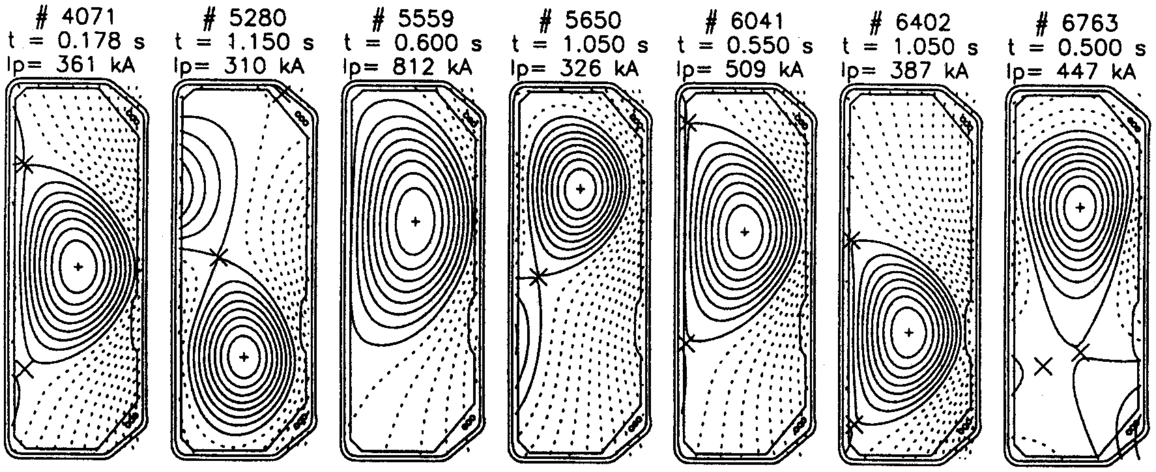

Fig.2. Selection of equilibrium reconstructions of plasmas produced in TCV using the MGAMS algorithm

7. Conclusion

MGAMS has proven to be an extremely versatile tool. It can generate any arbitrary plasma shape, subject to obvious physical constraints, without reference to a data base of precalculated equilibria or previous discharges. The shape accuracy depends on the precision of the magnetic measurements and is typically between 5 mm and 1 cm. Thanks to a graphical user interface, the algorithm is very easy to use. The original goal, i.e., that the operator only specifies the evolution of plasma current and shape and the algorithm does the rest, has been fully attained.

Acknowledgements: It is a pleasure to acknowledge the support of the entire TCV team. This work was partly supported by the Swiss National Science Foundation.

References:

[1] F. Hofmann, S.C. Jardin, Nuclear Fusion 30 (1990) 2013.

[2] F. Hofmann, G. Tonetti, Nuclear Fusion 28 (1988) 519.

[3] F. Hofmann, Computer Physics Communications 48 (1988) 207.

[4] P.F. Isoz, J.B. Lister, Ph. Marmillod, Proc. 16th Symp. on Fusion Technology, 1264 Oxford, 1990 (1991).

[5] F. Hofmann, G. Tonetti, Nuclear Fusion 28 (1988) 1871.

H-mode Threshold for Ohmic Plasmas in TCV

B.P. Duval, Y. Martin, M.J. Dutch, F. Hofmann, J.B. Lister, J.-M. Moret, Ch. Nieswand, R.A. Pitts, Z.A. Pietrzyk, A. Pochelon, G. Tonetti, H. Weisen

Centre de Recherches en Physique des Plasmas
École Polytechnique Fédérale de Lausanne
Association EURATOM - Confédération Suisse
21 Avenue des Bains, CH-1007 Lausanne, Switzerland

1. Introduction

Following the first boronisation of the TCV vacuum vessel, a clear H-mode transition has been observed with Single-Null (SN), Double-Null (DN) and highly elongated Limited magnetic configurations using ohmic heating only [1,2]. Figure 1 shows the reconstructed magnetic equilibria at the time of the L-H transition for a variety of plasma shapes for which a transition has been observed. For SN equilibria (Fig. 1a -b), H-mode is obtained only when the ion ∇B drift is directed towards the X-point. In DN configurations, H-mode transitions are equally observed independently of which of the X-points (upper Fig. 1d or lower Fig. 1e), lies on the separatrix. For most of these discharges, a clear density threshold is observed, in that, once the full magnetic configuration is established, as the density rises, H-mode is achieved at a density value that is often well reproduced by subsequent similar discharges.

Following a brief description of the general character of the H-mode transition in TCV, this paper reports on the behaviour of the density threshold for this transition. Whilst there is some early evidence for a dependence of the transition threshold on magnetic configuration, notably the plasma triangularity, there are strong indications that the threshold density is dominated by local recycling conditions.

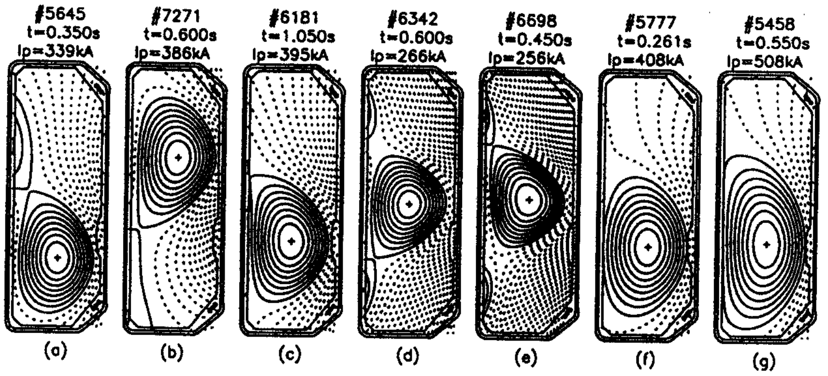

Figure 1. A selection of plasma equilibria at the time of the L-H transtion

2. H-mode Characteristics

The essential features of the ohmic H-mode transition in TCV are illustrated in Figure 2, where the time variation of the $D\alpha$ emission integrated along a vertical chord through the plasma is shown for four different discharges, reasonably typical of the observed behaviour. In general, the transition is marked by a sharp reduction (20 - 70% in less than 0.5ms) in the Dα intensity. It may be preceeded by a relatively calm phase marked by small fluctuations in the Dα intensity (Fig 2a), or by large amplitude oscillations ("dithering" phases) together with smaller fluctuations due to the effect of sawtooth activity on the edge plasma (Fig 2b-d). Indeed, many of the transitions are observed to be provoked by a sawtooth crash. The transition is most often followed by a quiescent "ELM-free" phase of at least 20ms, and later by small ("mossy") or large, probably type I, ELMs [3].

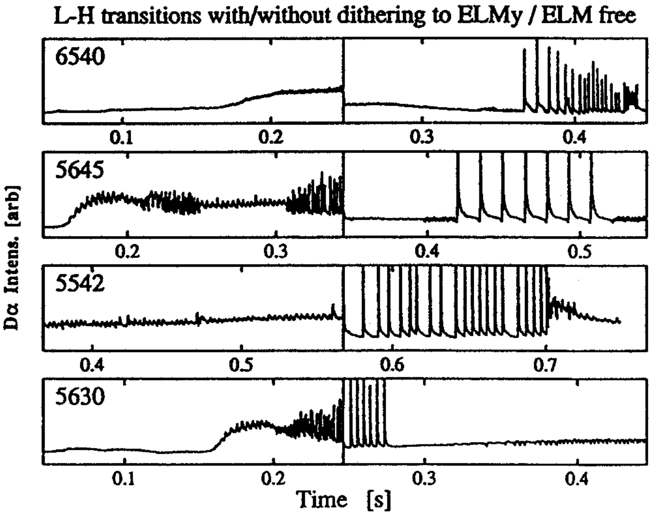

Figure 2:
Examples of different Dα intensity behaviour across the H-mode transition

3. Transition Threshold

3.1 Comparison with Power Threshold Scaling

With ohmic heating only, the existence of a power threshold (as proposed in [4] as a scaling of the power per unit surface crossing the last closed flux surface (P/S) with the product Bn_e) is not easily determined. Each configuration requires a certain minimum current in order to enter H-mode which limits operation to $2.1 \leq q_{95} \leq 3$. Following the L-H transition, the loop voltage often decreases by ~30% and the plasma density rises due to the improved particle confinement. The loop voltage is also observed to increase with plasma density both before and during the H-mode.

Thus, in a discharge with constant shape and plasma current, P/S is a fairly linear function of density. Figure 3 illustrates a TCV discharge in which the locus of P/S Bn_e follows the power scaling law until the discharge passes into H-mode. Although, in general, the plasma parameters at the transition are in agreement with the proposed power scaling [1], the subsequent decrease in the heating power and the concurrent density rise imply that the neutral particle beam power determined P/S, Bn_e law is less relevant as a description of the ohmic H-mode transition.

3.2 Behaviour with Density

The wide flexibility of TCV for the generation of varied plasma shapes and the easy access to the ohmic H-mode permit an examination of the density threshold as an independent function of a number of parameters, such as elongation, triangularity, wall separation, wall conditioning etc. In TCV, H-modes have been observed with a line averaged threshold plasma density in the range 1.7 to 7.1 x 10^{19} m^{-3}.

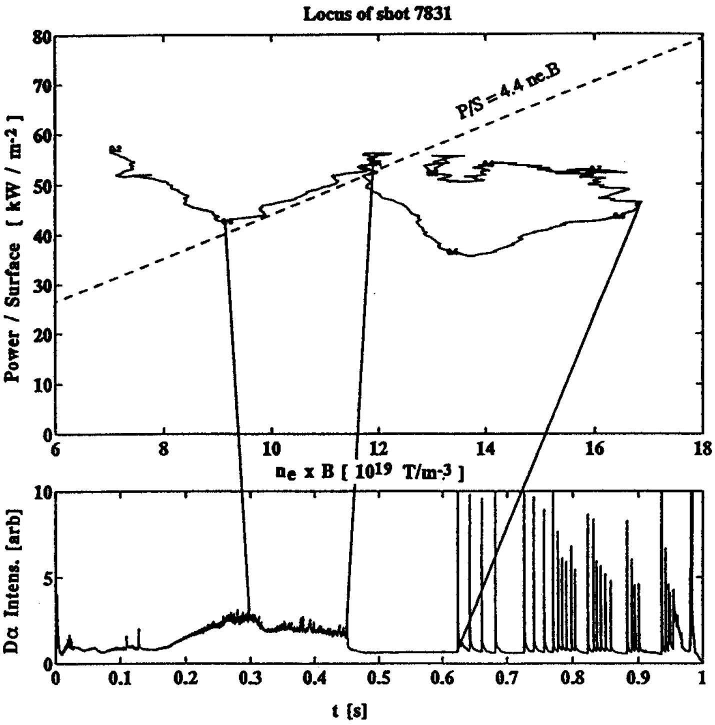

Figure 3:
The locus of the P/S against Bn_e for a SNU discharge. The Dα trace as a function of time is shown together with lines indicating the pre-H-L, H-L and post-H-L periods

Effect of wall conditioning: At present, graphite protection tiles cover ~64% of the vessel surface including, the entire central column and the top and bottom divertor target zones. The well known tendency for uncontrolled gas release from carbon surfaces coupled with the open divertor configurations of TCV, mean that the local recycling effects and wall conditioning may be expected, and are in fact observed, to have a strong influence on the transition threshold. For the SNU configuration of Fig1a, with Ip parallel to $B\phi$ (both ACW looking from the top of the machine), fresh boronisation and prolonged helium glow results in ELMing H-mode plasmas, with the ELMs becoming rarer with successive discharges and with the density threshold for the transition generally increasing. The consequent ELM-free H-modes often terminate in high density disruptions and further periods of He glow are required both to recover the ELMs and reduce the density threshold. Eventually, only ELM free H-modes are possible and a further boronisation is necessary to restore the initial conditions. Interestingly, inverting the direction of $B\phi$ appears to change the character of the H-mode in SNL discharges (ion ∇B drift again directed towards the X-point). Dithering phases and large ELMs are virtually absent and the discharges show a significant number of H-L-H transitions despite repetitive He glows and further boronisation. This is in contrast to the SNU ($B\phi$ ACW) where repeated H-L-H transitions are observed only in discharges following a long post-boronisation period. The reasons for the differences are as yet unknown and are under further investigation.

Effect of plasma shape: Results of a series of SNL experiments in which the density threshold is measured as separate functions of plasma elongation, plasma triangularity and wall separation are inconclusive. The density threshold is, for example, observed to rise by 100% as the plasma elongation is increased from 1.5 to 1.65, whereas a different series of similar discharges showed less than 30% change. Varying these parameters changes the position of the divertor strike points and is therefore also likely to influence the local recycling. Figure 4 shows the variation of the density threshold as a function of the upper triangularity, δ_u for SNL discharges (Fig 1b). Here the divertor magnetic geometry and the lower triangularity remain virtually unchanged with δ_u varying from 0.14 to 0.26 (elongation varied only slightly from 1.58 to 1.60). A clear and reproducible scaling is observed in which the density threshold increases linearly by 80% as δ_u increases.

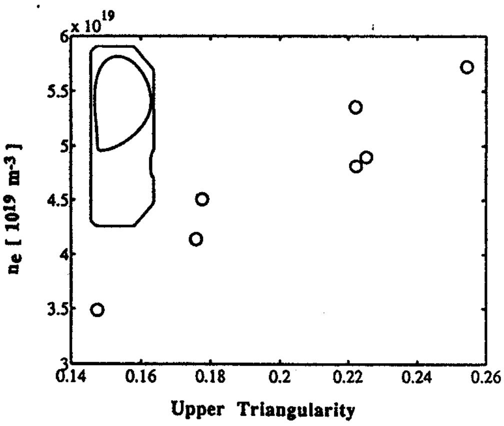

Figure 4:
The scaling of the density threshold for the H-L transition with upper triangularity

5. Conclusion

Under boronised wall conditions, ohmic H-mode transitions in TCV are observed in a variety of SN, DN and limited equilibria provided that in the SN configurations the ion ∇B drift be directed towards the X-point. With ohmic heating alone, since the heating power depends on the density via the loop voltage, it is difficult to determine a power threshold for the transition. A clear density threshold is, however, observed for configurations with easy access to the H-mode. This threshold can vary strongly with time and appears to be strongly influenced by wall recycling, leading to poor reproducibility in experiments designed to quantify the threshold dependence on plasma shape parameters. For a series of discharges in which recycling effects were minimised, an increase in the density threshold of 80% was observed as the upper triangularity of a SNL configuration was increased from 0.14 to 0.26.

Acknowledgements: This Work was partially supported by the Fonds National Suisse de la Recherche

References

[1] F. Hofmann et al. Plasma Phys. Control Fusion **36** B277, 1994

[2] J.-M. Moret et al. *Ohmic H-mode and confinement in TCV*, at this conference (invited)

[3] H. Weisen et al, *Edge Localised Modes in the TCV Tokamak*, at this conference.

[4] Ryter et al., 20th EPS Conference, Lisbon, 1993, ECA Vol 17C, I-23.

Comparison of Experimental and Theoretical Growth Rates of the Vertical Instability in TCV

M.J. Dutch, F. Hofmann, O. Sauter, D.J. Ward, M. Anton and J.-M. Moret
Centre de Recherches en Physique des Plasmas, EPFL
Association EURATOM-Confédération Suisse, CH-1015 Lausanne

1. Introduction

One of the principal aims of the TCV tokamak [1,2] is to produce plasmas with very high elongation ($\kappa \leq 3$). These plasmas are highly unstable with respect to axisymmetric ($n=0$) modes and require both active and passive stabilization. The maximum vertical growth rate that can be stabilized is of the order of the inverse of the response time of the power supplies which are used for the active stabilization [2].

When a new discharge scenario is prepared, it is of crucial importance to have some theoretical knowledge of the time evolution of the vertical growth rate and thus of the feasibility of the scenario. Vertical growth rate calculations have been performed for TCV [3,4] using the NOVA-W code [5]. In order to validate our theoretical model, we have measured the open-loop vertical growth rate for a variety of TCV plasmas and we compare the results with the model predictions. Single-parameter scans were used to measure the dependence of the growth rate on plasma elongation, triangularity and initial vertical position.

Growth rates were measured by opening the vertical (and radial) feedback control loops with fixed coil currents and observing the exponential growth of the vertical displacement via the magnetic and soft X-ray diagnostics.

2. Machine

The design of the TCV tokamak is a compromise between maximum shape flexibility and good passive vertical stability. The poloidal field system consists of an Ohmic transformer and 16 independently driven shaping coils located between the vacuum vessel and the toroidal field coils. The shaping coils are driven by thyristor-controlled power supplies with a response time of the order of 1ms. The TCV Plasma Control System used to feedback control the plasma position and shape is based on analog-digital hybrid matrix multipliers. The feedback cut was achieved in hardware by a pre-programmed switch to a new set of control matrices, in which the vertical and radial feedback gains are set to zero.

Poloidal arrays of 38 magnetic pickup coils (inside the vacuum vessel) and 38 flux loops (outside the vacuum vessel) are used as inputs to the feedback control loop.

The vacuum vessel is a 15-20mm thick continuously welded structure with a low toroidal resistance (55μΩ) and a nearly rectangular cross-section (height to width ratio of 3). The m=1 shell time ,γ_s^{-1}, is 8.2ms.

A set of internal coils driven by a fast power supply (response time ~ 0.1ms) has recently been installed inside the vacuum vessel. Calculations made using NOVA-W [3] show that using these fast coils in combination with the slower shaping coils should allow the stabilization of growth rates of the order of 2500 s^{-1}

3. Experimental Growth Rates

The growth rate of the vertical instability has been experimentally measured in TCV in a variety of low-current (250kA) discharges. Low current discharges were used in order to minimize the harmful effects of repetitive disruptions. Vertically centred plasmas were employed to maximize the growth rates by minimizing the wall-stabilizing effects (see Fig 3c). Fig. 1 shows an example of a vertical feedback cut during the current flat-top (t=0.47s) and the subsequent vertical displacement of the plasma.

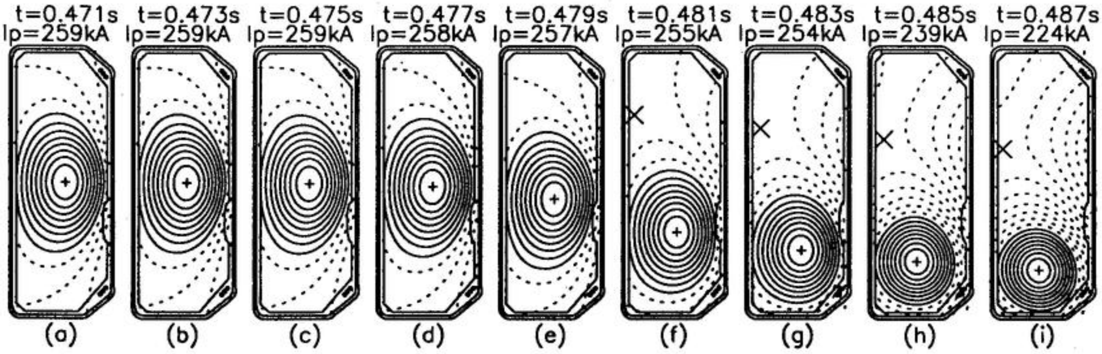

Fig. 1 Loss of vertical position control following feedback cut (control matrix switch) at 0.47s.(Shot #7617)

We limit the growth rate analysis to small displacements ($\Delta z \leq 4$cm), where the plasma current and cross-section are constant. During this time ($t \leq 0.477$s in Fig. 1), the plasma motion is purely vertical and essentially rigid.

The series of limiter configurations under study (Fig. 2) cover a range of elongation ($1.4 \leq \kappa_{edge} \leq 1.75$), triangularity ($0.1 \leq \delta_{edge} \leq 0.65$) and vertical position ($0 \leq z \leq 0.29$m).

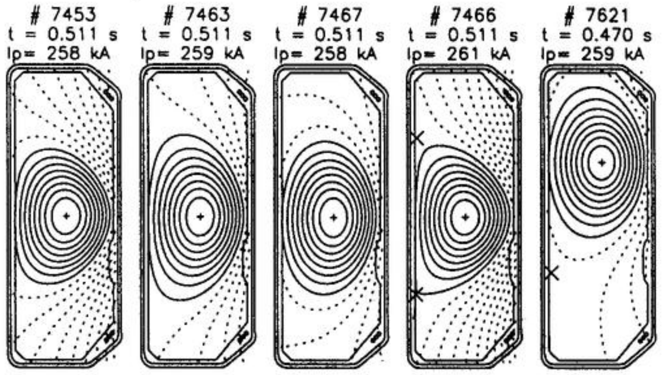

Fig. 2 Plasma configurations: extremes of elongation, triangularity and initial vertical position.

Fig. 3 shows experimental and modelled growth rates as a function of the global plasma parameters κ, δ and z. Experimental growth rates are calculated from the realtime Ip*z observer used for feedback control of the vertical position, and a full equilibrium reconstruction, LIUQE [6]. Also shown is the growth rate estimated from the centroid motion of the tomographically reconstructed soft X-ray emissivity. The soft X-ray diagnostic consists of a poloidal array of 10 cameras with a total of 200 viewing chords. An overall comparison of experimental and theoretical growth rates is presented in Fig. 4, for all the discharges included in this study.

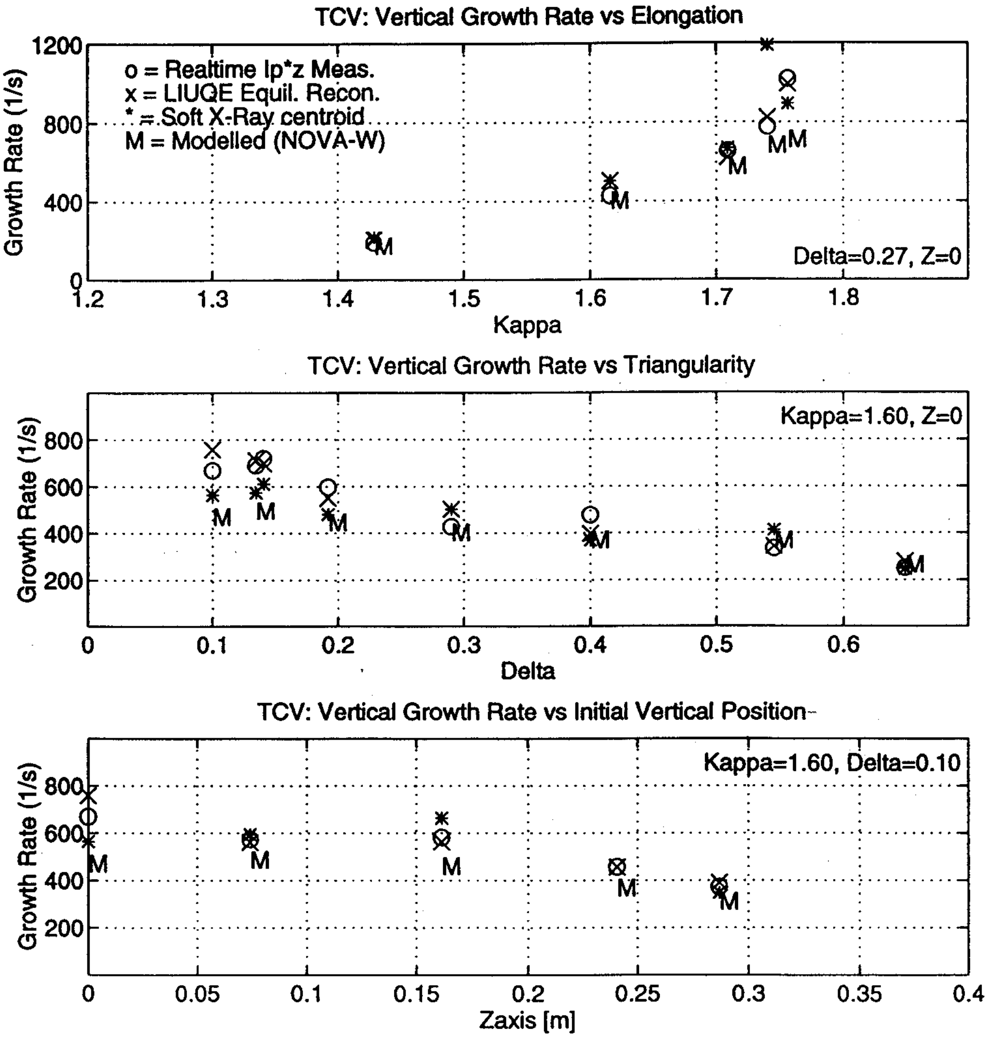
TCV: Vertical Growth Rate vs Elongation

TCV: Vertical Growth Rate vs Triangularity

TCV: Vertical Growth Rate vs Initial Vertical Position

Fig. 3 Comparison of experimental and theoretical vertical growth rates in TCV as a function of a) elongation, b) triangularity and c) initial vertical position.

4. Modelling of Growth Rates

Vertical growth rates are modelled in TCV using NOVA-W, which is a non-variational MHD stability code that includes the effects of a resistive wall and active feedback circuits, as well as plasma deformability.

The equilibrium reconstruction code LIUQE is used to routinely determine the plasma parameters on a two-dimensional rectangular grid, (r,z), after each discharge. An intermediate equilibrium code, CHEASE [7], maps the 2-D quantities produced by LIUQE from a cartesian grid to flux coordinates, in a form which is suitable for NOVA-W.

5 Discussion

Experimental and theoretical open-loop vertical growth rates have been compared in TCV and generally agree to within 20%. The largest differences (≥30%) occurred for the most highly unstable plasmas. Growth rates calculated by NOVA-W are systematically lower than those measured in the experiments. This may be due to slight profile errors in the equilibrium reconstruction, or the presence of a large number of diagnostic ports which are not treated by NOVA-W. Single-parameter scans of plasma elongation and triangularity show that the vertical growth rate increases strongly with elongation, highlighting the importance of active vertical position control, whilst positive triangularity has a stabilizing effect in these discharges. A series of similar discharges in which the plasma is progressively shifted towards the top of the vacuum vessel (Fig. 3c) clearly demonstrates the stabilizing influence of the conducting vessel wall. Growth rates up to 1000 s^{-1} have been stabilized in TCV using only the shaping coils outside the vacuum vessel. Incorporation of the fast-acting internal coils into the vertical position control loop should permit stabilization of the highest elongation configurations envisaged in TCV.

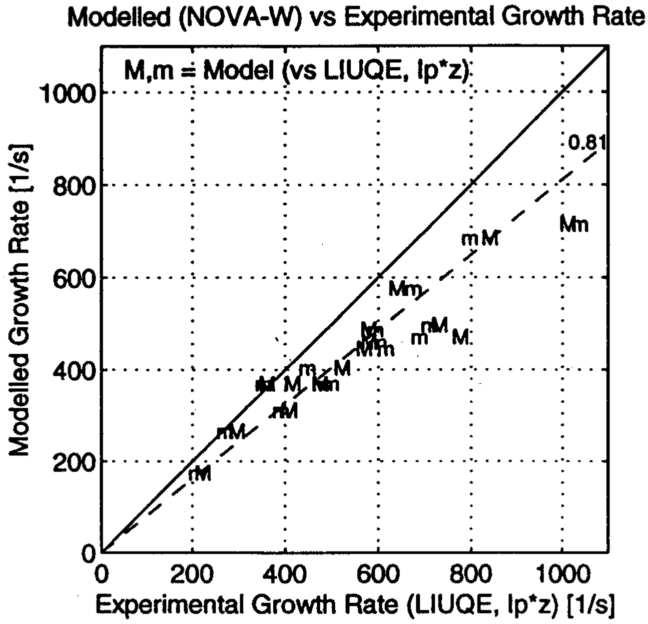

Fig. 4 Comparison of vertical growth rates in TCV

Acknowledgements: It is a pleasure to acknowledge the support of the entire TCV Team. This work was partly supported by the Fonds National Suisse de la Recherche Scientifique.

References:

[1] J.-M. Moret et al., this conference (Invited)
[2] F. Hofmann, J.B. Lister, et al, Plasma Phys. Contr. Fusion **36**, (1994) B277.
[3] Ward, D.J., Hofmann, F., Nuclear Fusion **34** , (1994) 401.
[4] Ward, D.J., Bondeson, A., Hofmann, F., Nuclear Fusion **33**, (1993) 821.
[5] Ward, D.J., Jardin, S.C., and Cheng, C.Z., J. Comput. Phys. **104**, (1993) 221.
[6] Hofmann, F., Tonetti, G., Nuclear Fusion **28**, (1988) 1871.
[7] Lütjens, H., et al, Comput. Phys.Commun **69**, (1992) 287.

Spectral and Angular Dependence of Photodiode Response to Soft X-Rays

M. Anton, M. J. Dutch and H. Weisen
Centre de Recherches en Physique des Plasmas, Association EURATOM - Confédération Suisse
École Polytechnique Fédérale de Lausanne, CH-1015 Lausanne, Switzerland

Introduction

Planar arrays of photodiode detectors for soft X-ray tomography on magnetic fusion devices have become very popular. They are economic and allow very compact camera designs. Unlike X-ray cameras based on single element detectors placed on a semicircle around the pinhole, the angle of incidence is different for each diode of such an array. Since uniformity of response is crucial for tomography we have investigated the effect and ways to compensate for it.

Modeling of pn-Photodiode Response

We adopt a simplified model [1, 2] to calculate the efficiency of n-type Si pn photodiodes[1]. Below the Si_3N_4–passivated surface the substrate of thickness D is strongly doped. Passivation and p+-zone form a dead layer of thickness d with a transmission $\tau = exp(-\alpha_d d)$. The probability $p(x)$ of detecting a charge generated within the depletion zone of thickness V is unity, whereas for charges generated at a distance x from the junction $p(x) = exp(-x/L_p)$. L_p is the diffusion length of the minority carriers. The responsivity equals $r = r_0 \times \tau \int \alpha \ \exp(-\alpha x)\ p(x)\ dx$. $r = r_0\eta$ where $r_0 = e_0/E_{e^- - hole} = 1/3.63\ AW^{-1}$. The efficiency η then is

$$\eta(\nu,\theta) = \tau[1 - \frac{\exp(-\alpha V)}{1+\alpha L_p}(1+\alpha L_p \exp[-(\alpha + 1/L_p)(D-V)])], \quad \alpha = \frac{\alpha(\nu)}{\cos(\theta)}. \quad (1)$$

Values of the absorption coefficients α were taken from [3]. For radiation with a spectral power distribution $w(\nu)$ (units $AW^{-1}Hz^{-1}$), we define a spectrum averaged efficiency $<\eta>$ as

$$<\eta> = \int \eta(\nu) w(\nu) d\nu / \int w(\nu) d\nu, \quad (2)$$

$<\eta>$ multiplied by r_0 equals the photocurrent induced by $1W$ of radiation with a spectral distribution $w(\nu)$.

---

[1] In the following we always refer to CENTRONIC LD20-5T arrays in photoamperic mode, $D = 380\mu m$, $V = 3\mu m$ [4]

Determination of Diode Efficiencies from Angular Dependences

The spectral efficiency $\eta(\nu)$ can be determined from measurements of angular dependences of the diode signal using monochromatic light [5]. We have applied a similar approach using a commercial X-ray source. With the help of PHA-spectra of our X-ray source for $10kV$ and $30kV$ we were able to calculate $<\eta>$ as a function of the unknown parameters L_p and d, *i.e.* $<\eta>=<\eta(\theta, L_p, d)>$. Comparison of theoretical and experimental photodiode current densities j following

$$\frac{j_{diode}(50^o)}{j_{diode}(0^o)} = \frac{<\eta(50^o, L_p, d)>}{<\eta(0^o, L_p, d)>}. \tag{3}$$

yielded approximate values of L_p and d. $\eta(\nu)$ is then determined by (1). Note that *only relative measurements* are required.

We have applied the method to CENTRONIC LD20-5T arrays which equip the soft X-ray cameras of the TCV tokamak. Typical diffusion lengths are $\approx 200\mu m$, the dead layer thickness varies between $0.5 - 0.8\mu m$. Details may be found in [6].

Angular Dependence of $<\eta>$ for Radiation from a Plasma

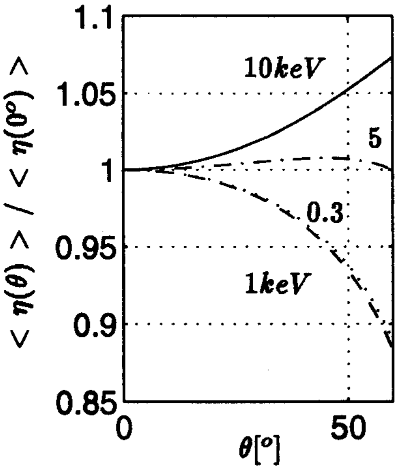

Figure 1: $<\eta(\theta)>$ / $<\eta(0^o)>$ for $47\mu m$ curved Be, $L = 200\mu m, d = 0.5\mu m$

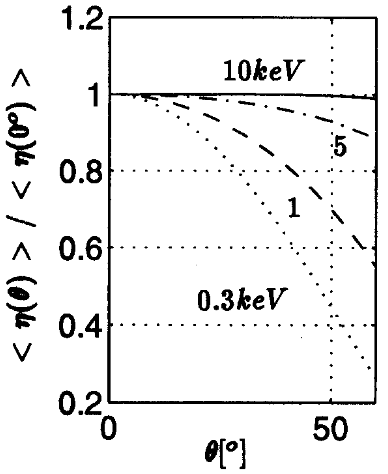

Figure 2: $<\eta(\theta)>$ / $<\eta(0^o)>$ for $47\mu m$ flat Be, $L = 200\mu m, d = 0.5\mu m$

We have calculated $<\eta>$ as a function of the angle of incidence θ for soft X-rays from a thermal plasma using [7]

$$w(\nu) = \int_0^1 \frac{\exp(-h\nu/kT_e(\rho))}{\sqrt{kT_e(\rho)}}\, d\rho \quad \text{with} \quad T_e(\rho) = T_e(0) \times (1-\rho^2) \tag{4}$$

which is a reasonable fit to spectral distributions seen in many fusion devices. Figures 1 and 2 display $< \eta(\theta) > / < \eta(0^o) >$ for $kT_e(0) = 0.3, 1, 5, 10keV$. To obtain fig. 1, $w(\nu)$ was multiplied by the transmission factors of $47\mu m$ thick Be independent of θ. This corresponds to the soft x-ray cameras on TCV and ALCATOR C-mod which are equipped with curved Be foils. For fig. 2, the Be foil was assumed to be flat, *i.e.* the effective thickness varies like $1/\cos(\theta)$.

As a result, we see that the actual angle of incidence has to be taken into account for the calibration. Otherwise errors of up to 10% at $\theta = 60^o$ may result, even if the Be foil thickness is θ-independent. For a flat foil, errors may exceed 40%.

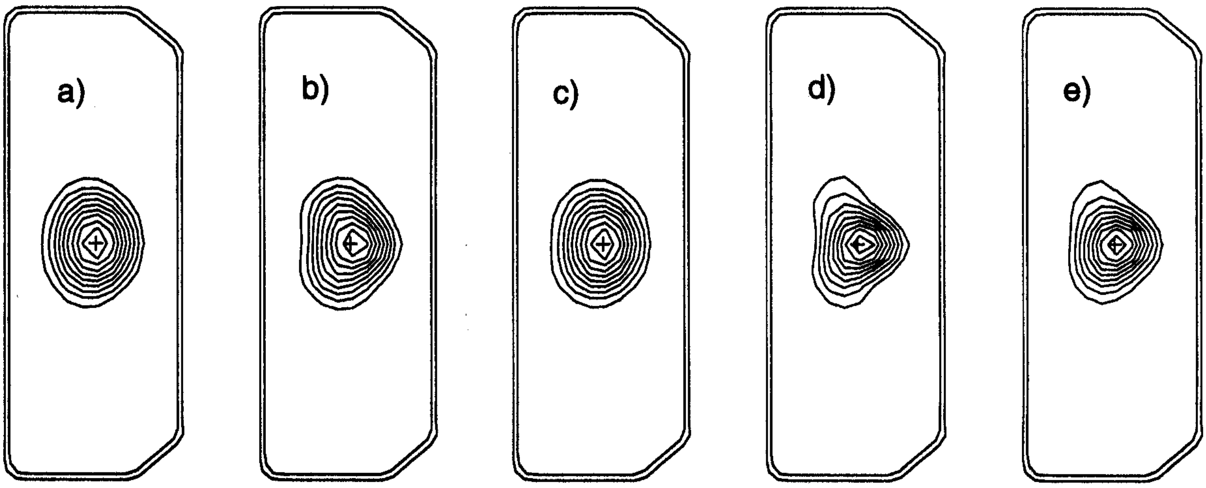

Figure 3: a) simulated emissivity distribution, b) reconstruction from uncalibrated, simulated data, c) from simulated, calibrated data, d)from experimental, uncalibrated data, e)from experimental, calibrated data. Calibration with $< \eta(\theta) >$. Granetz method, $\ell_{max} = 8, m_{max} = 3$

A more sophisticated approximation of the spectral distribution than (4) can be obtained using actual results from other diagnostics such as magnetics or Thomson scattering. We have simulated the spectral plasma emissivity of TCV discharge # 7067 at $t = 0.497s$, using the flux contours ψ from magnetic reconstruction, assuming a flat density profile and $T_e = 0.6keV \cdot \psi_{norm}^{0.8}$,where $\psi_{norm} = \psi/\psi_{axis}$. Fig 3 shows some examples of tomographic inversions using the Cormack-Granetz method [8] with $\ell_{max} = 8$ and $m_{max} = 3$. Part a) shows the simulated emissivity profile, b) is a reconstruction based on the simulated, uncalibrated detector signals, making use of the actual parameters D, d, V and L_p of the 180 diodes installed on TCV. Part c) shows a reconstruction using the same artificial dataset, calibrated with $< \eta >$, where $w(\nu)$ is taken from the simulation. Part

d) represents a reconstruction of uncalibrated, *experimental* data, for e) the experimental data were calibrated with the same factors as c).

Although this correction is possibly not yet sufficient (n-type Si photodiodes may become unstable, see [9]), the results displayed in fig. 3 clearly show that a calibration using $< \eta(\theta) >$ improves the accuracy of the tomographic reconstruction.

Acknowledgements

We gratefully acknowledge fruitful discussions with *Roland Payne* from CENTRONIC as well as the communication of LD20-5T specifications. We also thank *Thierry Buchillier* and the 'Institut de Radiophysique Appliquée', Lausanne, for providing spectra of our X-ray source. This work was partly supported by the *Swiss National Science Foundation.*

References

[1] *KINGSTON, R H:* 'Detection of Optical & Infrared Radiation' Springer (1978)

[2] *SZE, S M:* 'Physics of Semiconductor Devices', 2nd ed. Wiley, New York (1981)

[3] *VEIGELE, W M J:* Atomic Data **5**, No. 1 (1973)

[4] *CENTRONIC:* main catalogue and private communication

[5] *KRUMREY, M and TEGELER, E:* Rev. Sci. Inst. **63** (1) (1992)

[6] *ANTON, M, DUTCH, M J and WEISEN, H:* Rev. Sci. Inst., probably July (1995)

[7] *MIYAMOTO, K:* 'Plasma Physics for Nuclear Fusion', MIT Press (1976)

[8] *GRANETZ, R S and SMEULDERS, P:* Nuclear Fusion **28** 3 (1989)

[9] *TEGELER, E and KRUMREY, M:* Nucl. Inst. Meth. **A 282** 701 (1989)

Ultra-soft X-ray Spectroscopy using multilayer mirrors on TCV

H. Weisen*, V. Piffl+, A. Krejci+, J. Moravec+, J. Raus+, M. Dutch* and P. Paris*
*Centre de Recherches en Physique des Plasmas, Association EURATOM-Suisse
Ecole Polytechnique Fédérale de Lausanne, 1015 Lausanne, Switzerland
+Institute of Plasma Physics, Czech Academy, Prague, Czech Republic

The TCV tokamak has recently been equipped with an ultrasoft X-ray multichromator allowing low resolution ($\lambda/\Delta\lambda \approx 30$) measurements in the energy range 200-800 eV. Its purpose is to monitor emission from the main resonance lines of highly ionized light impurities such as Boron, Carbon and Oxygen. Wavelength selectivity is achieved by synthetic multilayer mirrors (MLM) [1,2] having 30-40 alternate layers with layer periods in the range 30 to 70Å depending on the wavelength range to be investigated.

1. Spectrometer design

The spectrometer developed at the IPP Prague is of the θ-2θ design (fig. 1). The centre wavelength of each of the 4 channels of the device can be independently adjusted while maintaining alignement. This is achieved by mechanically coupling the mirror incidence angle and position, as well as the detector orientation. The channeltron dectectors are housed in a cylindrical soft iron magnetic shield with a total thickness of 4 cm to guard them from the poloidal fields (~0.1 T) at its location 1.5 m above the TCV vacuum vessel. Russian type VEU-6 channeltrons with a gain of 10^7 and a maximum count rate of 0.5 MHz are used with tungsten photon-electron converters biased to -400 V at the channeltron input. Although this leads to a approximately four-fold reduction in overall sensitivity as compared to an open channeltron, it has the advantage of a uniform response accross the detector surface.

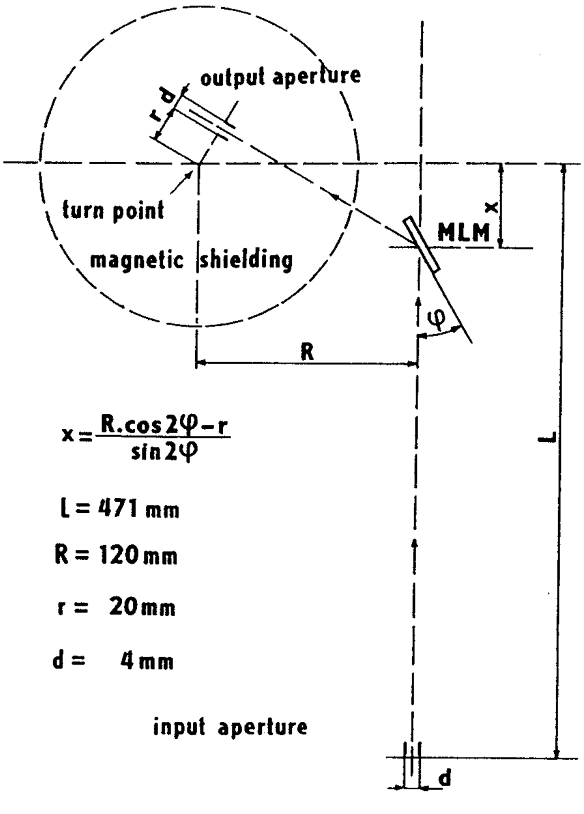

Fig. 1. Geometry of ultra-soft X-ray multichromator. Detectors are inside the magnetic shielding outlined by the broken circle. Separation from the TCV vacuum is achieved by polymer foils placed below the input aperture.

Pulse shaping electronics are included in the channeltron package. The flat multilayer mirrors were fabricated at the Institute of Applied Physics, Nizhnij Novgorod, Russia. The four channels of the device use different mirrors optimized for the ranges 200-300, 300-400, 400-500 and 500-800 eV respectively.

The vacuum of the apparatus is separated from the TCV vacuum by 0.3 µm thick polymer foils supported by silicon grids[3] which withstand pressures in excess of 1 bar and have acceptable absorption in the energy range of interest. We found that transmission of undesirable VUV radiation through the polymer window was still significant, as indicated by radiation spikes at breakdown and during plasma termination. Thin (0.2µm) film metal filters have therefore been inserted between the polymer vacuum window and the entrance aperture of the instrument. The characteristics of the components were measured at the IOFFE Institute in St. Petersburg, Russia and are summarized in table 1 for the energies corresponding to the strongest lines from hydrogen-like stages of B,C,N and O.

Table 1. Characteristics of spectrometer components at 4 typical photon energies

E (eV)	ΔE (eV)	R_{MLM}	T_{window}	Filter	T_{filter}	η_{chan}
255	15	0.23	0.45	Ag	0.062	$3.3 \cdot 10^{-3}$
367	13	0.12	0.26	Ag	0.125	$5.7 \cdot 10^{-3}$
501	32	0.13	0.46	Sn	0.12	$6.7 \cdot 10^{-3}$
654	22	0.10	0.53	Ni/C	0.38	$6.3 \cdot 10^{-3}$

The throughput defined as $\xi = A\Omega \cdot T_{filter} \cdot T_{window} \cdot R_{MLM} \cdot \eta_{chan} \Delta E$, is shown as a function of photon energy in fig. 2, where $A\Omega$ is the étendue of the instrument, T stands for transmission, R_{MLM} is the mirror peak reflectivity, η_{chan} the channeltron quantum efficiency and ΔE the energy resolution.

2) Results

The vertically viewing instrument is placed slightly outside the magnetic axis position, with viewing lines crossing the plasma midplane at r/a~0.4. This is not a limitation since most of the line radiation investigated originates from the plasma periphery. Normally the instrument is left to monitor a selected set of lines. Typical count rates for Carbon are 50 kHz in L-modes and 200 kHz in H-modes. In a demonstration experiment a spectrum over the full range was built up in a series of reproducible discharges in L-mode with the following parameters: B_T=1.43 T, Ip = 400 kA, $\langle n_e \rangle \approx 5 \cdot 10^{19} m^{-3}$, R=0.89m, a = 0.24 cm, κ=1.5, Te(0) ≈ 600 eV. The discharges were limited on carbon tiles covering the inner wall. The results in fig. 3 are averages over the ~1 s flat-top of the discharges and show clear peaks at the energies of the main lines of BIV (206 eV), BV (255 eV), CV(308 eV), CVI (367 eV), OVII (574 eV) and OVIII (654 eV). The vessel had not been boronized since the last shut-down when approximately half of the carbon tiles had been replaced. The Boron detected was a remnant from the inner wall tiles which had not been replaced. No Nitrogen or Iron lines were positively identified.

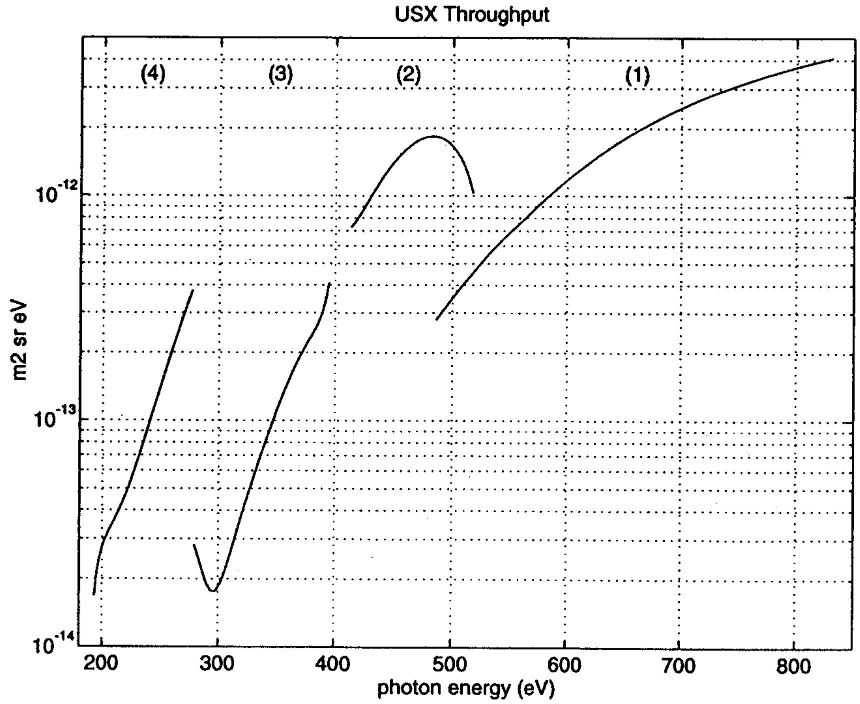

Fig.2. Throughput of the 4 channels of MLM based multichromator

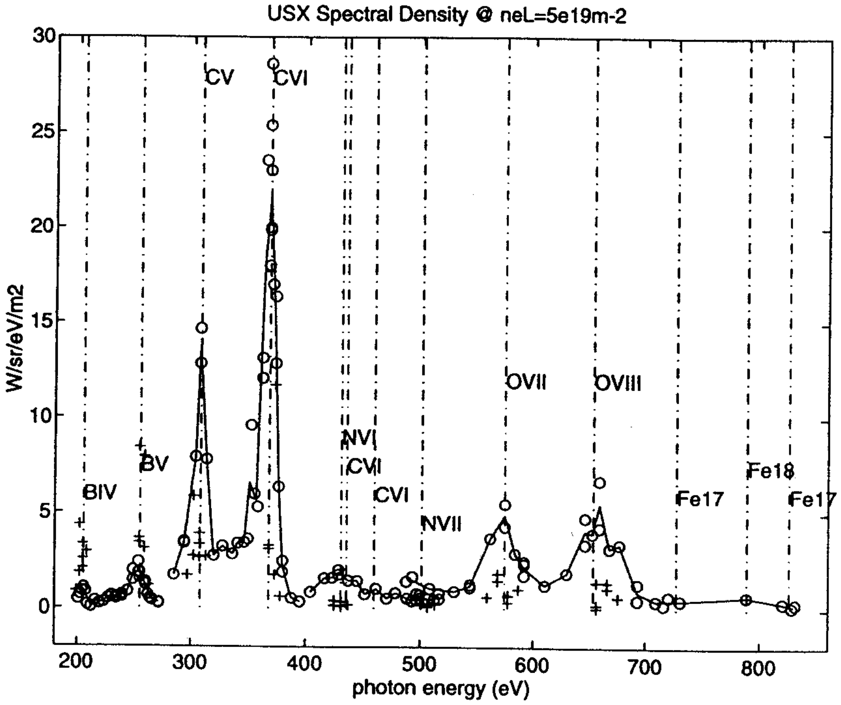

Fig.3 Ultra-soft X-ray spectrum obtained by a shot-to-shot scan of photon energy.

The main lines were revisited a few days (70 discharges) after a fresh boronization ('+' symbols on fig.3). Unfortunately these discharges were not very reproducible and not identical to those of the spectral scan. Oxygen signals were reduced by a factor of 5, Carbon signals by a factor of 2-4, Boron was enhanced by a factor of 2-4.

For the first 50 discharges following the boronisation the Boron signals remained one order-of magnitude above their pre-boronization levels. During the first few shots the impurity concentration estimated from X-rays emitted from the plasma core[4] was nearly a factor of 2 above its pre-boronization level despite a five-fold reduction in Oxygen and Carbon. This is attributed to Boron being substituted to Carbon as the main light impurity immediately following a boronization. An exact evaluation of the effect of boronization is not possible with the presently available data, because impurity signals are also observed to be sensitive to the very variable operating conditions in TCV, with different wall areas being exposed to the plasma at different times.

Since absolute transmission and sensitivity data are available for all of the components a determination of absolute impurity levels is possible if coronal equilibrium can be assumed. For the discharges use in fig. 3 (before boronization) the absolute line emission from hydrogen like impurity ions is consistent with coronal equilibrium modelled using the IONEQ[5] code for $n_C/n_e \sim 2\%$, $n_B/n_e \sim 1\%$ and $n_O/n_e \sim 0.1\%$. However the ratio of intensity from the helium-like lines (such as CV at 308 eV) to the hydrogen like lines (such as CVI at 367 eV) is several times larger than expected from coronal equilibrium. This observation may be explained by inward transport of ions where the higher electron temperature leads to strongly enhanced excitation rates before ionisation to the next stage takes place. Preliminary IONEQ calculations using diffusion coefficients of a few m^2/s are in qualitative agreement with our observations. The above concentrations, which together add up to $Z_{eff} \sim 1.9$ are therefore likely to be overestimates. This is corroborated by the above mentionned X-ray ($E>1.5$ keV) measurements which are mainly sensitive to fully ionized impurities in the core and are consistent with $Z_{eff} \leq 1.2$.

To conclude, the use of multilayer mirrors for spectroscopic measurements in the ultra-soft X-ray region allows the measurement of line emission from highly ionised light impurities in a way which is similar to the popular filter methods in the visible wavelength range for lower ionisation stages. Present results indicate that even helium-like and hydrogen-like ionization stages of light impurities are not in coronal equilibrium in TCV. It may be worth investigating the neutron resistance of MLMs since they may open up new diagnostics possibilities for the next generation of large fusion research devices.

Acknowledgements: This work was partly supported by the Fonds National Suisse de la Recherche Scientifique. The help of many colleages is gratefully acknowledged.

References:

[1] A P Zwicker, M Regan, M Finkenthal & H W Moss, Rev.Sci.Instrum 61 (1990) 2786
[2] V Piffl, J Badalec, AV Golubev, SV Bobashev, report IPPCZ-340, IPP Prague (1994)
[3] MOXTEK Inc. Orem 452W 1260N,Utah 84057, USA
[4] H Weisen, D Pasini, A Weller & AW Edwards, Rev. Sci. Instrum 62 (1991), 1531.
[5] Courtesy of A. Weller, IPP Garching, Germany

Edge Localized Modes in the TCV Tokamak

H. Weisen, M.J. Dutch, A. Pochelon, A. Hirt, R.A. Pitts, F. Hofmann, M. Anton,
B.P. Duval, J.B. Lister, J.-M. Moret, Ch. Nieswand, and G. Tonetti
Centre de Recherches en Physique des Plasmas, EPFL
Association EURATOM-Confédération Suisse, CH-1015 Lausanne

1. Introduction

The TCV tokamak [1] has produced a large number of diverted SN and DN plasmas, as well as limited plasmas. Following boronization in 1994 virtually all discharges with the ion ∇B drift towards an X-point and several elongated limited plasmas have produced Ohmic H-modes [2]. The typical SN discharge shown in fig.1 demonstrates most of the features observed in H-modes. Transitions can be 'dithering', with the D_α level switching between L-mode and H-mode levels. They can also feature ELMs with pulses of D_α emission well above the L-mode level. Following the transition there generally is an initial ELM-free period. In the example presented there is a short period of irregular 'mossy' ELMs causing low amplitude fluctuations on the D_α signal, followed by several Large ELMs which significantly reduce the energy confinement time and interrupt the density rise and a final period of mossy ELMs. The plasma density rises rapidly in the absence of Large ELMs. Mossy ELMs have their largest amplitude in the divertor and do not appear to affect confinement. In the absence of Large ELMs H-modes frequently terminate in high density disruptions, sometimes at the Greenwald limit $<n_e>_{GL} = 0.27\ I_p/a^2$.

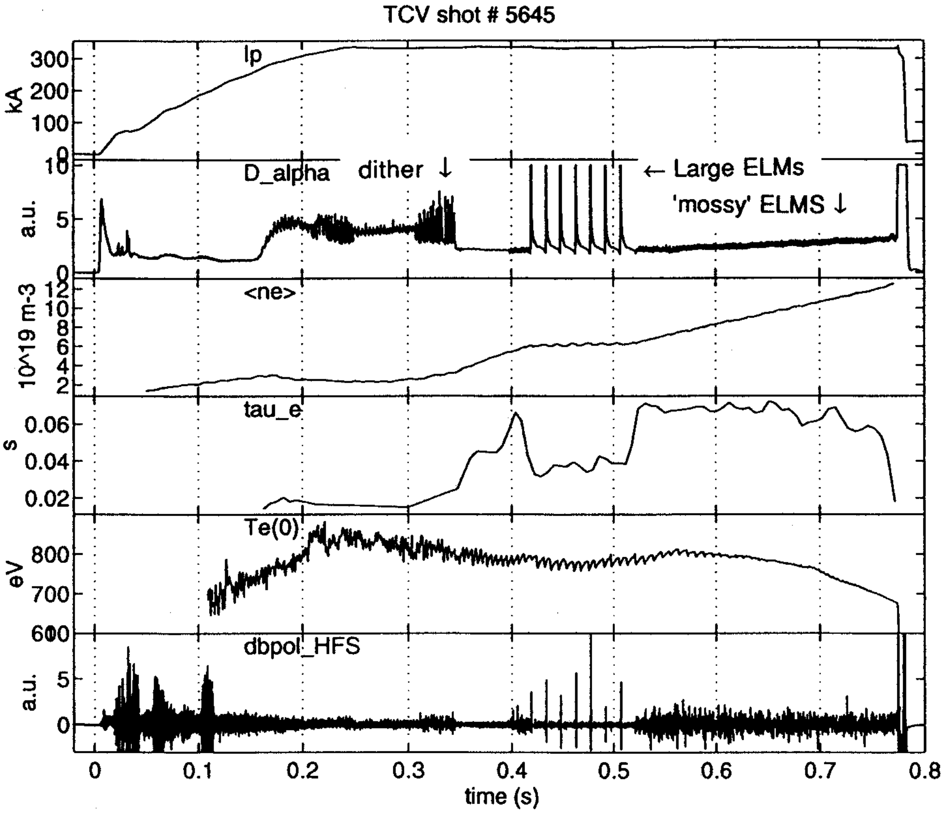

Fig.1 Typical Ohmic H-mode evolution in the Single-Null configuration (fig.2b)

2. Large ELMs

The magnetic signature of Large ELMs features a dominant m=1, n=0 (fast vertical displacement) together with an m=2,3, n=1 mode. Higher order modes could not be measured because of hardware limitations. Both coherent and turbulent precursors have been observed, beginning 0.1-3 ms before the D_α pulse.

ELM effects have been studied in detail in two configurations, a Double-Null D shaped configuration (DN) with κ=1.7, δ=0.7, Ip=390 kA and a Single Null configuration with the X-point at the top (favourable ion drift, SN) with κ=1.6, δ=0.4, Ip=330 kA (fig.2).

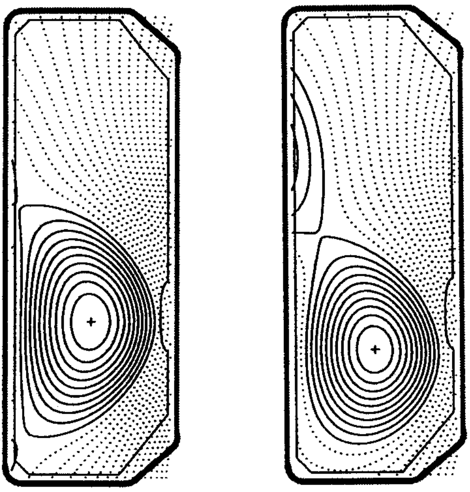

Fig.2 Configurations for ELM studies. Left: DN, right SN

In the SN plasmas these ELMs cause changes in electron content and stored energy of the order of 10% [3] . The X-ray emission from the plasma edge is dramatically affected. The emission rises at the arrival of heat pulses released by sawtooth collapses and falls as a result of the energy loss associated with each ELM. A single ELM may cause the emission to fall by a factor of 2 within 0.1 ms. It is interesting to note that in ELMy H-modes these discrete MHD events (sawteeth and ELMs) appear to dominate the power balance at the edge transport barrier. In DND the ELM effects are 2-3 times smaller.

The effect of ELMs on global confinement has been investigated as a function of ELM frequency. We may take a time average (over many ELMs) of the usual particle balance and obtain

$$\langle \dot{N}_{eff} \rangle / N = \Phi_{in}/N - 1/\tau_{up} + (\langle \Delta N \rangle / N) f_{ELM}$$

where the first term on the left hand side is the rate of change of the particle content averaged of many ELMs. τ_{up} stands for the underlying (ELM-free) particle confinement time and Φ_{in} is the particle source. Analogous expressions hold for the impurity content, N_Z, and the stored energy W.

The experimental time traces were divided into windows with roughly constant ELM frequency, for which quantities of interest and their rates of change were sampled. In both the DN and the SN cases the average rates of change in electron content from a 4 channel FIR interferometer, impurity content estimated from an X-ray measurement [4], stored energy from the equilibrium reconstruction vary nearly linearly with f_{ELM} up to a maximum frequency, ~300 Hz for DN and ~120 Hz for SN (figs.3 and 4). Above these frequencies irregular ELMs and returns to L-mode are often observed.

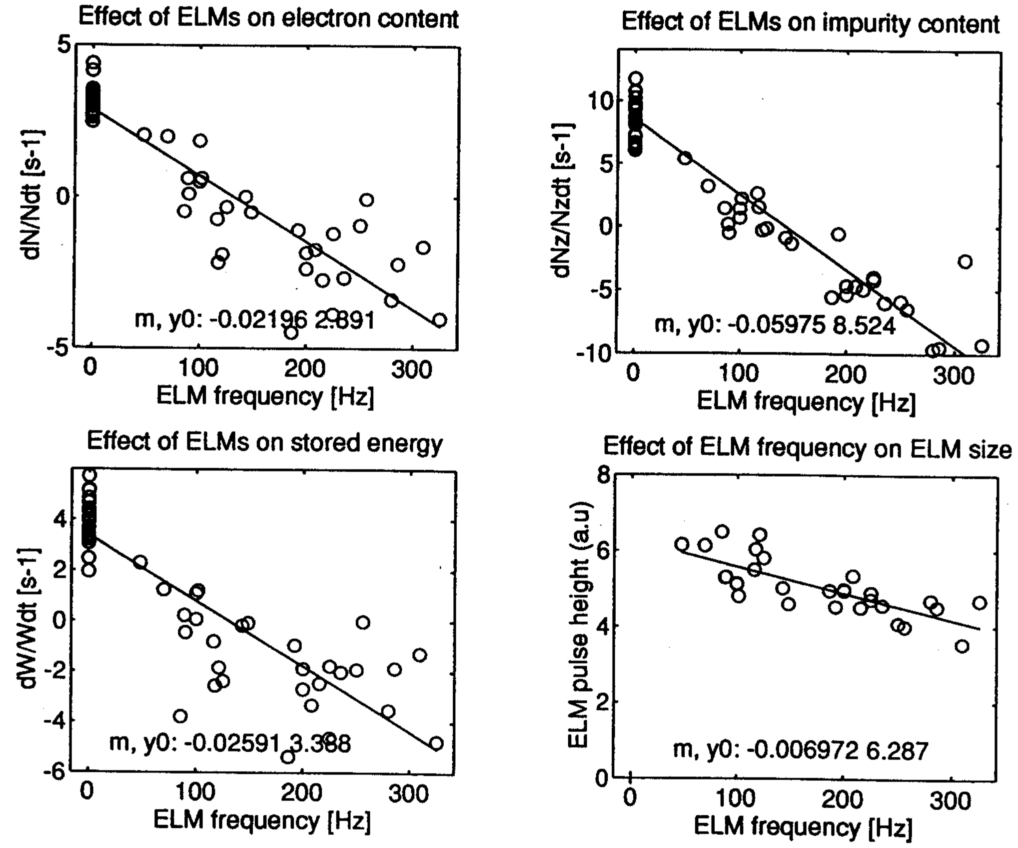

Fig. 3 *Rates of change of electron content, impurity content and stored energy versus ELM frequency in DN H-modes. The right bottom right figure shows the pulse height of the D_α emission.*

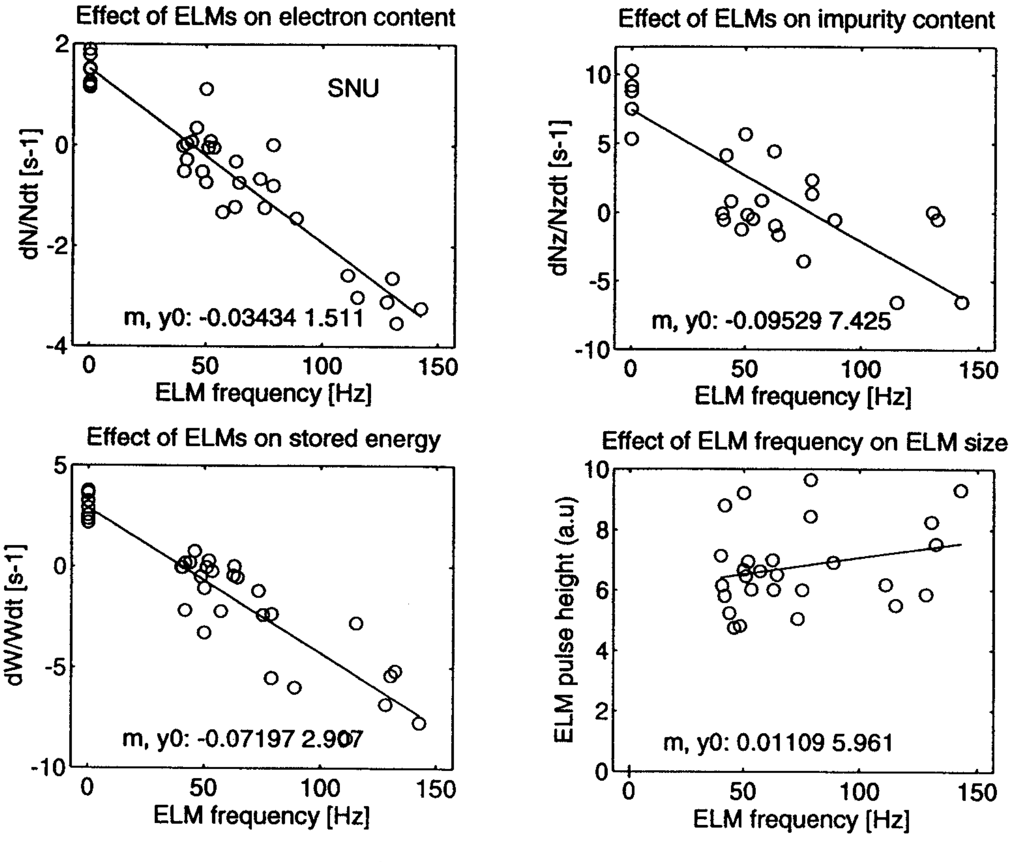

Fig. 4 *As fig.3 but for SN*

From the slopes of the fitted lines we see that in DND these ELMs expel on average 2% of the electron content, 2.5% of the stored energy and 6% of the impurity content. In SNU the corresponding numbers are 3.5%, 7% and 9%. The height of the D_α pulses, which may be indicative of ELM size, vary little with ELM frequency. These large numbers are confirmed by direct measurements of $\Delta N_e/N_e$ and $\Delta W/W$ in selected cases. Note that as far as particles are concerned the loss fraction should be taken as net since the gross outward flux caused by the ELMs may be partly offset by an influx due to ELM-enhanced recycling at the walls. Also the X-ray estimates for the impurity content, which are still based on a single chord and cannot take into account profile changes due to the ELMs, may be subject to revision when more comprehensive impurity diagnostics become available.

In DN stationary conditions are obtained for $f_{ELM} \approx 120$ Hz, with $<n_e> \approx 8\cdot10^{19}m^{-3}$, $Z_{eff} \approx 1.6$ and $\tau_e \approx 0.7\,\tau_{eu}$. In SN, stationary conditions with similar plasma parameters are obtained for $f_{ELM} \approx 50$ Hz, due to the larger ELM size.

3. Discussion

Although Large ELMs have been observed in ohmic H-modes in TCV, their large size and probable pressure (gradient) threshold, indicated by the requirement of an ELM-free period lasting for 20 ms or more before the first Large ELM occurs following an L-H transition, suggest they may be related to type I ELMs observed in devices with auxiliary heating. The instability threshold for Large ELMs also depends on configurational factors, as apparent from the ELM control experiments [5]. In these experiments in DN, Large ELMs were induced or inhibited depending on the sign of the imbalance of a DN configuration. When the ion ∇B drift was away from the 'active' X-point Large ELMs appeared after an initial ELM-free period. This opens up the possibility of controlling both the evolution of H-modes and the size (ΔW, ΔN) of the ELMs.

The smaller ELMs observed near L-H and H-L transitions may be of type III. We know of no counterpart, in other devices, of 'mossy' ELMs, although detachment instabilities have been suggested as an explanation [6].

Acknowledgements: This work was partly supported by the Fonds National Suisse de la Recherche Scientifique.

References:

[1] J.-M. Moret et al., this conference (invited)
[2] F. Hofmann, J.B. Lister et al, Plasma Phys. Contr. Fusion **36**, (1994) B277.
[3] H. Weisen et al., 17th Symp. Plasma Phys. and Techn., Prague, June 1995.
[4] H. Weisen, D. Pasini, A. Weller et al., Rev. Sci. Instrum **62** (1991) 1531
[5] M. Dutch, F. Hofmann, et al., accepted for Nuclear Fusion (Letters), 1995.
[6] M.A. Mahdavi, personal communication, June 1994

Direct Measurement of TAE, EAE and Multiple Kinetic TAE in JET

A.Fasoli[1], D.Borba, N.Delyanakis, J.A.Dobbing, D.J.Campbell, C.Gormezano, J.Jacquinot, A.Jaun[1], W.Kerner, H.Holties[2], P.Lavanchy[1], J.B.Lister[1], J.-M.Moret[1], L.Porte, S.Sharapov, L.Villard[1]

JET Joint Undertaking, Abingdon, Oxfordshire, OX14 3EA, UK

[1]*CRPP-EPFL, Ass. Euratom-Swiss Confederation, 21 av. des Bains, CH-1007 Lausanne*

[2]*FOM Institute for Plasma Physics, Rijnhuizen, Nieuwegein, Netherlands.*

1. Introduction

A concern for tokamak reactors is that alpha particles, providing the main source of plasma heating, drive Alfven Eigenmodes (AE) unstable and in turn be subject to anomalous transport induced by these modes [1]. Experimental investigations into the AE linear stability properties and into the features determining their effects on particle orbits appear necessary.

2. The JET AE Active Diagnostic

To obtain this information a new AE active diagnostic has been developed at JET, combining excitation by external antennas with coherent detection of various probing signals, including the impedance of the driven saddle coils, the voltage on non excited saddle coils and magnetic coils, 8 ECE and 8 reflectometer signals [2]. The JET saddle coils are driven by a 3 kW amplifier in the range 30-300 kHz. The antenna currents (<30 A) generate low-n magnetic perturbations much smaller than those predicted to affect the particle transport significantly.

3. TAE and EAE Excitation and Identification

Many global AE have been driven in the frequency range from 50 kHz to 300 kHz and identified as Toroidicity or Ellipticity induced AE from their frequency dependence on density and magnetic field. The eigenmodes appear as resonances in the antenna/detector transfer function. The corresponding poles and residues provide the mode frequency, the total damping rate, $\gamma = \gamma_{damping} - \gamma_{drive}$, and the spatial structure. In Fig. 1 we see an example of a driven AE resonance, with the identification of the observed mode as a TAE being presented in Fig. 2.

4. Direct Measurement of TAE/EAE damping rates

Damping rates were measured in a wide variety of conditions, with $1\ \mathrm{MA} < I_p < 3\ \mathrm{MA}$, $1\times10^{19}\ \mathrm{m}^{-3} < \bar{n}_e < 5\times10^{19}\ \mathrm{m}^{-3}$ and $1\ \mathrm{T} < B_{tor} < 3.5\ \mathrm{T}$ [2]. The results with both odd and even low-n excitation span several orders of magnitude, from $\gamma/\omega < 0.1\%$ to $\gamma/\omega > 10\%$, suggesting that different absorption mechanisms dominate according to the configuration of each specific shot. Greatly differing damping rates were measured in similar discharges with different profiles of $g = 1/(q\rho^{1/2})$, the function determining the AE gap alignment and hence the significance of continuum damping (Fig. 3). With a strong radial dependence of g(r) (a), strong continuum damping occurred with $\gamma/\omega \sim 5\%$. g(r) in curve (b) was flatter and led to a more 'open' gap structure with much less damping.

5. AE spectrum in heated plasmas: kinetic AE

AE experiments have also been undertaken in additionally heated plasmas, to extend the parameter range for the damping measurements, to assess the driving effects of resonant fast particles and to study the AE spectrum in the presence of non-ideal MHD effects. A sudden change was observed in the spectra as T_e, T_i , T_e/T_i and the magnetic shear were increased by means of high current ohmic heating, NBI, Lower Hybrid Heating (LHH), ICRH, or fast plasma current ramps. This transition appeared clearly in high current ohmically heated plasmas (Fig. 4). The single peak TAE observed for low I_p is transformed into a multiple structure of less damped peaks at higher I_p, corresponding to a hotter plasma. As these modes are externally driven with $|n|=2$, with negligible plasma rotation, they cannot correspond to Doppler shifted peaks of different n. Similarly, multiple resonances with the same toroidal mode number characterised the spectrum of driven magnetic and density perturbations in the TAE range with LHH and moderate ICRH (Fig. 5). This first observation of driven density perturbations emphasises the non-ideal MHD character of the modes. Comparable spectra in the TAE/EAE gap frequency range, with similar peak frequency spacing, resonance width and mode numbers, have been driven during discharges with other additional heating methods. In most cases the observed structures consisted of several resonances with regular frequency spacing and damping rates significantly lower than for the corresponding 'cold' TAE. As they appear in experimental conditions which correspond to the predicted departure from ideal MHD behaviour due to kinetic effects, the observed modes are identified as kinetic AE [4].

6. Excitation of AE by non-linear beating of ICRH waves

The excitation of AE by ICRH beat waves was investigated experimentally. The frequencies of two different ICRH modules were mixed together to produce a beat wave signal at Δf, then used as the reference of the AE synchronous detectors. TAE were excited when Δf coincided with the TAE gap centre frequency (Fig. 6). The relatively large amplitudes for the TAE driven by ICRH beat waves suggest that this non-linear excitation method could allow investigations into the effects of AE on particle orbits and should be taken into account in ICRH heated thermonuclear plasmas.

7. Conclusions

The successful implementation of a new active diagnostic for AE has allowed us to drive TAE and EAE in linearly stable conditions and to measure, for the first time, their damping rates in a variety of plasma conditions. Weakly damped, multiple kinetic AE have been excited and detected in the TAE/EAE gap frequency range on the JET heated plasmas. Resonant excitation of TAE by ICRH beat waves has also been demonstrated experimentally. The combination of these linear and non-linear studies should provide insight into the AE stability and their effects on alpha particles' dynamics in future ignition experiments.

The Authors would like to thank the JET Team for experimental support. This work was partly supported by the Fonds National Suisse pour la Recherche Scientifique.

References

[1] C.Z.Cheng, L.Chen, M.S.Chance, *Annals of Physics* **161**, 21 (1985).
[2] A.Fasoli et al., *Phys. Rev. Lett.*, in press (1995).
[3] D.J.Sigmar, C.T.Hsu, R.White and C.Z.Cheng, *Phys. Fluids B* **4**, 1506 (1992).
[4] R.R.Mett and S.M.Mahajan, *Phys. Fluids B* **4**, 2885 (1992).

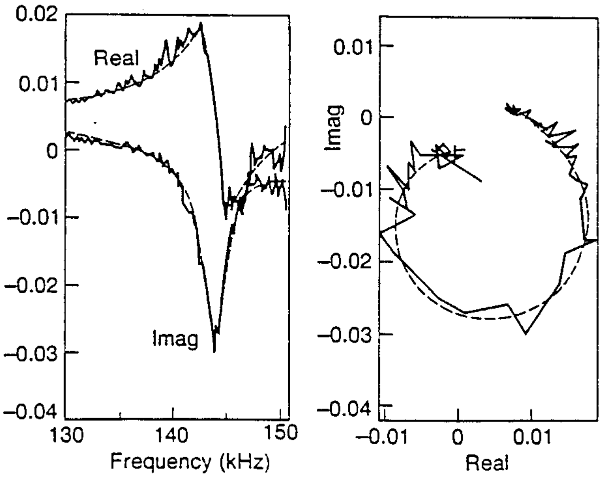

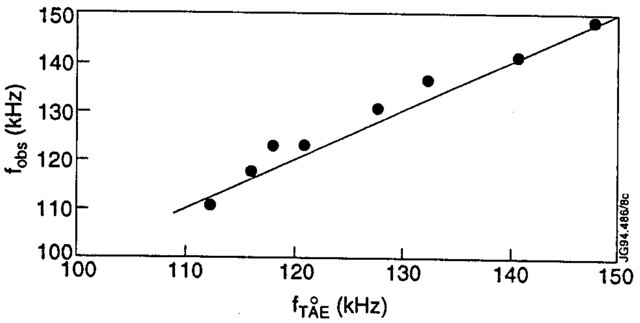

Fig. 2 Measured eigenfrequency vs $f_{TAE}{}^0=v_A/2\pi qR$, the TAE gap centre, calculated for q=1.5 (#31591). B_{tor} was varied linearly between 2.2 and 3 T.

Fig. 1 TAE resonance in ohmic plasma (#31638). Real and imaginary parts (left) and complex plane representation (right) of a magnetic probe signal, normalised to the driving current. A fit with a transfer function of order 5/2 is shown, giving f_{obs}=144.2 +-0.1 kHz, $\gamma/2\pi$=1400 +-100 s^{-1}, $\gamma/\omega \cong 1\%$.

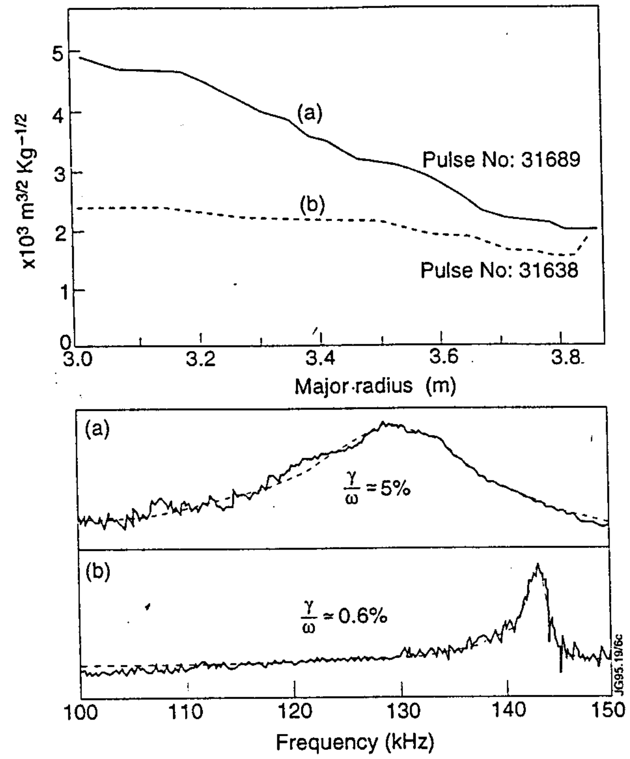

Fig. 3 The relationship between the profile of $g(r)=1/(q(r)\rho(r)^{1/2})$ and the TAE damping. Excitation peaked at $|n|=2$ was used for both discharges; ohmic plasma, with $\bar{n}_e \cong 4x10^{19}$ m^{-3}; (a) $B_{tor} \cong 1.8$ T. (b) $B_{tor} \cong 2.8$ T.

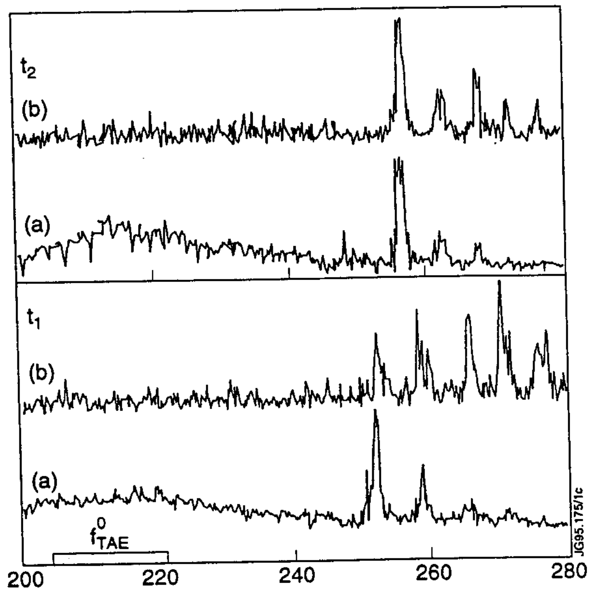

Fig. 5 Spectrum of magnetic (a) and density perturbations at r/a~0.5 (b), with LHH (2.5 MW) and ICRH (6 MW). Two successive scans in shot #33157, at t_1 = 19 s and t_2 = 20 s, are shown. I_p ~ 3 MA; B_{tor} ~ 3.2 T; T_e ~ 6.3 keV; T_i ~ 2.9 keV.

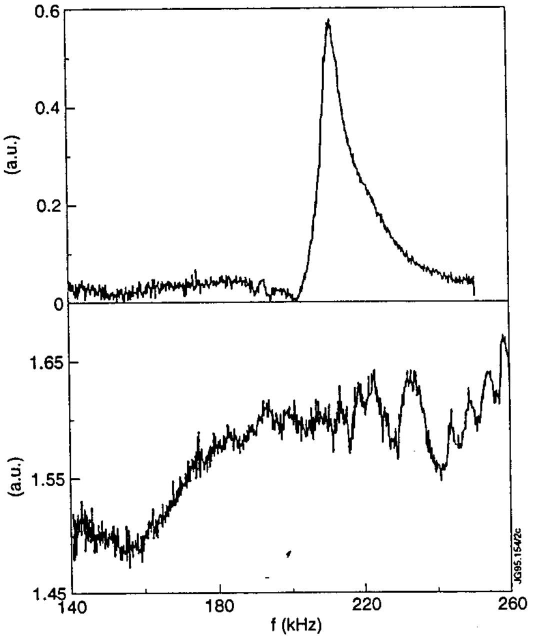

Fig. 4 δB_{pol} probe signals for moderate (top: t=3.5 s; I_p ~2 MA; B_{tor}~2.5 T; T_e ~2.2 keV; $f_{TAE}{}^0$~200 kHz) and high plasma current (bottom: t=9.5 s; I_p ~ 4.1 MA; B_{tor}~2.9 T; T_e~3.2 keV; $f_{TAE}{}^0$~180 kHz) in shot #34073.

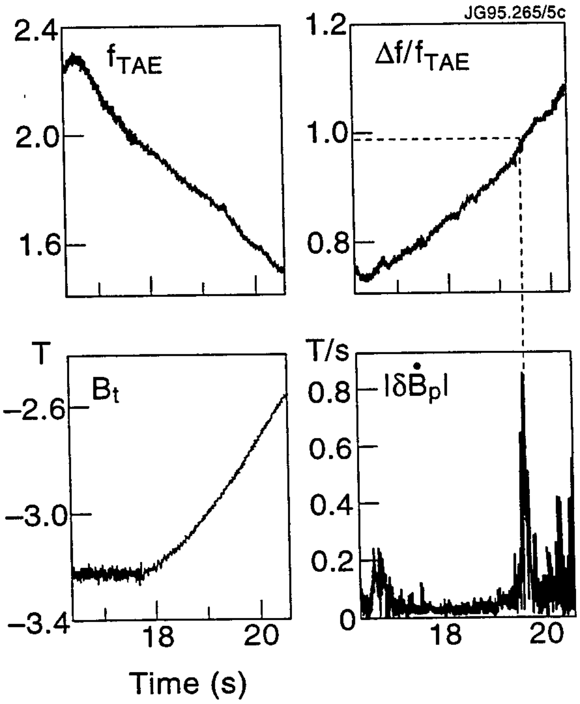

Fig. 6 Observation of TAE driven by ICRH beat waves in shot #35051. Each module is in dipole configuration for hydrogen minority heating, with $f_{1,2}$ ~ 43 MHz, and coupled power ~1MW; I_p ~ 3 MA; T_e ~ 5 keV.

Consistency and Precision of the TCV Magnetic Measurements

J.-M. Moret, F. Bühlmann, F. Hofmann, G. Tonetti

Centre de Recherches en Physique des Plasma
Association EURATOM - Confédération Suisse
Avenue des Bains 21, CH-1007 Lausanne, Switzerland

Introduction. The TCV tokamak has been built to study the influence of the plasma shape on tokamak physics. Possible shapes include limited and open single null or double null divertor configurations with an elongation up to 3, and more complex configurations. The magnetic measurements must permit a flexible control of the plasma contour and the divertor legs in all these situations. These measurements are used for both real time control and off line reconstruction of the magnetic topology which require high accuracy and high redundancy. In the work presented here the redundancy was used in conjunction with dedicated measurements to check the consistency of the measurements, quantify their accuracy and then determine corrections in the sensor location and in the measurement calibration. These corrections have permitted considerable improvements in the consistency and precision.

TCV magnetic diagnostics. A poloidal cross section of TCV is shown in figure 1. The ohmic transformer consisting of coil A and coils B, C and D in series are connected to two separate power supplies, OH1 and OH2. Each shaping coil E1 to E8 and F1 to F8 has its own power supply to provide maximum flexibility in shape control. The coils labelled T1 to T3 are the connections between the toroidal field coils. The current in all these coils are measured by LEM modules to an accuracy of 0.5%. The poloidal flux is measured at 61 positions by flux loops wound on the outside of the vessel and on the shaping and ohmic transformer coils (× in the figure). The complete signal conditioning and acquisition electronics was calibrated to better than 0.5%. 4 poloidal sections are equipped with 38 magnetics field probes, shown by to scale rectangles in the figure. The effective area of each probe was separately measured and the combined error of this area and the corresponding electronics is better than 1%. Any of these signals may be used for real time shape control and, following acquisition, for equilibrium reconstruction.

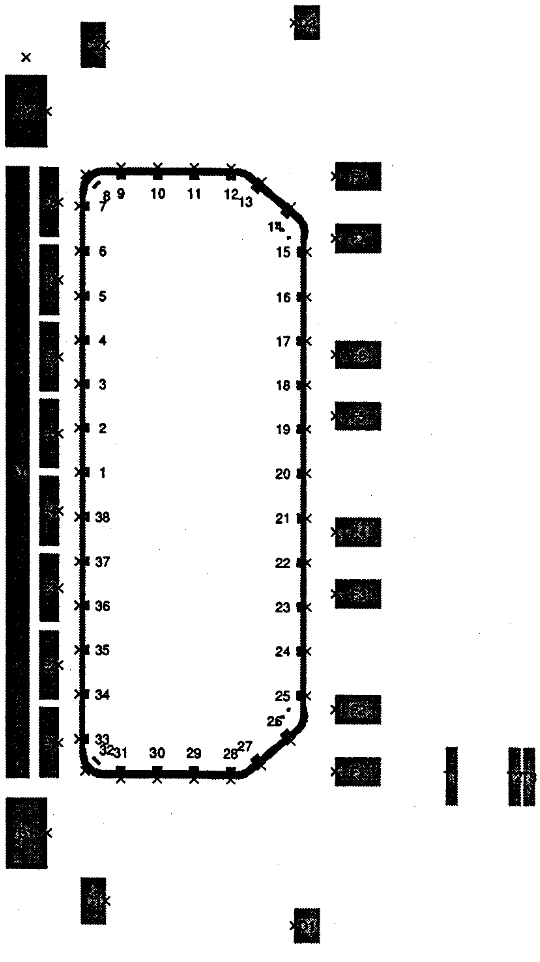

Fig. 1 TCV layout.

Consistency check. The degree of consistency in these measurements was investigated with experiments in which each coil was in turn fed by a constant current (±10 A during 1 s) to avoid eddy current in the vessel. This provides 19 independent measurements for each magnetic signal. The modelled values for the poloidal flux and magnetic field can be computed based on the constructional dimensions and on the coil currents, respectively $M_{fa}(R_f,Z_f,R_c,Z_c)I_a$ and $B_{ma}(R_m,Z_m,a_m,R_c,Z_c)I_a$ where M_{fa} is the mutual inductance between the flux loop located at (R_f,Z_f) and the coil at (R_c,Z_c), B_{ma} the magnetic field per unit current measured by the probe at (R_m,Z_m) with orientation a_m and I_a the coil current. In this computation, the coils were split into individual turns (1 to 3 cm in size) and the magnetic probe spatial extension were taken into account. Comparison of the modelled values with the measured flux and field y_f and B_m indicates discrepancies of the order of 2% and 5% respectively (fig. 2), which clearly exceed the expected, and tolerable, errors.

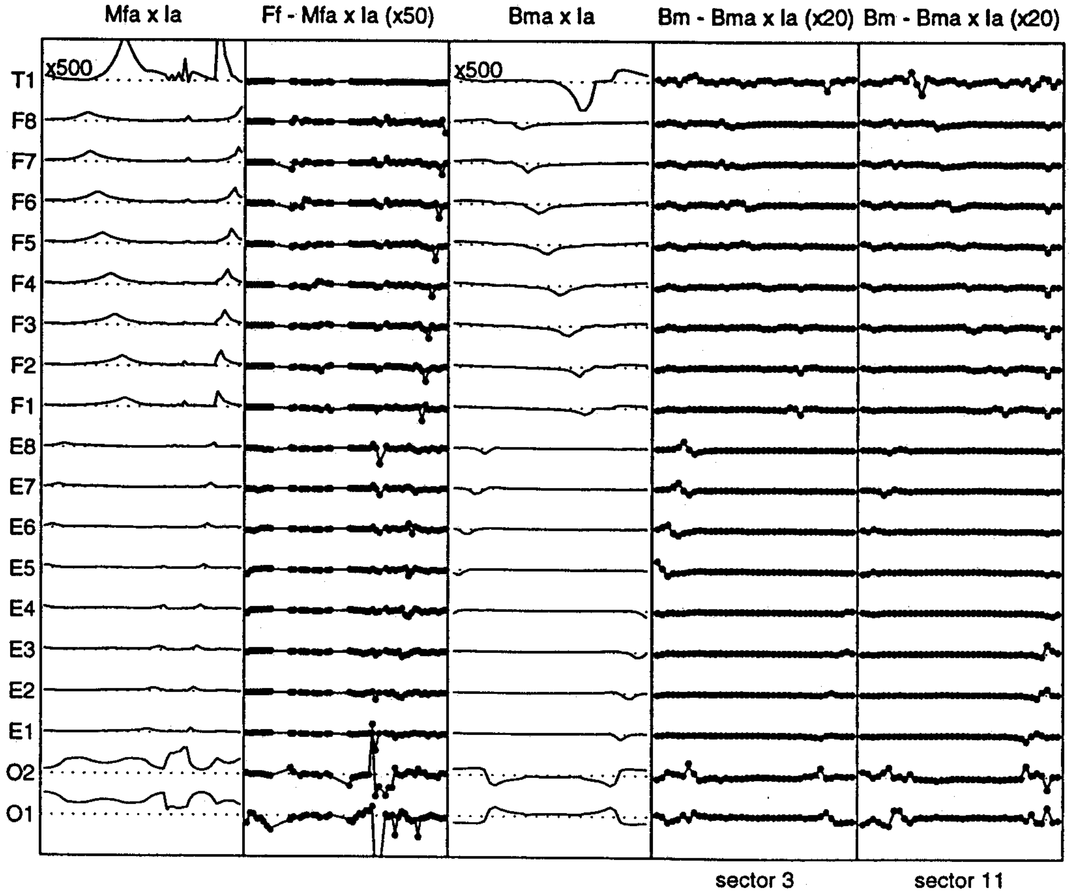

Fig. 2 Modelled flux and field $M_{fa}I_a$ *and* $B_{ma}I_a$*; flux and field errors* $\psi_f - M_{fa}I_a$ *and* $B_m - B_{ma}I_a$ *(dots: measured, solid line: effect of the corrections). Curves are drawn as a function of the sensor number for each coil current.*

Sources of errors. The explanation for these differences is to be mainly found in small calibration and positional errors. Relative calibration error in a coil current ΔG_a yields a flux and field error of $\Delta G_a M_{fa} I_a$ and $\Delta G_a B_{ma} I_a$ while a calibration error in the flux ΔG_f and field ΔG_m produces errors of $\Delta G_f M_{fa} I_a$ and $\Delta G_m B_{ma} I_a$. The differences produced by misplacement of coils or sensors take, for example in the case of a flux loop radial displacement ΔR_f, the form $\Delta R_f \partial_{R_f} M_{fa}(R_f,Z_f,R_c,Z_c)I_a$.

Determination of the corrections. All these corrections can be adjusted to reproduce the observed differences. This may be achieved by minimising the residual errors in the flux and field

$$\Delta\psi_f = \psi_f - M_{fa}I_a - (\Delta G_a M_{fa}I_a + \Delta G_f M_{fa}I_a + \Delta R_f \partial_{R_f} M_{fa}I_a + \ldots) \qquad (1)$$
$$\Delta B_m = B_m - B_{ma}I_a - (\Delta G_a B_{ma}I_a + \Delta G_m B_{ma}I_a + \Delta R_m \partial_{R_m} B_{ma}I_a + \ldots) \qquad (2)$$

by means of the cost function

$$J = \sum_{f,k} w_f^2 \, \Delta\psi_{fk}^2 + \sum_{m,k} w_m^2 \, \Delta B_{mk}^2 \qquad (3)$$

where w_f and w_m are appropriate weights and the index k runs over the experiments. The deduced corrections remain small, a few % in the calibrations and a few mm in the positions. They exceeded, however, the expected tolerances and this can be understood by inspecting the covariance matrix (fig. 3). This shows strong correlations, one of the most obvious being that a correction in a current calibration is compensated by an opposite correction in the flux and field measurements.

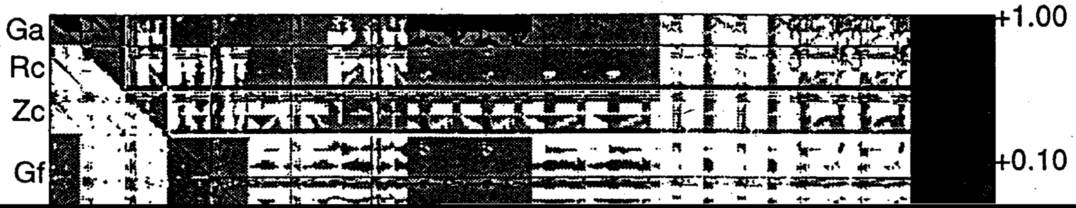

[redacted]

This effect can be diminished by choosing a cost function that favours small corrections:

$$J' = J + \sum_a w_{Ga}^2 \, \Delta G_a^2 + \ldots + \sum_f w_{Rf}^2 \, \Delta R_f^2 + \ldots \tag{4}$$

Here, the weights were chosen to be the inverse of the expected errors in the corrected parameters. All the corrections deduced with this cost function are now limited to a tolerable amplitude (fig. 4), with only a slight increase in the flux and field residuals (0.5→0.8 mWb and 0.3→0.4 mT). The reduction in the correction correlations is significative (fig. 3).

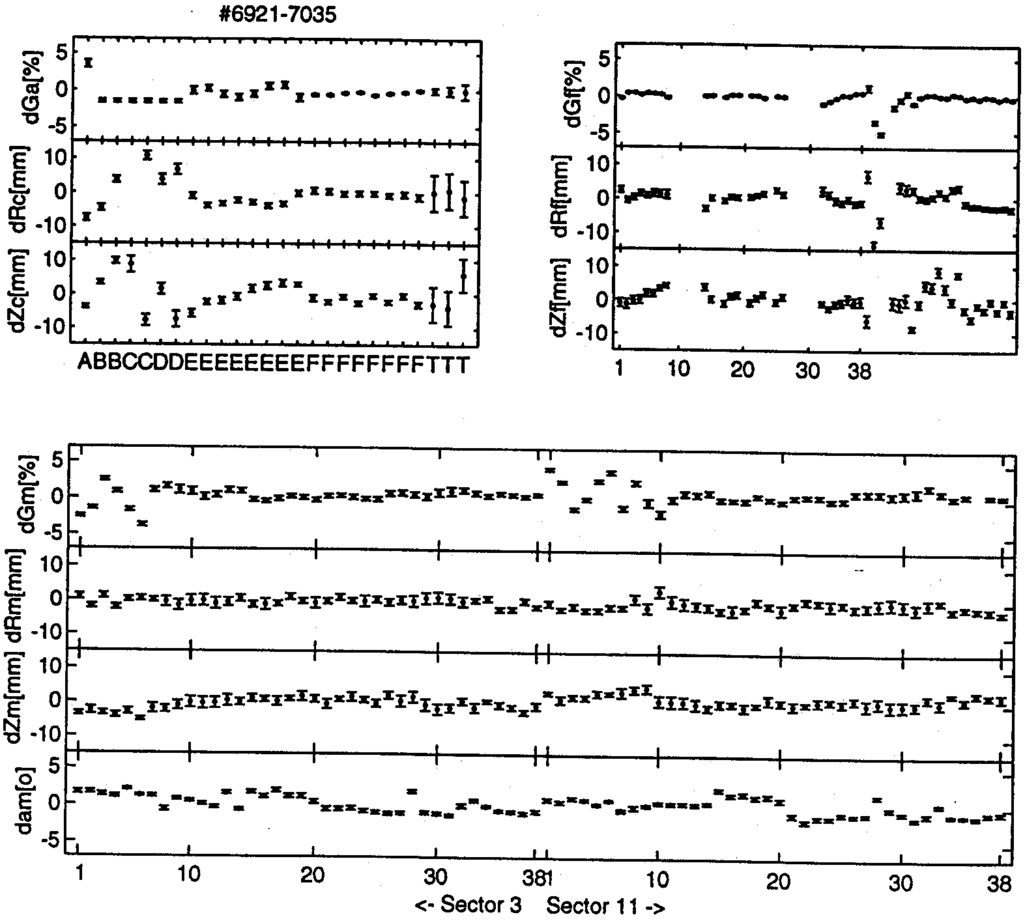

Fig. 4 Derived corrections.

The linearity of the measurements was verified by repeating the experiments at half current. Only the coil current measurements show a small non linearity which may be due to the ferromagnetic elements in the LEM modules.

Conclusion. Although a first analysis indicates errors higher than expected, it has been possible to reduce the errors to a very low value (0.5 mWb and 0.5 mT). To achieve this, small corrections in the system calibrations and in the coil, flux loop and magnetic probe positions have been derived by a formalised method together with appropriate experiments. The TCV magnetic diagnostic thus provides a measurement set which is highly coherent and in which each measurement exploits the calibration precision.

This work was partly supported by the Fonds National Suisse de la Recherche Scientifique.

Influence of Plasma Near Separatrix on Ideal MHD Stability in Tokamaks

L.Degtyarev, A.Martynov, S.Medvedev
Keldysh Institute of Applied Mathematics, Russian Academy of Sciences, Moscow
F.Troyon, L.Villard
Centre de Recherches en Physique des Plasmas, Association Euratom – Confédération Suisse, Ecole Polytechnique Fédérale de Lausanne

Abstract

Stability studies of doublet [1, 2] and single null configurations [3] with the KINX MHD stability code have revealed the influence of the presence of plasma near the separatrix on ideal MHD modes.

Growth rates of $n = 0$ modes can be reduced even by the presence of a currentless mantle plasma. Perturbations of surface current along the equilibrium magnetic field at the plasma-vacuum interface account for this kind of stabilization.

The stabilization of external kink modes when the plasma near the separatrix is taken into account is connected with the larger number of rational surfaces inside the plasma at fixed plasma current and internal inductance l_i.

The paper presents further investigations of the boundary plasma effect on the stability with emphasis on single null divertor configurations.

1. Mantle effect on $n = 0$ mode

The perturbed potential energy representation is the same for the cases of currentless mantle plasma or vacuum at the place of the mantle:

$$\delta W = \frac{1}{2} \int_{mantle} |\delta B|^2 \, dV, \tag{1}$$

where δB is magnetic field perturbation. The perturbed magnetic pressure continuity at the plasma-vacuum interface

$$B \cdot \delta B = B \cdot \delta B_v \tag{2}$$

prohibits surface current perturbations across the equilibrium magnetic field lines. However, perturbations of the surface current along the equilibrium field can arise and account for a difference in the value of the potential energy compared to the vacuum case.

The following model problem was chosen to demonstrate the stabilizing effect of the mantle. The plasma toroidal current density profile with the currentless mantle was prescribed as follows

$$r j_\phi = \begin{cases} 1 - \bar{\psi}/\psi_m, & 0 < \bar{\psi} < \psi_m, \\ 0, & \psi_m < \bar{\psi} < 1, \end{cases} \tag{3}$$

where $\bar{\psi}$ is the normalized poloidal flux and ψ_m controls the width of the mantle. The plasma density profile was the same as $r j_\phi$ in order to exclude the inertia from the mantle. It makes possible to compare ideal MHD growth rates with the vacuum case. The growth rates should be the same if there is no surface current. A difference in the growth rates implies the existence of a perturbed surface current.

An equilibrium with an inverse aspect ratio $a/R = 0.2725$, $\psi_m = 0.9$ and a safety factor on magnetic axis $q_0 = 1.05$ was chosen. An ideally conducting wall of elliptic cross section and minor radius twice of the plasma minor radius ($b/a = 2$) was placed around the plasma. For the up-down asymmetric plasma boundary with overall elongation 1.5 (see Fig.1) the obtained difference in the ideal MHD growth rates between the cases with and without mantle was about 10%.

However, for the elliptic cross-section plasma no difference in the converged growth rates was revealed. It corresponds to the vanishing surface current due to the antisymmetric normal component of the "vertical" displacement eigenfunction in the case of an up-down symmetric equilibrium.

The difference in growth rates for asymmetric cross sections also occurs for resistive wall modes.

2. Plasma outside separatrix

The effect of the presence of plasma outside the separatrix on $n = 0$ stability was studied in computations for doublet configurations [2]. Resistive wall mode growth rates were considerably reduced by the presence of a mantle plasma outside separatrix in the case of up-down asymmetric configurations. However, the stabilization due to the surface current excitation at the plasma-vacuum interface is also possible in up-down symmetric doublet configurations. This is due to the structure of the most unstable $n = 0$ mode in doublets featuring a symmetric normal displacement component [1, 2] in contrast to the antisymmetric one in the case of single axis elongated up-down symmetric plasmas.

The effect of plasma outside separatrix in a single null divertor configuration was the next subject of investigation.

As long as the equilibrium magnetic field is the same in vacuum and in mantle plasma, the equilibrium configuration with a mantle plasma outside separatrix can be easily produced from any free boundary single axis equilibrium. For the model problem it is convenient to turn the doublet equilibrium into the divertor configuration (see Fig.2). The toroidal current density was prescribed by (3) with $\psi_m = 1$ inside the separatrix and with a currentless mantle outside the separatrix.

Vanishing displacement at the boundaries where the equilibrium magnetic field $B \cdot n \neq 0$ (Fig.2a) corresponds to the case of perfectly conducting end plates touching the plasma.

The stability code KINX-W [2] has been modified to treat such configurations. The first version of the code computes $n = 0$ stability in the presence of a wall with finite resistivity. Perfect conductors can be optionally placed also at some parts of the external mantle boundary (Fig.2b, Fig.2c).

The table below compares the growth rates for the single axis plasma inside the separatrix, the doublet plasma without and with the mantle (two modes) and the divertor configuration with end plates. All are placed inside the resistive TCV wall. The eigenfunction arrow plot for the case of the divertor configuration is given in Fig.3. The strong stabilizing effect comes not from the conducting end plates alone but from the presence of the plasma outside the separatrix in the divertor configuration.

single axis	doublet without mantle	doublet	divertor
410	680/110	220/110	85

Table 1: Growth rates in s^{-1} for the TCV wall.

The presence of perfect conductors in the vacuum near the plasma can stabilize the $n = 0$ mode. However, the presence of lateral plates touching the plasma outside the separatrix has again a much stronger stabilizing effect. The lateral plates placed like in Fig.2b completely stabilize the $n = 0$ mode. On the other hand putting the bottom conducting plate (Fig.2c) has almost no stabilizing effect on growth rates.

To estimate the stabilizing effect of perfect conductors for the single axis plasma in the absence of mantle, we prescribe a wall shape similar to that of the separatrix and consider a fraction of its circumference below the x-point as an ideal conductor. For $b/a = 1.3$ the ideal wall fraction needed to stabilize the mode is 30%. For a closer fitting wall with $b/a = 1.1$ the fraction needed for stabilization is 15%. For both cases the ideally conducting parts of the wall are much closer to the plasma than for the case of the lateral plates touching the mantle.

The stabilizing effect of the plasma outside separatrix on $n = 0$ mode is very strong in the divertor configuration. The stabilization comes both from the mantle effect and the specific boundary conditions.

3. Kink modes

In the frame of ideal MHD the difference between mantle plasma and vacuum is more significant for $n > 0$ modes. The existence of rational surfaces introduces singularities in the MHD equations thus restricting the admissible set of magnetic field perturbations. If the separatrix is closer to the plasma boundary then the shear is higher and the number of rational surfaces inside plasma is bigger.

The calculations of β limits for L-mode and H-mode ITER configurations [3] showed that external kink modes are less sensitive to the plasma profiles near separatrix than to the proximity of the separatrix to the plasma boundary. For all cases the beta limits are higher with separatrix at the boundary. From $\beta = 5.8\%$ for a plasma boundary defined by $\psi_{boundary}/\psi_{separatrix} = 0.95$ they raise to $\beta = 6.3\%$ for the separatrix at the boundary for $n = 1$ external kink mode and L-mode equilibrium. The difference is higher for H-mode case: 5.0% vs. 6.8%.

On the other hand the stability calculations for doublet configurations [2] showed that β and current limits against external $n = 1$ kink stability for doublets and for single-null plasma inside separatrix are very close to each other. No substantial influence of the plasma outside the separatrix on the external kink limits was discovered. The reason for that could be very the high values of q in the low current plasma outside the separatrix. Corresponding high order rational surfaces have a weak effect on external kink stability [3].

Kink stability of divertor configurations with plasma outside the separatrix involving various types of boundary conditions is an important subject of further investigation.

4. Discussion

The presented results point to the substantial influence of the presence plasma near the separatrix on ideal MHD stability.

- The mantle plasma inside and outside the separatrix can considerably reduce $n = 0$ growth rates especially in divertor plasma configurations.
- The kink mode stability is favored by the presence of the separatrix inside the plasma.

However the ideal MHD model may be not adequate to describe the tokamak plasma behavior especially in the vicinity of the x-point and outside the separatrix. More realistic models are also needed to compute the divertor configuration stability.

Acknowledgement

This work was partly supported by the Fonds National Suisse de la Recherche Scientifique.

References

[1] Medvedev S., Villard L., Degtyarev L.M., Martynov A., Gruber R., Troyon F. MHD equilibrium and stability of doublet configurations. 20th EPS Conf. on Controlled Fusion and Plasma Phys., Lisbon, Proc. Contrib. Papers vol.IV (1993) 1279

[2] Degtyarev L.M., Martynov A., Medvedev S., Troyon F., Villard L. MHD limits and axisymmetric stability of doublets. 21th EPS Conf. on Controlled Fusion and Plasma Phys., Montpellier, Proc. Contrib. Papers vol.II (1994) 556

[3] Boucher D. *et al.* ITER plasma modeling and MHD stability limits, 15th Int. Conf. on Plasma Phys. and Controlled Nuclear Fusion Research, Sevilla, Spain, September–October (1994), paper IAEA-CN-60/E-P-2

[redacted]

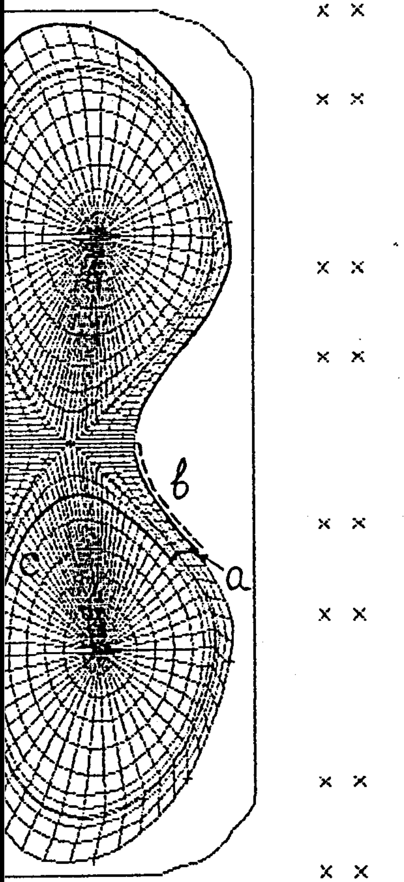

ilibrium grid adapted to mag-
es for the up-down symmetric
figuration. The divertor config-
ndaries are given by bold lines.
onducting plates, (b) lateral
bottom plate.
vall and PF coils are shown.

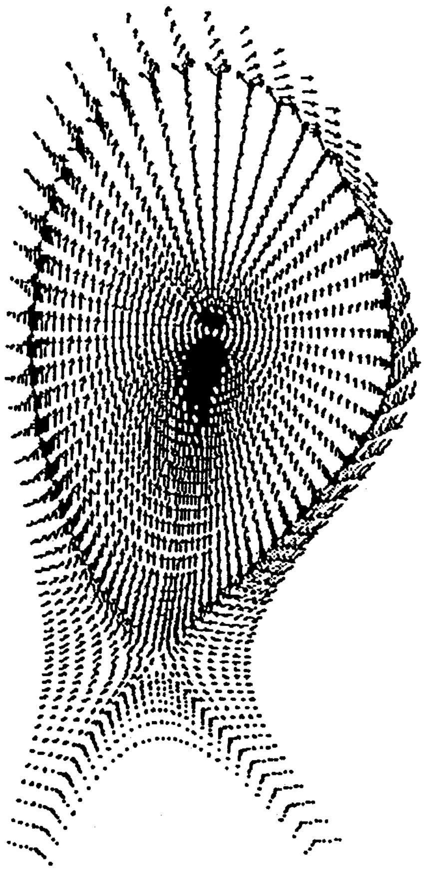

Fig.3: Eigenfunction of the resistive wall $n = 0$ mode for the divertor configuration.

Global Internal Modes in the H1 Heliac

W. A. Cooper
CRPP/EPFL, Association Euratom/Confederation Suisse,
Lausanne, Switzerland
and
H. J. Gardner
Plasma Research Laboratory and Department of Theoretical Physics,
Research School of Physical Sciences and Engineering,
The Australian National University,
Canberra, Australia

Heliac devices are three dimensional (3D) stellarator configurations with relatively large rotational transform per field period and relatively weak magnetic shear. They

[redacted]

The 3D TERPSICHORE code [5] is used to investigate the global internal modes of the sequence of equilibria calculated with VMEC. An initial test of stability was carried out with a set of Fourier modes to describe the instability structure limited to the $m = 7, n = 8$ component and its three closest poloidal sidebands. The configurations with a boundary description less than 40% of the H1 have nonmonotonic ι profiles (see Fig. 1a) and in particular have the $\iota = 8/7$ rational surface near the centre of the plasma and near the edge. This initial test demonstrated a dominant core localised $m = 7, n = 8$ mode that became marginal as the $\iota = 8/7$ surface near the centre vanished into the magnetic axis as the plasma shaping was increased to a 3/8 fraction of the standard H1. The family of Fourier components that have toroidal mode numbers that are a multiple of 3 (the number of field periods) constitute the modes of the equilibrium. Those that are not a multiple of 3 constitute a single family that describe the structure of an instability [6,7]. It has been our experience, however, that an arbitrary selection of toroidal sidebands in helical axis stellarators yields very ill conditioned matrices. The selection of toroidal sidebands of the main instability structure, therefore, requires a careful evaluation of the dominating Fourier components of the equilibrium state. The most relevant components of the equilibrium for the sequence we have investigated are:

M	NL
$0-4$	0
1,2	-3
$0-5$	3
1,2	-6
$0-3$	6
$0-3$	9
$2-5$	12

where NL denotes the product of N times L. We have found that the $m = 5, n = 5$ component becomes more important than the $m = 7, n = 8$ component as the plasma shaping increases because as shown in Fig. 1a the value of ι on axis decreases to almost unity for the configurations that are 70% – 75% of the H1 before starting to increase again. Considering the $m = 5, n = 5$ as the dominant component of the instability, we obtain that it couples with 48 additional sidebands of significance through beatings with the equilibrium components we have identified (eg.,$m - 5 = M, n - 5 = NL; m + 5 = M, n + 5 = NL$) [6,7]. The eigenvalues as a function of the square of the inverse of the number of radial intervals (which were varied from 48 to 108) for the configurations with $f = 0.5$, $f = 0.6$, $f = 0.7$ and $f = 0.75$ are shown in Fig. 1b. In Fig. 2a, the converged eigenvalues extrapolated to infinitesimal mesh in Fig. 1b are plotted with respect to the shaping parameter f which reveals that the configuration that is 78% the H1 heliac and 22% the helical axis stellarator becomes marginal to the $m = 5, n = 5$ mode. This stabilisation is mostly due to the deepening of the magnetic well with f, but also the increase of ι on axis for $f > 0.7$ that displaces the $\iota = 1$ resonant surface further away plays a rôle. The five dominant Fourier components of the radial component of the perturbed displacement vector as a function of the radial variable s are shown in Fig. 2b for the configuration with $f = 0.75$ and the corresponding profile of the potential energy perturbation is shown in Fig. 3a.

The $M = 8, N = 3$ component of the equilibrium state constitutes another potentially important contribution to the stability picture because it corresponds to a resonance condition within the plasma where the parallel current density can diverge. We have thus included two additional sidebands, the $m = 3, n = 4$ and the $m = 13, n = 14$ components, which couple with the main $m = 5, n = 5$ component to beat with the equilibrium $M = 8, NL = 9$ term. We obtain eigenvalues that are more unstable, but a convergence study in the radial mesh size shows that the perturbed potential energy becomes a δ function about the $\iota = 9/8$ resonant surface as shown in Fig. 3b. The mode structures that are excited all localise about the 9/8 rational surface and the magnitude of the eigenvalues depend sensitively on how close the mesh point is located with respect to the 9/8 surface as we change the number of radial intervals. Therefore, this type of instability appears to be a manifestation of a shortcoming of the equilibrium description. The extreme localisation of the perturbed energy suggests that the model may be inadequate. Magnetic islands and finite Larmor radius effects should resolve the narrow unstable layer.

In conclusion, we have analysed a sequence of equilibria that lead to the standard H1 configuration with respect to global ideal MHD internal modes. This study suggests that the H1 should be stable to global structures well beyond the β limits imposed by local Mercier and ballooning modes.

References

[1] Hamberger S M et al, *Fusion Technol.* 17 123 (1990)
[2] Hirshman S P and Betancourt O, *J. Comput. Phys.* 96 99 (1991)
[3] Gardner H J and Blackwell B D, *Nucl. Fusion* 32 2009 (1992)
[4] Cooper W A and Gardner H J, *Nucl. Fusion* 34 729 (1994)
[5] Anderson D V et al, *Int. J. Supercomp. Appl.* 4 34 (1990)
[6] Cooper W A et al, *Proc. Joint Varenna – Lausanne Int. Workshop on Theory of Fusion Plasmas* (Editrice Compositori, Bologna 1990) p.655
[7] Schwab C, *Phys. Fluids* 5 3195 (1993)

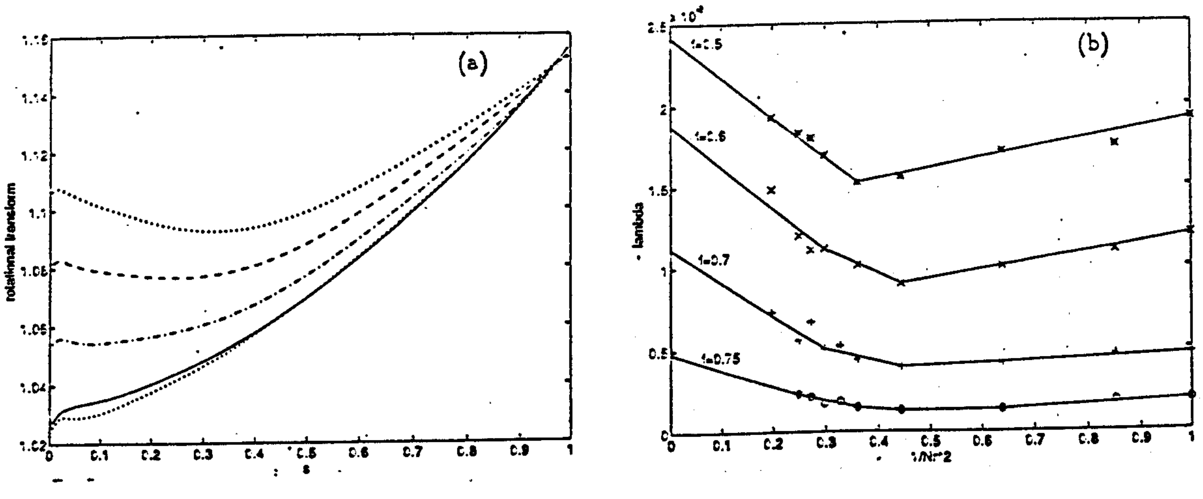

Figure 1: (a) The rotational transform ι profiles for the configurations with $f = 0.4$ (top dotted curve), $f = 0.5$ (dashed curve), $f = 0.6$ (dot-dashed curve), $f = 0.7$ (lower dotted curve) and $f = 0.75$ (solid curve); (b) Radial convergence of eigenvalues for configurations ranging from 50% to 75% of the standard H1

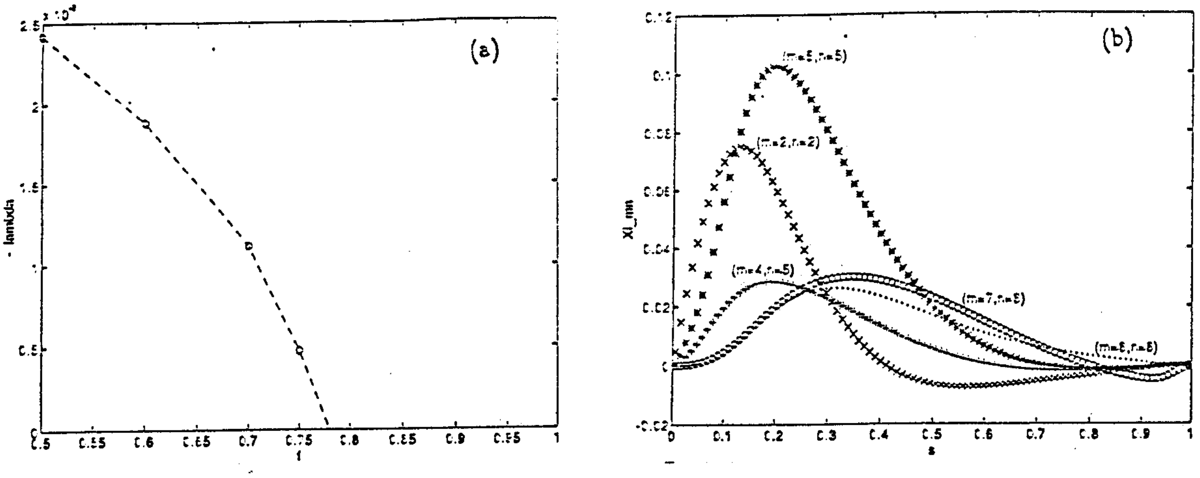

Figure 2: (a) The converged eigenvalue dominated by the $m = 5, n = 5$ component with 49 mode pairs as a function of the heliac shaping parameter f; (b) The Fourier mode structure of the radial component of the perturbed displacement vector with 49 mode pairs for the configuration with $f = 0.75$

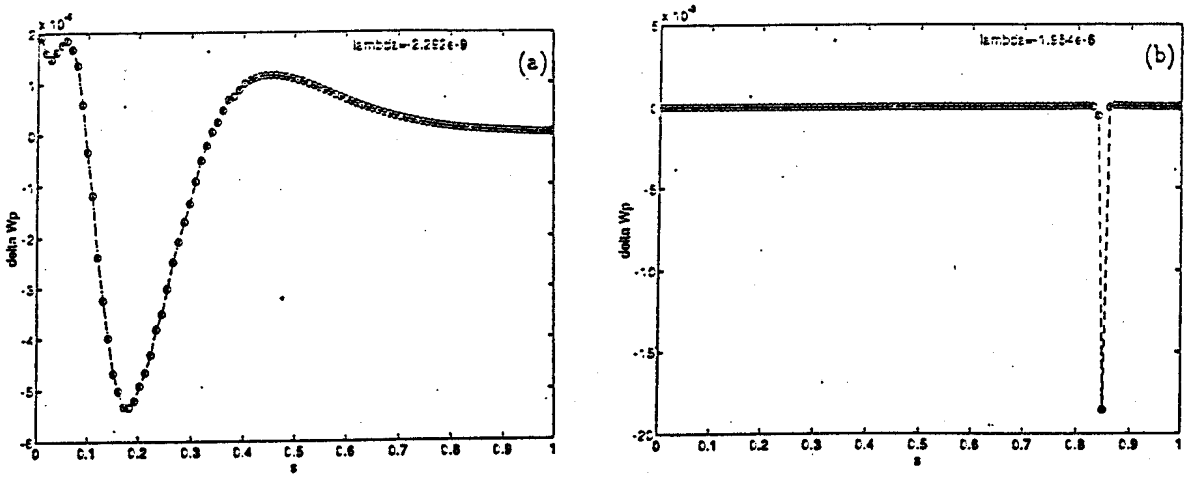

Figure 3: The perturbed potential energy profile for the configuration corresponding to $f = 0.75$ with (a) 49 mode pairs which is dominated by the $m = 5, n = 5$ component and with (b) 51 mode pairs which is dominated by the $m = 13, n = 14$ component

Drift Reversal in the WVII-X Advanced Stellarator

D. Clément and W. A. Cooper
CRPP/EPFL, Association Euratom/Confederation Suisse,
Lausanne, Switzerland

1. Introduction

The variation of the magnetic field along a field line in fusion plasma confinement configurations causes particles to become mirror-trapped. These particles can trigger instabilities in the fluid plasma which can have important implications especially if they are energetic. The sign of the ratio of the bounce-averaged magnetic drift frequency to the diamagnetic drift frequency constitutes a useful and important measure of the impact of trapped particles on instabilities. The application of a Schwarz inequality shows that for magnetohydrodynamic (MHD) modes, energetic trapped particles exercise a stabilising effect if the ratio is positive, but no conclusions can be drawn if it is negative [1]. In the Wendelstein WVII-X device [2], the effect of trapped particles on ballooning instabilities has been examined by Nührenberg and Zheng [3]. Another important class of instability is the *collisionless trapped particle mode* ($CTPM$) [4], which can enhance anomalous transport losses. These modes that are localised in regions of unfavourable curvature can be stabilised by the digging of a magnetic well at finite β that reverses the direction of the magnetic drifts. In this work, we examine the conditions that lead to the reversal of the magnetic drift frequencies in the WVII-X Advanced Stellarator.

2. The equations

We invoke the ballooning representation in order to calculate the ratio ot the magnetic to diamagnetic drift frequencies because local stability properties are evaluated in ballooning space in order to reconcile conditions of periodicity in toroidal systems with finite magnetic shear [5]. In the ballooning space, the magnetic drift frequency is given by the expression

$$\omega_{dj} = -\frac{1}{\Omega_j}\left[\left(\frac{B\times k_\perp\cdot\kappa}{B}\right)v_\parallel^2 + \left(\frac{B\times k_\perp\cdot\nabla lnB}{B}\right)\frac{v_\perp^2}{2}\right], \tag{1}$$

where $\Omega_j = Z_j eB/M_j$ is the cyclotron frequency of a particle of species j, $\kappa = (b\cdot\nabla)b$ is the magnetic field line curvature and b is the unit vector along the magnetic field lines. The diamagnetic drift frequency is

$$\omega_{*j} = -\frac{p_j}{\Omega_j\rho_{Mj}}\frac{B\times k_\perp\cdot\nabla lnN_j}{B}, \tag{2}$$

where p_j is the pressure, N_j is the density, Z_je is the electronic charge, $\rho_{Mj} = M_jN_j$ is the mass density and M_j is the mass of the particles of species j. We express the ratio of the diamagnetic drift frequency to the bounce-averaged magnetic drift frequency as

$$\frac{1}{R} = \frac{(-1)\int_{\theta_{min}}^{\theta_{max}} d\theta\sqrt{g}\frac{B}{v_\parallel}}{\int_{\theta_{min}}^{\theta_{max}} d\theta\frac{\sqrt{g}}{v_\parallel}\left[\left(\frac{B\times\nabla S\cdot\nabla(p+B^2/2)}{B^3}\right)v_\parallel^2 + \left(\frac{B\times\nabla S\cdot\nabla B}{B^2}\right)\frac{v_\perp^2}{2}\right]}, \tag{3}$$

which is evaluated in the Boozer magnetic coordinate system [6] (s,θ,ϕ), where s labels that radial variable, θ is the poloidal angle and ϕ is the toroidal angle. In this coordinate system, the magnetic field B lines are straight, hence the wave vector $k_\perp = \nabla S$ in ballooning space is given by $\nabla S = \nabla\phi - q\nabla\theta - q'(\theta-\theta_k)\nabla s$, where q is the inverse of the rotational transform and prime ($'$) denotes the derivative with respect to s. The integration with respect to θ between the bounce points θ_{min} and θ_{max} are evaluated on a fixed magnetic field line $\alpha = \phi - q\theta$ which reflects the coordinates being straight. The factor (-1) in the numerator is a result of the normalisation of the diamagnetic drift frequency that we have imposed to unity taking into consideration that the density profile is assumed monotonically from the centre to the edge of the plasma to make its sign negative.

3. Description of the results

We calculate three dimensional (3D) equilibria with nested magnetic flux surfaces that model the WVII-X device with the VMEC code [7]. We map these equilibria to the Boozer magnetic coordinates with the modules of the TERPSICHORE stability code that perform this task [8]. To evaluate the bounce averages, we chooses $\theta = \theta_{max}$ and evaluate the pitch $\lambda = 1/B(\theta_{max})$ and then follow the field line to search for θ_{min} that satisfies $B(\theta_{min}) = B(\theta_{max})$ to a prescribed absolute error, typically 10^{-11}. We then apply a Simpson rule to performe the bounce average integrations. We have benchmarked the calculations with results presented for the tight aspect ratio START tokamak [9]. We find good agreement with respect to the drift reversal of the barely trapped particles and with the observation that the fraction of drift-reversed particles does not change with β. Some discrepancies are observed in the shape of the $1/R$ curve for deeply trapped particles that can be attributed to the difference in the models employed. The mod-B distribution in WVII-X on a surface with $s = 10/18$ is illustrated in Fig. 1. As an initial application for WVII-X, we have considered the evaluation of $1/R$ on two different field lines $\alpha = -1$ and $\alpha = -1 - 2\pi/5$, which due to stellarator symmetry describe in fact the same field line (Fig. 1). The results are essentially identical. The calculation of $1/R$ shows that the grad-B drifts dominate over the curvature drifts because the trapped particle orbits are confined to the straight sections of the WVII-X device. It also shows that the magnetic well is an important factor associated with drift reversal. At low β, only the barely trapped particles have orbits of sufficient toroidal extent to sample the well to reverse their drifts. The bulk of the trapped particles do not drift-reverse except for a small fraction of deeply trapped particles near the magnetic axis. This is shown in Figs. 2a-2c. As we raise β, we find that the fraction of drift-reversed particles increases significantly at $\beta = 1.5\%$ and that virtually all trapped particles reverse their magnetic drifts near the MHD limit of $\beta = 5\%$. The drift reversal is caused by the enhancement in the magnitude of the radial gradient of the Jacobian $\sqrt{g}$ which is associated with a deepening of the magnetic well with β and the steepening of the radial gradient of the poloidal current flux. The fraction of drift-reversed particles on flux surfaces with $s = 3/18$, $s = 10/18$ and $s = 16/18$ occupy the solid regions in Figs. 2a-2c for $\beta = 0.15\%$, in Figs. 2d-2f for $\beta = 1.5\%$ and in Figs. 2g-2i for $\beta = 5.3\%$.

4. Summary and conclusions

In summary, we have analysed the conditions for drift reversal in the Wendelstein VII-X Advanced Stellarator. For this purpose, we have evaluated the bounced-averaged drifts in ballooning space because local stability of a plasma is commonly investigated after invoking the ballooning mode transformation (in order to reconcile conditions of periodicity in systems with shear). The calculations are performed in the straight field line Boozer magnetic coordinates . At low β, we obtain that the helically (toroidally) trapped particles have bounced-averaged drift frequencies of the same (opposite) sign compared with the diamagnetic drift frequency (assuming monotonically descreasing density profiles). As β increases, we find that the fraction of trapped particles that experience drift reversal also increases (manifested by a change in the sign of the ratio of the drifts). This increase is attributed mainly to the modification of the grad-B drift due to the combination of a favourable variation of the radial gradient of the Jacobian (which is related to a deepening of the magnetic well with β) and a steepening of the poloidal current flux gradient. Near the MHD β limit of 5%, nearly all the trapped particles become drift-reversed. This could have very favourable implications for anomalous transport in the WVII-X.

References

[1] Rosenbluth M N et al, *Phys. Rev. Lett.* 51 1967 (1983)
[2] Beidler C. et al., *Fusion Technol.* 17 148 (1990)
[3] Nührenberg J and Zheng L J, *Proc. 20th EPS Conf. Contr. Fusion Plasma Phys.* ECA17c I-413 (1993)
[4] Rosenbluth M N and Sloan M L, *Phys. Fluids* 14 1725 (1971)
[5] Connor J W, Hastie R J and Taylor J B, *Phys. Rev. Lett.* 40 396 (1978)
[6] Boozer A H, *Phys. Fluids* 23 904 (1980)
[7] Hirshman S P and Betancourt O, *J. Comput. Phys.* 96 99 (1991)
[8] Anderson D V et al, *Int. J. Supercomp. Appl.* 4 34 (1990)
[9] Roach C M, Connor J W and Janjua S J, *Culham Laboratory Report* 281 (1995)

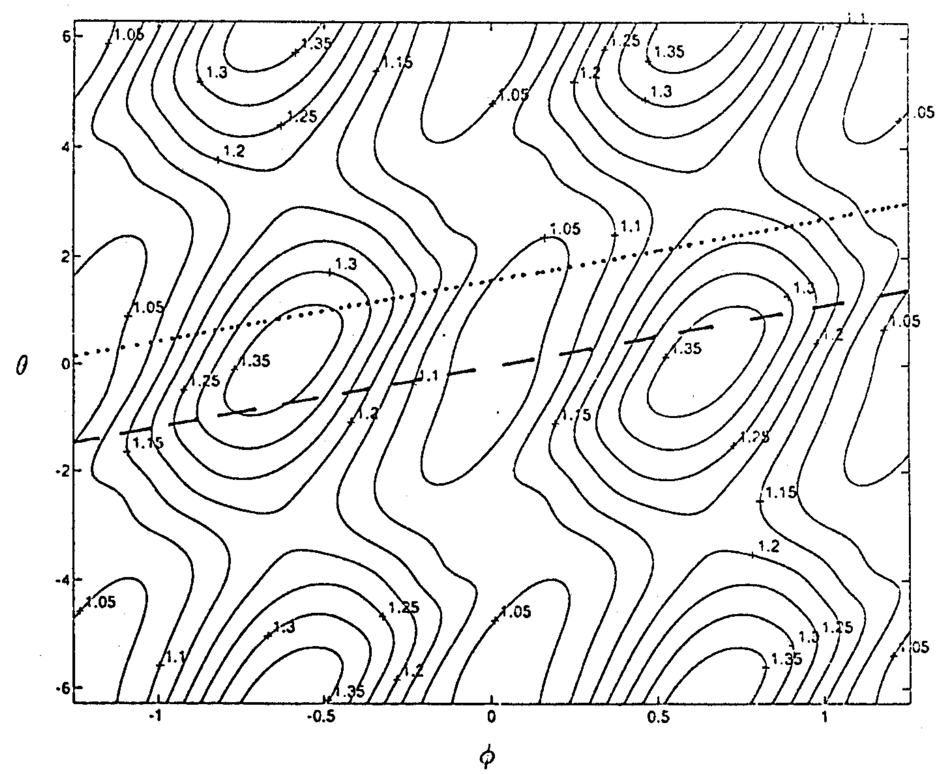

Figure 1: The mod-B contour distribution in WVII-X on a flux surface with $s = 10/18$ at $\beta = 1.5\%$ peeled open over the poloidal and toroidal Boozer magnetic coordinate angles θ and ϕ, respectively. This distribution covers two field periods $-2\pi/5 < \phi < 2\pi/5$ and two poloidal transits $2\pi < \theta < 2\pi$. The dashed line corresponds to the trajectory of the magnetic field line labelled $\alpha = 0$ and the dotted line corresponds to the field line with $\alpha = 2\pi/5$ or alternatively can be considered as the $\alpha = 0$ line but one field period downstream.

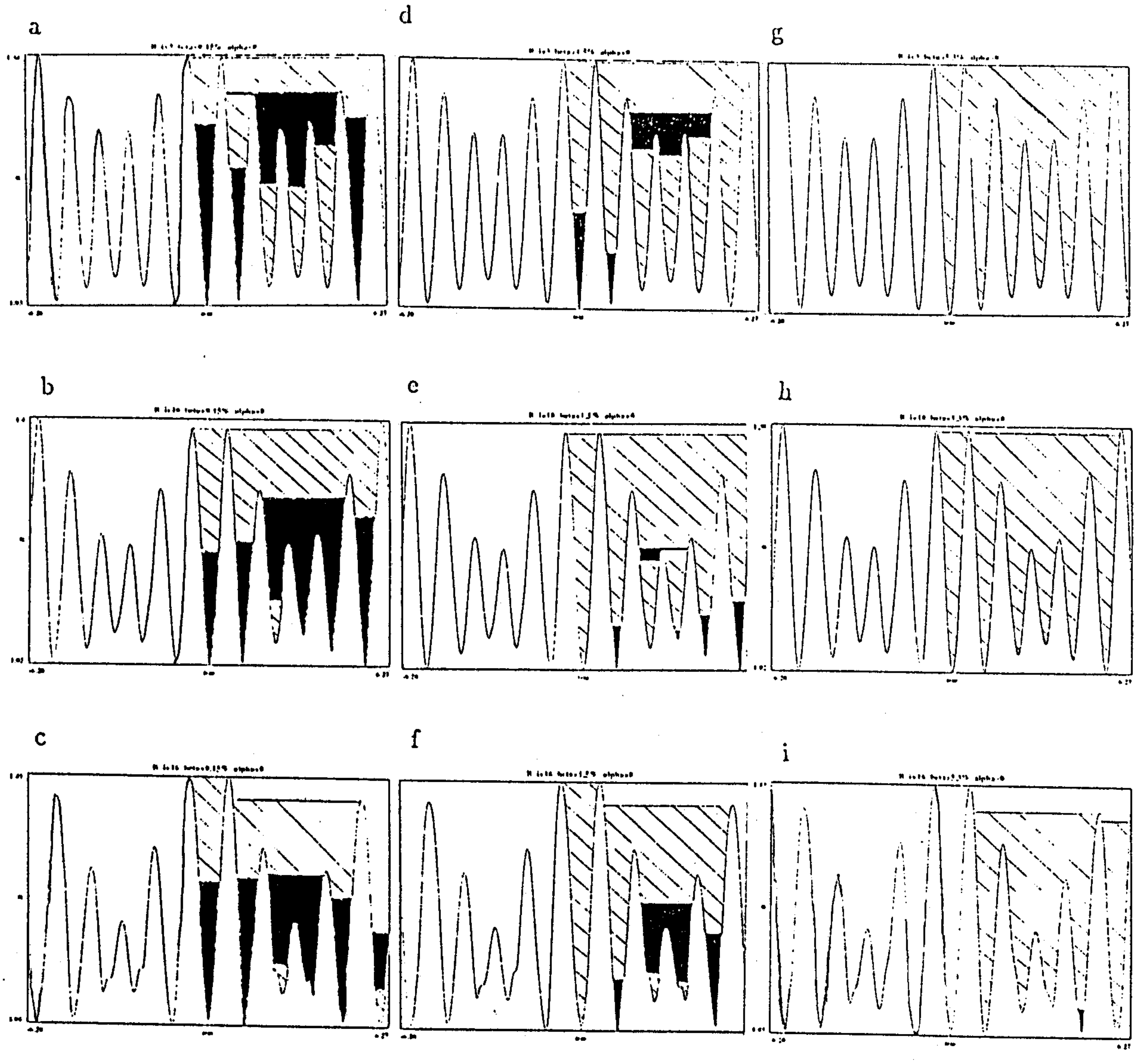

Figure 2: The magnitude of the magnetic field in WVII-X as a function of the poloidal angle θ along the field line $\alpha = 0$ for a) $\beta = 0.15\%$ and $s = 3/18$, b) $\beta = 0.15\%$ and $s = 10/18$, c) $\beta = 0.15\%$ and $s = 16/18$, d) $\beta = 1.5\%$ and $s = 3/18$, e) $\beta = 1.5\%$ and $s = 10/18$, f) $\beta = 1.5\%$ and $s = 16/18$, g) $\beta = 5.3\%$ and $s = 3/18$, h) $\beta = 5.3\%$ and $s = 10/18$, and i) $\beta = 5.3\%$ and $s = 16/18$. Trapped particles that experience drift reversal are confined in the solid regions and those do not drift-reverse are located in the hatched regions.

SPECTRA AND MODE STRUCTURE OF GLOBAL DRIFT MODES IN TOROIDAL GEOMETRY

S. Brunner and J. Vaclavik

Centre de Recherches en Physique des Plasmas/ Ecole Polytechnique Fédérale de
Lausanne/ Av. des Bains 21, 1007 Lausanne/ SWITZERLAND

Abstract. To get an overview of drift waves in tokamak plasmas, a fluid code was written so as to easily obtain spectra and mode structure over a wide range of parameters. In particular, the goal of this study was to understand the effect of toroidicity and ellipticity on these waves and whether they can induce new modes. In this spirit, the simplest fluid

[redacted]

where $\vec{x}_p$ is the position in the poloidal plane, φ the toroidal angle and ω the antenna frequency. Using in addition the continuity equation for ions, one obtains:

$$e\left[N\frac{e\phi}{T_e}-\frac{1}{i\omega}\,\vec{\nabla}\cdot(N\,\vec{v})\right]=\rho^{ant}, \tag{2}$$

where $\vec{v}=-\frac{1}{B}\,\vec{\nabla}_\perp\,\phi\times\,\vec{e}_\parallel+\frac{i}{B}\frac{(\omega+i\nu)}{\Omega}\,\vec{\nabla}_\perp\,\phi-i\frac{e}{m_i}\frac{1}{(\omega+i\nu)}\nabla_\parallel\phi\,\vec{e}_\parallel$, having assumed $\omega\ll\Omega=eB/m_i$. The first term in the relation for $\vec{v}$ leads to $\vec{F}\times\vec{B}$ drifts, where $\vec{F}$ is related to curvature of magnetic field and to density inhomogeneities. The second term is the polarization drift which is the only coupling in our model between magnetic surfaces in the case of a cylindrical geometry. The above equation can be cast into a weak variational form :

$$\begin{aligned}\int_{V_p}\frac{N}{N_0}\Bigg\{&(\omega+i\nu)^2\left[\frac{T_{e0}}{T_e}\tilde{\phi}^\star\phi+\left(\frac{c_{s0}}{\Omega}\right)^2\vec{\nabla}_\perp\,\tilde{\phi}^\star\,\vec{\nabla}_\perp\,\phi\right]\\&+i(\omega+i\nu)\frac{{c_{s0}}^2}{\Omega}\left(\vec{\nabla}_\perp\,\tilde{\phi}^\star\times\vec{\nabla}_\perp\,\phi\right)\cdot\vec{e}_\parallel-c_{s0}^2\nabla_\parallel\tilde{\phi}^\star\nabla_\parallel\phi\Bigg\}\,d^3x=\\&(\omega+i\nu)^2\frac{T_{e0}}{e}\int_{V_p}\tilde{\phi}^\star\frac{\rho^{ant}}{eN_0}d^3x,\end{aligned} \tag{3}$$

using the notation $c_{s0}=\sqrt{T_{e0}/m_i}$ for the sound velocity and $\tilde{\phi}$ for a test function. Notice that in the absence of friction ($\nu=0$), this form is Hermitian.

For simplicity, we use the magnetic geometry given by a Solovev equilibrium. Poloidal flux is thus defined by

$$\psi(r,z)=\frac{\psi_s}{a^2R^2}\left[\frac{r^2z^2}{E^2}+\frac{1}{4}\left(r^2-R^2\right)^2\right], \tag{4}$$

R being the major radius, a the minor radius, E the elongation, $\psi_s=\frac{E}{2q_0}a^2B_0$ the flux at plasma surface, B_0 the magnetic field on magnetic axis and q_0 the safty factor on magnetic axis. Density and electron temperature profiles are of the form : $N(s)=N_0\left(1-\beta s^2\right)^\alpha$, $T_e(s)=T_{e0}\left(1-\delta s^2\right)^\gamma$, where $s=\sqrt{\psi/\psi_s}$ is the radial magnetic variable.

Equation (3) can be compared with the dispersion relation in slab geometry

$$\omega^2-\omega\omega^\star-(c_sk_\parallel)^2=0, \tag{5}$$

where $\omega^\star=\vec{k}\cdot\vec{v}_d$, $\vec{v}_d$ representing drifts. In this last relation we have omitted polarization drift. The effect of polarization drift can be easily illustrated in the special case of sound waves in a homogeneous plasma where it leads to dispersion in the direction perpendicular to the magnetic field :

$$\omega^2=\frac{(k_\parallel c_s)^2}{1+\left(\frac{c_s}{\Omega}\right)^2k_\perp^2}. \tag{6}$$

2 Numerical Method

Euation (3) was solved in the poloidal plane by performing a Fourier series decomposition with respect to the poloidal angle θ and by using linear finite elements in the radial direction. In this way, the potential ϕ was projected on the basis functions : $\phi_{i,m} = \frac{1}{2\pi} f_i(s) \exp i(m\theta + n\varphi)$, $f_i(s)$ being the radial linear element centered at mesh point s_i. The same definition was used for the test functions $\tilde{\phi}$. The program was run on a SUN SPARC station.

3 Results

For the results presented here, we chose the following values: $R = 1.m$, $a = 0.2m$, $q_0 = 1.98$, $B_0 = 2.Tesla$, $\frac{N(s)}{N_0} = (1 - s^2)$, $T_e(s) = T_{e0}(1 - s^2)^2$, $T_{e0} = 1.keV$, $n = 5$, ions are protons. To unbend a torus into a cylinder in such a way that eigenfrequencies and mode structures can be compared, one must apply the following transformations: $(R, q_0, n) \Longrightarrow (pR, q_0/p, pn)$, the other physical parameters remain constant. Our starting point is a cylinder ($p = 500$) with circular cross section (E=1). In this geometry modes contain a single poloidal mode number m and one can speak of a parallel wave number given by $k_{\|} = \frac{1}{Rq_0}(nq_0 - m)$. As we are interested in drift waves i.e. $\omega \simeq \omega^*$, one can see from relation (5) that $k_{\|} \simeq 0$ so that $m \simeq nq_0$. For this reason we concentrated our study around $m = 10$ as $nq_0 \simeq 9.9$. Furthermore we chose the antenna such that it couples best to modes with low radial number i.e. $l \simeq 1 - 5$ and therefore fixed :

$$\rho^{ant}(s, \theta, t) \sim [s(1 - s)]^{|m|} \sin(\pi s) \exp i(m\theta + n\varphi - \omega t). \qquad (7)$$

The number of radial mesh points was typically taken between $ns = 40 - 80$.

When the cylinder is bent into a torus ($p \rightarrow 1$) toroidicity leads to coupling between modes with different poloidal mode numbers. The dominant coupling is between m and $m \pm 1$. For $p = 1$ ($R/a = 5$) the number of significant poloidal Fourier coefficients is around 20. In the same way, ellipticity leads to dominant coupling between m and $m \pm 2$.

Exciting the plasma with an antenna of type $m = 10$, one can easily follow the eigenfrequencies of former cylindrical modes $m = 10$ as parameters are varied by following the coresponding peaks on the response curve (see Fig.1). With toroidicity and ellipticity, peaks relative to former cylindrical modes with neighbouring m's ($m = \ldots, 8, 9, 11, 12, \ldots$) appear on the response curve. **However no new modes are induced.** Besides, rational surfaces do not affect the mode structure in any particular way.

4 Conclusion

Although our model is restricted as it contains none of the kinetic effects that can lead to instabilities, it allowed to clarify the properties of global drift waves in toroidal geometry. New modes induced by toroidicity or ellipticity were not observed. The results will serve as a reference for futur kinetic studies.

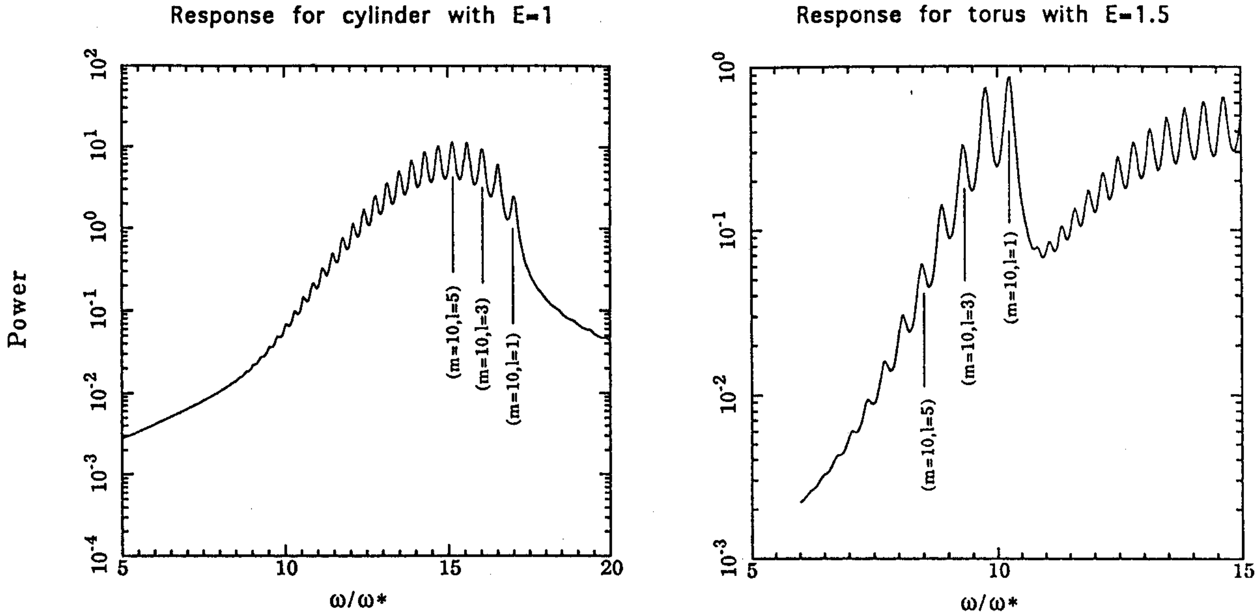

Fig.1 *When bending a cylinder with circular cross-section into a torus with elongated cross-section, one can identify the eigenfrequencies of former cylindrical modes by following the core-sponding peaks on the response curve.*

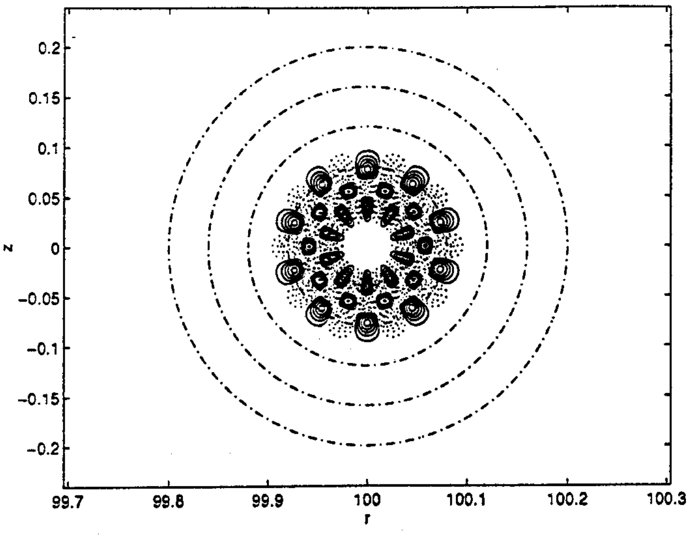

Fig.2 *Mode (m=10,l=3) in non elongated cylinder.*

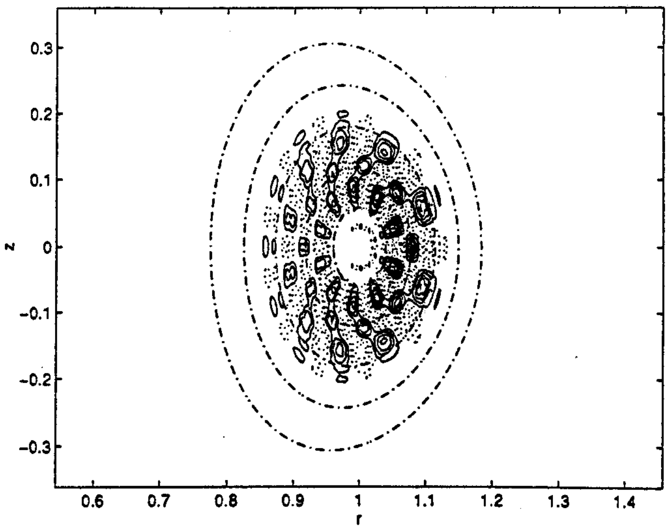

Fig.3 *Former mode (m=10,l=3) in elongated torus.*

Linear electrostatic gyrokinetic PIC code for trapped ion modes in toroidal geometry

M. Fivaz, K. Appert, J. Vaclavik

Centre de Recherches en Physique des Plasmas, Association Euratom-Confédération Suisse,
Ecole Polytechnique Fédérale de Lausanne, Av. des Bains 21, 1007 Lausanne, Switzerland

1. Introduction

Drift-type microinstabilities such as η-i and trapped ion modes are good candidates for explaining anomalous transport in tokamaks [1,2]. This project aims at modelling accurately the linear physics of these modes in realistic toroidal geometry.

The modelling of these instabilities requires a gyro-averaged kinetic description of the plasma [3,4]. The pertinent five-dimensional phase space problem can be solved with Particle-In-Cell (PIC) methods. These algorithms can be implemented efficiently on massively parallel machines, taking advantage of their large memory and computing power. The code presented here runs on the CRAY T3D parallel supercomputer.

The model includes full banana orbits and arbitrary density and temperatures profiles. It is run at realistic aspect ratio, with a magnetic structure obtained from a Solovev equilibrium.

2. The Physical Model

- Linear Boltzmann electrons with quasi-neutrality condition: $n_e = n_0\left(1 + \frac{e\phi}{k_B T_e}\right) = n_i$
- Electrostatic approximation: magnetic field **B** is static, the electric field $\mathbf{E} = -\,\mathbf{grad}\ \phi$
- Gyrokinetic ions [4] of gyrocenter distribution $f^t(\mathbf{R}, v_{/\!/}, v_\perp, t)$. The Larmor radius is assumed much smaller than the perpendicular wavelength
- This model is then linearized by taking $f^t = f_0 + f$, where f_0 is an axisymmetric equilibrium distribution, usually a local Maxwellian, and f is a small perturbation. Perturbed quantities $(f, \phi, \mathbf{E})$ can be Fourier expanded in the toroidal angle φ, for instance:

$$\phi(R,\varphi,Z) = \mathrm{Re}\ \{\phi(R,Z)\exp(-in\varphi)\}$$

One then obtains for the complex Fourier amplitudes of the perturbation:

$$\left(\frac{d}{dt} - in\frac{d\varphi}{dt}\right) f = -\,\frac{\mathbf{E} \times \mathbf{B}}{B^2}\,\frac{\partial f_0}{\partial \mathbf{R}} - \frac{e}{m}\mathbf{E}_{/\!/}\,\frac{\partial f_0}{\partial v_{/\!/}}$$

$$\frac{df}{dt} = \frac{\partial f}{\partial t} + \mathbf{v}_{gc}\,\frac{\partial f}{\partial \mathbf{R}} + \frac{dv_{/\!/}}{dt}\,\frac{\partial f}{\partial v_{/\!/}} + \frac{dv_\perp}{dt}\,\frac{\partial f}{\partial v_\perp}$$

$$\mathbf{v}_{gc} = v_{/\!/}\,\mathbf{h} + \frac{m(v_\perp^2 + 2\,v_{/\!/}^2)}{2qB}\,\mathbf{h} \times \frac{\mathbf{grad}\ B}{B}$$

$$\frac{dv_{/\!/}}{dt} = \frac{1}{2} v_\perp^2\ \mathbf{div\ h} \qquad\qquad \frac{dv_\perp}{dt} = -\ \frac{1}{2} v_\perp\, v_{/\!/}\ \mathbf{div\ h}$$

$$\frac{n_0 e}{k_B T_e}\,\phi + \nabla_\perp \frac{n_0 e}{m\,\Omega^2} \nabla_\perp \phi = 2\pi \int f\, v_\perp dv_{/\!/} dv_\perp$$

$$\mathbf{E} = -\ \mathbf{grad}\ \phi + \frac{in\phi}{R}\,\mathbf{e}_\varphi \qquad\qquad \mathbf{h} = \frac{\mathbf{B}}{B}$$

where the symbols have their usual meaning; the parallel subscript denotes the direction of the magnetic field.

3. The Discrete Model

Phase space discretization: one chooses a partition of phase space in N_p domains of phase space volume ξ_v and position centred on (R_v, Z_v, $v_{/\!/v}$, $v_{\perp v}$), v=1..N_p. Defining:

$$f(\mathbf{R},v_\perp,v_{/\!/}) = \sum_v \frac{f_v}{4\pi^2 v_\perp R}\,\delta(R-R_v)\,\delta(Z-Z_v)\,\delta(v_\perp - v_{\perp v})\,\delta(v_{/\!/} - v_{/\!/v})$$

where f_v is the number of ions in ξ_v. One obtains:

$$\frac{df_v}{dt} = -\left(\frac{\mathbf{E}\mathbf{x}\mathbf{B}}{B^2}\frac{\partial f_0}{\partial \mathbf{R}} + \frac{q}{m}E_{/\!/}\frac{\partial f_0}{\partial v_{/\!/}}\right)\xi_v + in\frac{d\varphi_v}{dt} f_v$$

$$\frac{n_0 e}{k_B T_e}\,\phi + \nabla_\perp \frac{n_0 e}{m\,\Omega^2} \nabla_\perp \phi = \sum_v \frac{f_v}{2\pi R}\,\delta(R-R_v)\,\delta(Z-Z_v)$$

Potential discretization: the potential is expanded on a finite element basis on a **(s,θ) mesh**, i.e. (flux surface coordinate $s=\sqrt{\Psi}$, poloidal angle). **Quadratic spline** elements over both direction are used. The discrete equation obtained for the potential leads to a symmetric banded matrix problem. The perpendicular plane is approximated as the poloidal plane.

Time discretization: **4th order Runge-Kutta** scheme. Within this scheme, for additional precision, the guiding centre trajectories in phase space are advanced in time using a Burlish-Stoer scheme and are corrected after every time step so as to conserve exactly the three constants of motion of guiding centres (kinetic energy, magnetic moment and toroidal canonical momentum).

4. Convergence properties

- For all the runs described herein, the magnetic structure is taken from a Solovev MHD equilibrium, with major radius R=0.88 m, minor radius a=0.24 m (R/a=3.7), safety factor on axis $q_0 = 2.88$, magnetic field on axis $B_0 = 1.4$ Tesla and elongation between 1 and 1.6. The equilibrium distribution function f_0 is a local Maxwellian. Density and electron temperature profiles are of the form $(1-s^4)$ with values of 10^{20} m^{-3} and 2 Kev on axis whereas ion temperature goes as $(1-s^2)^2$ with 2 Kev on axis, and one tenth of these values at the plasma boundary.
- Arbitrary initial conditions are evolved until the most unstable mode emerges. The growth rate is then obtained by measurement of the time dependence of the potential.
- The convergence of the growth rate with respect to grid size, time step and number of particles was demonstrated, as shown on figure 1 with respect to the number of particles.

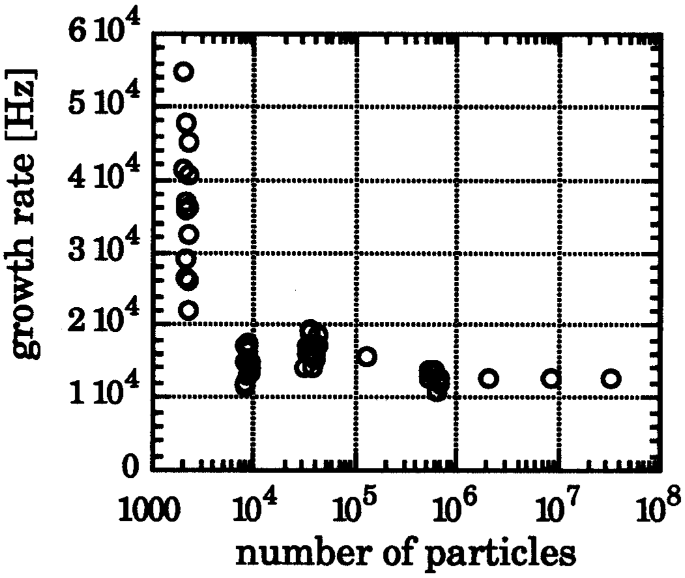

*Fig 1: Convergence of the growth rate of the most unstable eigenmode with respect to the number of particles for a 60*16 spatial mesh*

- A numerical instability occurs if a particle crosses several poloidal cells in one time step, imposing a constraint on the time step. Filtering in poloidal Fourier space reduces this constraint in addition to reducing the particle noise.

5. Results

- Figure 3 shows the dependence on elongation of the frequency and growth rate of the most unstable mode. We call mode A the most unstable eigenmode obtained for a plasma with elongation 1. Its frequency is of the order, but smaller than the typical bounce frequency. The mode radial wavelength is of the order of the banana width. This mode is strongly stabilized by elongation. For elongation higher than 1.15, the growth rate of mode A is lower than the growth rate of another low frequency mode B.

Non Perturbative Kinetic Effects on Alfvén Eigenmodes in Tokamak Plasmas

A Jaun, **K Appert**, J Vaclavik and L Villard
Centre de Recherches en Physique des Plasmas, Association Euratom - Confédération Suisse
Ecole Polytechnique Fédérale de Lausanne
Av. des Bains 21, 1007 Lausanne, Switzerland

1. Introduction

Global modes of the Alfvén wave exist in tokamaks because of the equilibrium current (GAE), the toroidicity (TAE), the pressure (BAE) and the shaping of the plasma (EAE). These modes have already been studied numerically [1,2,3] using either cylindrical kinetic or toroidal fluid plasma models; comparisons with experiments showed however important limitations and led to the recent development of the toroidal PENN code [4], which includes a resistive fluid and a kinetic model based on a finite Larmor radius (FLR) expansion. Using this new tool, kinetic effects are here studied for a GAE mode in a medium size tokamak.

2. Model

To model the propagation of Alfvén waves in a tokamak, a general MHD equilibrium is first computed using the CHEASE code [5] and the geometry extended further into a vacuum region limited by a perfectly conducting wall. The linear field perturbations expressed in terms of the electromagnetic potentials (**A**,Φ) are then obtained for a given model of the dielectric tensor.

The fluid plasma model [6] has been derived in the frame of resistive MHD, assuming that the resonant wave-particle interactions and the Larmor excursion of the particles remain negligible. The more sophisticated kinetic approach [7] is based on a finite Larmor radius (FLR) expansion and takes both of these effects into account: it provides a consistent description of the Landau damping and allows for conversion to either the kinetic Alfvén wave (KAW) or the surface quasi-electrostatic wave (SQEW), depending on whether the ratio between the parallel phase velocity of the wave and the thermal speed of the electrons $\omega/(k_{//}v_{th,e})$ is smaller or bigger than unity.

The oscillating helical antenna current driven inside the vacuum region serves to calculate the response of the cavity and to check the consistency of the numerical solution using the balance between the power absorbed by the plasma, the energy flux and the antenna load.

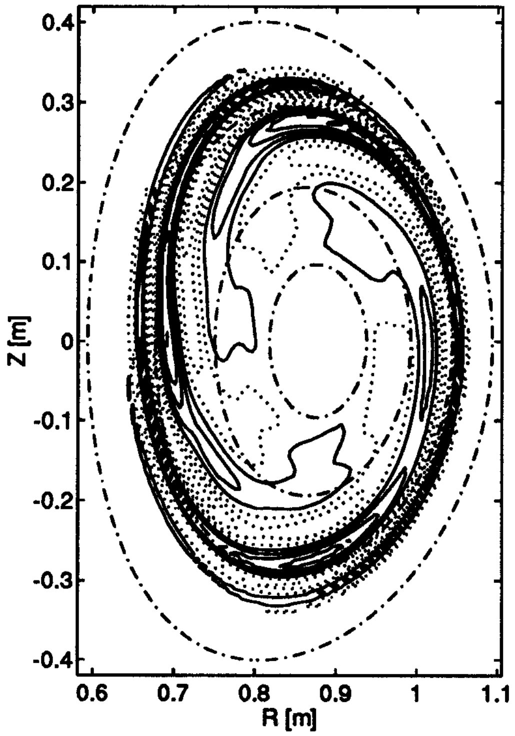

Figure 2: most unstable eigenmode, for elongation 1.6, n=1

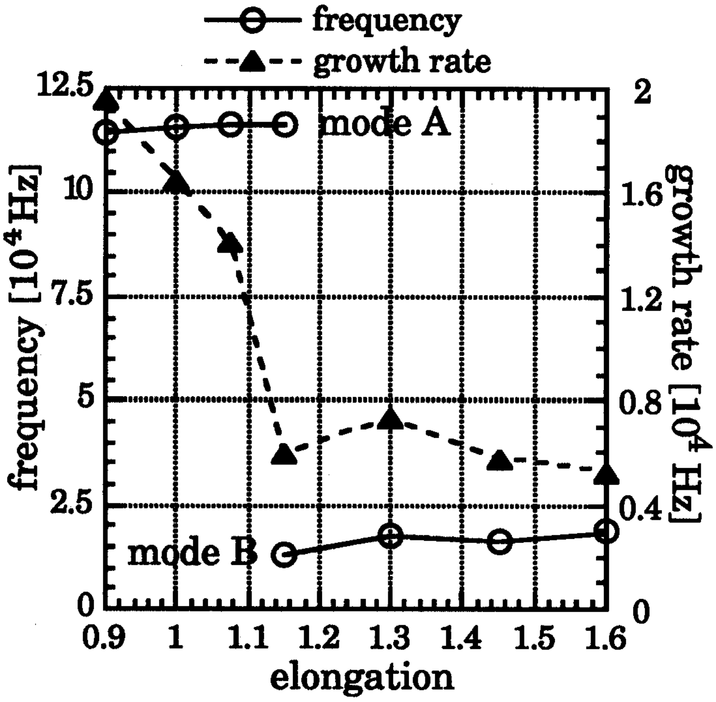

Figure 3: Frequency and growth rate of the most unstable mode as a function of elongation

6. Conclusions

A linear gyrokinetic PIC solver has been developed for toroidal geometry. It takes fully into account the ion banana width, trapped ion resonances and arbitrary equilibrium profiles. The model was shown to converge with the numerical parameters. The banana width can determine the radial wavelength. Elongation can have a strong effect on the most unstable mode.

Acknowledgements

This work was partly supported by Cray Research, Inc. within the framework of the Cray Research/EPFL Parallel Application Technology Program and by the Swiss National Science Foundation. The computations were done on the CRAY-T3D massively parallel computer at EPFL, Lausanne. The authors thank S. Brunner, V. Decyk, W.W. Lee, S. Parker, O. Sauter, R. Sydora and T.M. Tran for useful discussions.

References

[1] W.M. Tang, Nuclear Fusion 18, 1098 (1978)
[2] S.E. Parker, Phys. Rev. Letters 71, 2042 (1993)
[3] W.W. Lee, Phys. Fluids 26 (1993)
[4] T.S. Hahm, Phys. Fluids (1988)

3. GAE mode in the TCA tokamak

A force-free equilibrium of circular cross-section is defined with the parameters R_0=0.61 m, R_0/a=3.39, R_W/a=1.167, B_0=1.5 T, q_0=1.05, q_a=4.55, $n_e=n_D=5.2\times10^{19}(1-0.98s^2)^{0.7}$ m^{-3}, $T_e=2T_D=T_0(1-0.84s^2)$ eV reminding the TCA experiment [9], except for the rather flat temperature profile which has been chosen to avoid conversion to an SQEW at the plasma edge. A helical antenna current (n=-2, m=-1) is driven in the vacuum region half way between the plasma edge and the perfectly conducting wall.

Using first the fluid model to calculate the plasma response, a generator frequency scan illustrated in fig.1 reveals the presence of a GAE mode at 2.38 MHz and the edge of the continuum at 2.41 MHz. Apart from the global m=-1 structure in the center which is characteristic for this mode, the fluid wavefield in fig.2 shows that several Alfvén resonances are simultaneously present at radial positions s=0.79, 0.88, 0.93, 0.96, 0.97, 0.985 and yield a continuum damping of $|\gamma/\omega| \cong 0.75\%$ via resonant absorption.

The same study is then repeated with the kinetic model for an electron temperature increasing from T_0=400, 600, 800 eV to 1 keV. Fig.1 shows that the GAE mode is first clearly found at 2.32 MHz, but is then up-shifted to 2.33 and 2.37 MHz before it disappears completely for the highest temperature. Although it is difficult to measure the damping rate precisely, approximate values obtained for the three lowest temperatures give $|\gamma/\omega| \cong$ 1, 1.5 and 2.6% which are an order of magnitude higher than those predicted by cylindrical FLR models [9]. Combined with a Fourier analysis of the kinetic wavefields, fig.2 suggests how toroidal FLR effects damp the GAE mode via two different mode conversion processes.

At T_0=400 eV, the global GAE wavefield is clearly dominant inside and its radial extension agrees remarkably well with the fluid result. Unlike for the fluid model, short wavelength oscillations appear between s=0.55 and the center, with poloidal Fourier amplitudes m=-1 increasing, and m=0, +1 decreasing towards the center. A comparison with the local dispersion relation indicates that these oscillations correspond to a KAW. The innermost Alfvén resonance is at s=0.79, but no conversion takes place there. Therefore, we interpret the existence of the kinetic wavefield between s=0.55 and the center as a result of the toroidal coupling between the global wavefield and the KAW. This *non-perturbative* interaction (in the sense that it cannot be obtained perturbatively from a toroidal fluid model because the finite-Larmor radius effects are a *singular perturbation*) is strongest at s=0.55 where $R_0/a \cong 6$ is still not very large. The KAW is subsequently damped by electron Landau damping as it propagates towards the center. This whole process has been called *radiative damping* in ref.[10].

Increasing the temperature to T_0=600 eV, brings the ratio $\omega/(k_{//}v_{th,e}) \cong 0.5$ at s=0.9 down to 0.37, so that the conversion begins to be possible at the outer resonances: the KAW does however still not propagate very far and the global mode damping is probably still dominated by the Landau damping of the KAW in the plasma core.

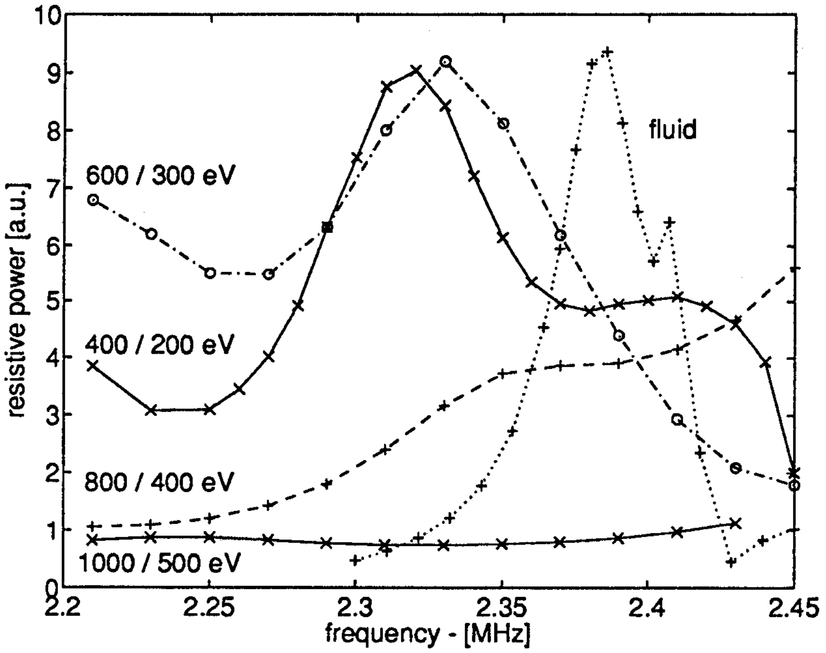

Fig.1: Power absorption as a function of frequency using the fluid and the kinetic model with different temperatures

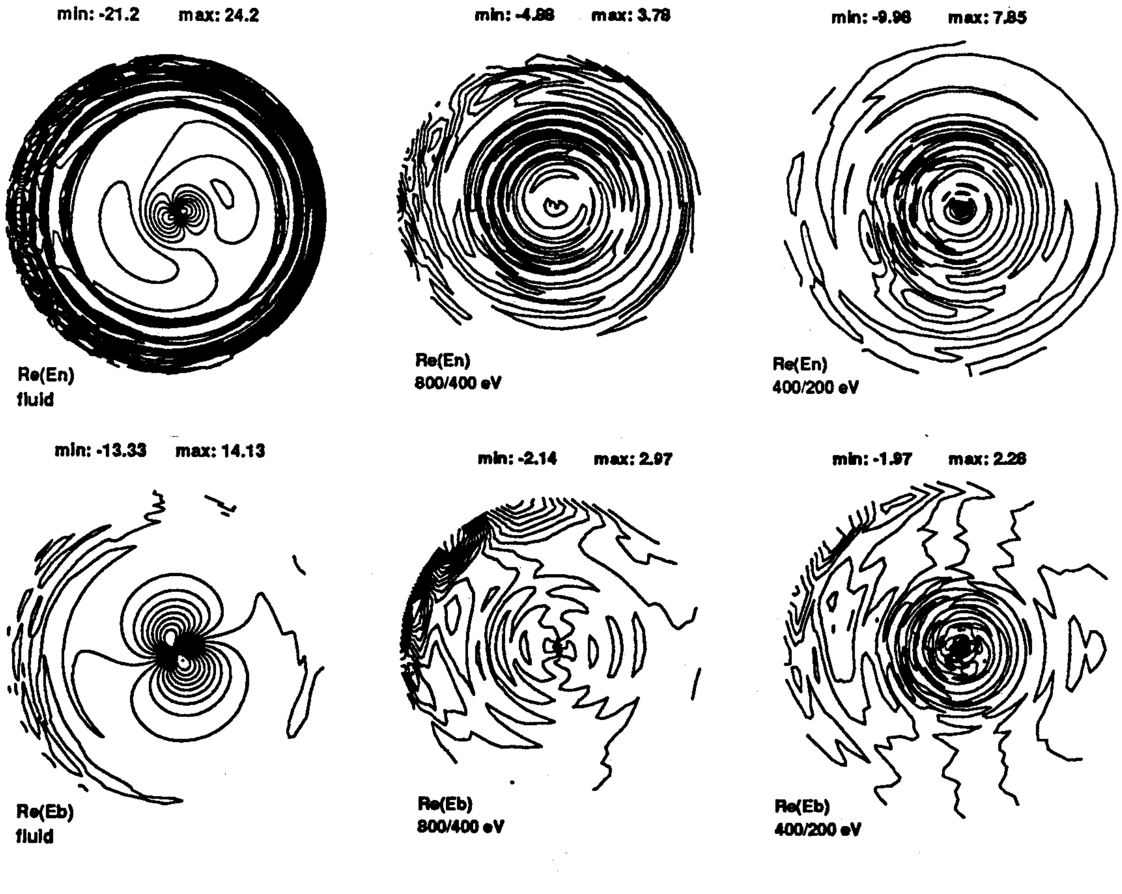

Fig.2: Radial E_n and poloidal E_b electric field for three GAE modes of fig.1

At T_0=800 eV and 1 keV, this ratio is further reduced to 0.32 and 0.29, so that the mode conversion taking place at the resonances becomes strong enough that it drowns the GAE mode character in the center, damping out the peak in the plasma response (fig.1).

Despite the qualitative difference between the fluid and the kinetic results, both predict GAE damping rates which are in good agreement with the experimentally observed $|\gamma/\omega| \cong$ 1-2%. The single fact that this value remained constant during all the years of exploitation of TCA speaks however strongly in favor of the non-perturbative damping process in the plasma core, where the parameters remained much more similar from shot to shot than in the edge region.

4. Conclusion

An analysis has been carried out for the GAE mode observed in the TCA tokamak. Both, the fluid and the kinetic models implemented in the toroidal PENN code predict frequencies and dampings which are in good agreement with the experiment. Using the fluid model, the GAE mode is located in the plasma core and damped via resonance absorption in the plasma exterior. With the kinetic description, two conversion mechanisms lead to the Landau damping of a KAW: one is the counterpart of the fluid models' resonance absorption and occurs in the external parts of the plasma; the other has no such fluid correspondance, and is induced non perturbatively in the plasma core through toroidal coupling between the global GAE wavefield and the KAW.

Acknowledgments

This work was supported in part by the Swiss National Science Foundation.

References

[1] Appert K, Gruber R, Troyon F, Vaclavik J, *Plasma Physics* **24** (1982) 1147

[2] Cheng C Z, Chance M S, *Phys.Fluids* **29** (1986) 3695

[3] Heidbrink W W, Strait E J, Chu M S, Turnbull A, *Phys.Rev.Lett.* **71** (1993) 885

[4] Jaun A, Appert K, Vaclavik J, Villard L, *submitted to Comput.Phys.Commun.*

[5] Lütjens H, Bondeson A, Roy A, *Comput.Phys.Commun.* **69** (1992) 287

[6] Vaclavik J, Appert K, *Nucl.Fusion* **31** (1991) 1945

[7] Brunner S, Vaclavik J, *Phys.Fluids B* **5** (1993) 1695

[8] Collins G, Hofmann F, Joye B, *Phys. Fluids* **29** (1986) 2260 and references cited therein.

[9] Appert K *et all., Plasma Physics (Proc. 7th Int. Conf. Kiev, 1987),* Invited papers Vol.2, World Scientific, Singapore (1987) 1230

[10] Mett R R, Mahajan S M, *Phys.Fluids B* **4** (1992) 2885